TOWARDS THE IMPROVEMENT OF COMMON RANS MODELS IN THE PREDICTION OF BUOYANCY INFLUENCED HEATED GAS FLOWS

A Dissertation

by

AUSTEN DAVID FRADENECK

Submitted to the Office of Graduate and Professional Studies of
Texas A&M University
in partial fulfillment of the requirements for the degree of

DOCTOR OF PHILOSOPHY

Chair of Committee,	Mark L. Kimber
Committee Members,	Karen Vierow Kirkland
	Debjyoti Banerjee
	Jorge Alvarado
Head of Department,	Andreas A. Polycarpou

August 2020

Major Subject: Mechanical Engineering

ABSTRACT

An emerging trend in the nuclear community is to utilize RANS based turbulence models to supplement thermal-hydraulic system codes in the design of Generation-IV (Gen-IV) power reactors. Prior to full integration into the design process for Gen-IV reactor concepts, RANS models must undergo thorough validation studies to justify their applicability in both normal and accident conditions. Several previous numerical studies have raised concerns regarding the performance of RANS models within buoyant flow regimes indicative of a loss of flow accident (LOFA). To address these concerns, the current research performs a detailed assessment of 5 different RANS based turbulence models against benchmark experimental data designed to replicate the transient conditions of a LOFA along a heated vertical plate. Boundary conditions and system response quantities for the numerical model are supplied from the experiment every 0.2 seconds during the 18.2 second transient. ASME standards are used to quantify the numerical uncertainties while the input uncertainties are handled using a Latin Hypercube Sampling (LHS) method based on the steady-state conditions ($t = 0\ s$). Qualitative comparisons between numerical and experimental results at several downstream locations are supported using a validation metric based on the statistical disparity between the respective empirical and cumulative distribution functions. Overall, the RANS based turbulence models are unable to accurately predict the system response quantities supplied through the experiment, most notably during the flow reversal where the buoyancy force is dominant. In comparison to the other RANS

models, the Abe-Kondoh-Nagano (AKN) $k-\epsilon$ variant is the most consistent with the experimental results and is selected for additional assessment and development.

To further assess the AKN models applicability in buoyant flows, a comprehensive analysis is conducted against well trusted Direct Numerical Simulation (DNS) databases for mixed convection flows characterized over a range of Richardson numbers (Gr/Re^2). The analysis suggests that at intermediate Richardson numbers, the AKN model is insensitive to changes in buoyancy, resulting in grossly overpredicted values of Nusselt number and skin-friction coefficient. To correct this, a new source term is derived to increase the turbulent dissipation rate as a function of local buoyancy related flow variables to improve the prediction of the turbulent viscosity. Using the previously mentioned validation metric, the modified AKN model is shown to greatly improve predictions at the intermediate Richardson numbers while maintaining the integrity of the original model.

ACKNOWLEDGEMENTS

I would like to thank my committee chair and academic advisor, Dr. Mark Kimber, for the abundance of guidance and support over the past few years. I would also like to thank my committee members, Dr. Kirkland, Dr. Banerjee and Dr. Alvarado for their patience and support throughout this entire research process.

I would especially like to thank my friends and colleagues here at Texas A&M University, specifically, Dr. Corey Clifford, Paul J. Kristo, Adam M. Oler, Nolan E. MacDonald, Ramiro Freile and Mohammad Tareq Bani Ahmad. Without the endless support and countless conversations, none of this research would be possible. I would also like to thank my past colleagues from the University of Pittsburgh, Dr. Matthew M. Barry, Dr. Douglas T. Landfried, Dr. Greg Stehle, Dr. Michael Durka and Dr. Konstantin Redkin for offering me endless help and guidance early in my graduate career.

Most importantly, I would like to thank my loving family for always being there for me when I needed them most. Throughout my seemingly endless years of undergraduate and graduate school you have always offered your never-ending care and support for which I am forever grateful.

CONTRIBUTORS AND FUNDING SOURCES

Contributors

This research was supervised by a dissertation committee consisting of Professor Mark Kimber and Karen Vierow-Kirkland of the Nuclear Engineering Department, and Professor Debjyoti Banerjee and Jorge Alvarado of the Mechanical Engineering Department.

All work conducted for the dissertation was completed by the student independently.

Funding Sources

The funding for this work was provided by the United States Department of Energy's Nuclear Energy University Program (NEUP) as part of Project 16-10509. I would like to also recognize the contributions of the Texas A&M University's High-Performance Research Computing (HPRC) who supplied the requisite resources for the computational investigations.

TABLE OF CONTENTS

Page

LIST OF FIGURES

Page

LIST OF TABLES

Page

CHAPTER I

INTRODUCTION

Eddy-viscosity based Reynolds Averaged Navier-Stokes (RANS) models present a practical compromise between accuracy and computational cost, therefore it is no surprise they remain the workhorse for computational fluid dynamics (CFD) codes in both academia and industry. While advances in computational power and efficiency over the past several decades have improved the feasibility of using scale-resolving simulations for routine calculations, typical research and industrial applications do not require such high-fidelity solutions. Instead, information about mean flow quantities predicted with RANS based models is sufficient for most applications. This is not to suggest that the use of such simulations is obsolete; in fact, these models provide details into the small-scale mechanisms that govern the underlying flow physics, which is invaluable when developing or tuning lower resolution models. Utilizing this modeling hierarchy to train lower fidelity models is a highly efficient method to improve accuracy while reducing computational cost.

An emerging trend within the nuclear community is to use RANS models to develop correlations for lower fidelity, thermal-hydraulic system codes for the design of the next fleet of Generation-IV (Gen-IV) power reactors. These codes, such as RELAP-7 [1] and TRACE [2], simplify the reactor core into a myriad of 1-D and 0-D flow networks in which relevant design characteristics can be obtained through empirical correlations. This method greatly reduces the computational time required to model full reactor core designs and components; however, the accuracy of these codes is largely

dependent on the efficacy of the correlations implemented in the calculations. Calculations of nominal operating conditions, which follow classic fully-developed flow configurations, are typically characterized very well using these simplified modeling approaches. However, off normal or accident type scenarios impose complex flow conditions which are not so easily characterized though traditional correlations. This underlying empiricism required in the development of thermal-hydraulic system codes raises concern about the generality of these models to accurately predict resulting flow physics and heat transfer mechanisms in accident type scenarios. The development of reliable correlations for such complex conditions requires a large sample size taken over a wide range of conditions - an arduous and costly process using experiments or scale-resolving simulations. Conversely, this process is considerably more feasible using RANS models. The computational efficiency and simplicity of RANS models also makes it possible to tune these models based on highly trusted canonical flow databases. However, prior to the development of such correlations, RANS models must undergo thorough validation studies to justify their applicability in these accident type scenarios.

Beyond normal operating conditions, it is essential to understand the repercussions of any potentially catastrophic scenarios within Gen-IV reactor designs. From a thermal-hydraulics perspective, a coolant related incident such as a loss-of-flow accident (LOFA) or loss-of-coolant accident (LOCA) is particularly concerning. Gen-IV reactor concepts such as the Very-High Temperature Reactor (VHTR) are susceptible to highly unpredictable flow physics and heat transfer during a LOFA due to its unique flow configuration (see Figure 1).

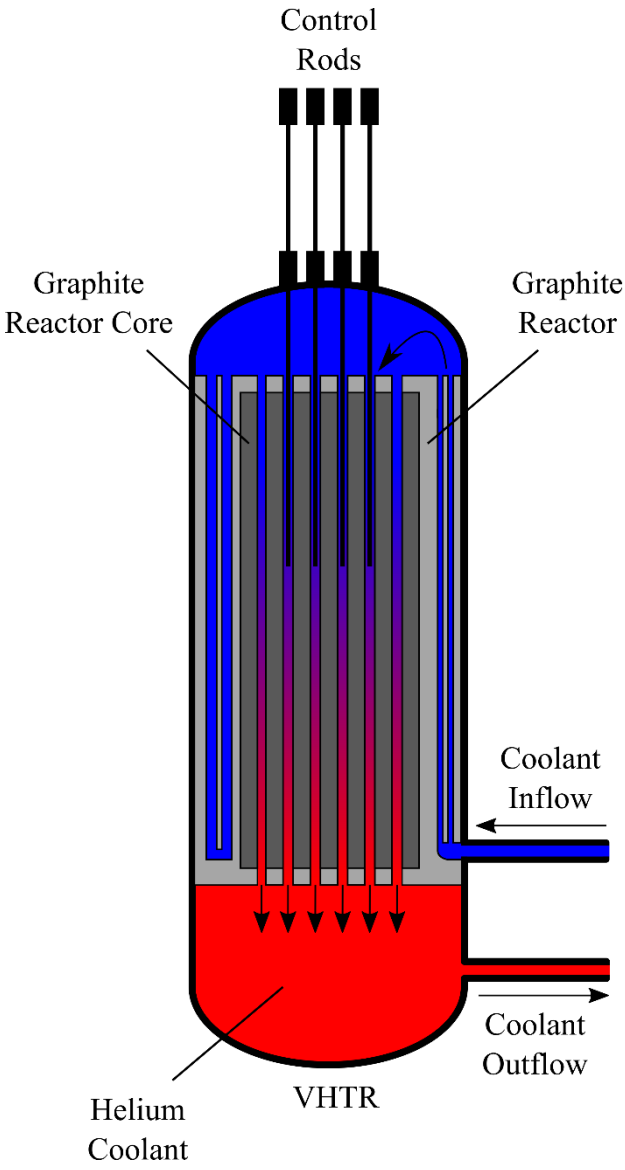

Figure 1: General flow schematic for a Gen-IV VHTR Concept. Revised and modified from original image in [3].

Unlike traditional reactor designs, the coolant in the VHTR is pumped downward through the reactor core into the lower plenum where the heat exits into a secondary loop for electrical generation or process heat applications. In the case of a LOFA, the main driving force for the coolant is compromised such that there is not enough pumping

power to continue normal operation. As this process persists, the inertial driving force begins to diminish and the buoyancy force, driven by density gradients caused by the high heat load in the core, begins to dominate. Inevitably, as the ratio of buoyant to inertial forces continues to grow, the downward flow slows to the point where the flow is completely reversed by the dominant buoyancy force. The change in flow regime from downward forced convection to upward natural convection introduces a significant amount of complexity in providing accurate predictions of the expected heat transfer and flow physics within the core.

Several numerical studies have raised concerns regarding the applicability of RANS models in the case of LOFA conditions within the VHTR [4-7]. In a comparison between several RANS models [4], heat transfer rates in the upper plenum of the reactor varied by several orders of magnitude between different turbulence model formulations. In addition, due to the purely numerical nature of these studies, there is no logical way to discern which of these wildly different solutions most accurately represents the conditions during a LOFA. It is theorized that the discrepancy between different RANS models is linked to inaccuracies in the underlying turbulent viscosity assumption for buoyancy-influenced flows. However, due to the lack of comparisons to benchmark quality data, there is no definitive conclusion as to the source of these modeling errors.

The research presented herein focuses on addressing the modeling issues inherent in RANS based models in the calculation of buoyancy-influenced flow regimes. The analysis consists of detailed comparisons against benchmark quality experimental data

[8] and highly trusted Direct Numerical Simulation (DNS) databases [9-11]. The major contributions provided in the current research are three-fold:

1. Investigate the applicability of RANS based turbulence models for the prediction of buoyant flows based on a detailed model validation assessment against benchmark quality data.

2. Provide insight into deficiencies inherent in the RANS modeling paradigm for the prediction of buoyancy-influenced flow regimes using high-fidelity simulation results.

3. Enhance the predictive capability of RANS models for buoyancy-aided flows through a local buoyancy related source term targeted at the inherent deficiencies in the underlying RANS modeling assumptions.

Details regarding these contributions are provided in Chapters II, III and IV while concluding remarks for each are presented in Chapter V. Finally, a discussion on the future of the current work is presented in Chapter VI to further the applicability of the newly developed turbulence model.

CHAPTER II

APPLICABILITY OF COMMON RANS MODELS FOR THE CALCULATION OF TRANSIENT FORCED TO NATURAL CONVECTION

Background

Reynolds Averaged Navier-Stokes (RANS) models have been widely successful in the analysis of thermal fluid systems in many engineering disciplines. The popularity of these models has grown exponentially in industry mostly due to their availability and ease of use in many commercial and open source software packages. However, this often leads to a misconception that each model is equally applicable to all flow regimes, and their availability and convenience has led to the misuse of models in many situations. In reality, each model has a range of applicability and the degree of accuracy will vary for different scenarios. RANS models notoriously have difficulty in reproducing the mean flow and heat transfer within buoyant flow regimes. This is primarily due to the breakdown of fundamental closure assumptions as well as issues in capturing near wall anisotropy with standard wall function approaches [12]. These modeling issues have a profound effect on the uncertainty associated with different models hence the modification and development of more accurate models has been the subject of many research efforts [12-16].

A benchmarking numerical study on the effect of buoyancy within heated vertical pipe flow by You et. al [9] provided direct numerical simulation (DNS) data for several turbulent mixed convection regimes. This study included both buoyancy-aided

(ascending) and buoyancy-opposed (descending) flow configurations, each with four separate cases of increasing buoyancy force. The flow rate is constant in each case while the buoyancy force is altered by increasing the Rayleigh number in the form of a constant heat flux. To ensure a fully developed flow regime, the pipe domain is simplified using translational periodicity in the flow direction. All material properties are kept constant, allowing for isolation of the buoyancy force through the Boussinesq assumption. The study found that in the case of buoyancy opposed flow, the heat transfer is always enhanced due to a local rise in shear-stress near the wall. This rise in shear stress is a product of increased turbulent production in the near wall region which in turn causes turbulent effects to dominate the near wall diffusion and increase heat transfer. However, in the case of buoyancy aided flow, the production of turbulence in the near wall is reduced, resulting in deterioration of heat transfer at higher levels of buoyancy. As the buoyancy force increases with higher Rayleigh numbers, the reduction in turbulent production becomes so severe that a laminarization effect occurs, resulting in significant impairment of heat transfer. In comparison to this DNS data, several researchers performed turbulence model assessments which show that regardless of the level of complexity, the majority of available RANS models fail to accurately recreate the influence of buoyancy on the mean flow and corresponding wall heat transfer [17-19]. This is especially apparent in the case of buoyancy-aided flow, in which very few turbulence models can capture the laminarization effect. In some cases, certain low-Reynolds number variants of the two-equation k - ϵ model reproduced a better representation of the turbulent viscosity, and in turn, the impact of buoyancy on the

mean flow quantities. However, as described in [17], this is primarily due to the poor predictions in turbulent kinetic energy and turbulent dissipation rate being balanced by the low-Reynolds number damping function, rather than providing an accurate, robust model for buoyant flows.

Qualitative comparisons with DNS data provide a good starting point for assessing model performance, however in industrial applications the flow is subject to any number of non-ideal conditions making the resulting model predictions much more difficult. Such an example can be seen in a previous numerical study of the thermal-hydraulics for a Generation-IV nuclear reactor concept during an accident scenario [4]. The accident scenario is based on conditions indicative of a loss of flow accident (LOFA), in which the flow regime changes from downward forced convection to purely natural convection as the flow direction reverses upward through the core, driven by density differences within the heated flow. The combination of variable material properties, strong buoyancy force and complex geometry results in a very challenging flow regime to model. The study examined the performance of four turbulence models as well as a laminar flow model in capturing the resulting heat transfer and flow characteristics during the transient. The results showed that simply by changing the model formulation, the velocity characteristics and most notably the heat transfer varied significantly. Resulting heat transfer rates within the upper plenum varied by upwards of four orders of magnitude between different turbulence models. In a case such as this, it is impossible to make a definitive decision on which model is best suited for this scenario without previously knowing what value to look for. In other words, the predictive

capability for any of these models is truly unknown for this given problem. An assessment of turbulence models can help to determine which turbulence model produces the most desirable results, however due to the purely numerical nature of the study, the results are largely inconclusive in determining the most appropriate model.

While general, qualitative assessments are valuable, a more beneficial and complete analysis would be to perform a model validation study, in which there is quantification of the uncertainty of the solution associated with the model. Model validation studies are essential to properly evaluate the performance and applicability of computational models for different scenarios [20]. Ideally, the simulation's results are compared to a known solution or high-fidelity experimental data. The chaotic nature of turbulent flows excludes the chance to obtain a known solution, while a scale resolving simulation such as LES or DNS is often far too computationally expensive for industrial type flows. This leaves the use of high-fidelity, benchmark quality experiments to validate these models. These validation experiments provide boundary conditions and system response quantities along with a detailed description of the uncertainty in these measurements so that a better comparison between simulation and experiment may be performed. The use of benchmark quality data is crucial in determining the credibility for computational models, especially in cases where the model is used outside the range of its applicability. One such experimental facility central to model validation efforts for buoyant flows is the Rotatable Buoyancy Tunnel (RoBuT) located at Utah State University. The unique design of the facility allows exploration of buoyancy aided and opposed flow conditions using a combination of particle image velocimetry (PIV),

thermocouples and heat flux sensors. The RoBuT facility has been successful in acquiring benchmark quality experimental data for several different flow configurations and conditions [21-23]. One benchmark case in particular attempts to replicate the previously mentioned conditions of a LOFA along a heated vertical plate [8]. To accomplish this, the power to the blower is turned off after achieving steady-state downward forced convection, allowing the flow to gradually transition through mixed and natural convection, in which a full flow reversal is achieved. Data for system response quantities such as velocity, turbulent stresses, heat flux and shear stress are captured at periodic time intervals during the transient providing detailed insight into the flow physics during a flow reversal type situation. The aim of this study is to utilize this benchmark quality data to assess the applicability of some commonly used turbulence models for buoyant flows. In order to accomplish this, the numerical uncertainty for each model is accounted for according to the ASME best practice guidelines [24] so that a validation metric based on the unique cumulative distribution functions (CDF) of experimental and simulation can be determined. This metric is based on the Minkowski distance between CDFs [25] and provides a way of ranking the most appropriate turbulence model during the transient by comparing the dissimilarity between the numerical and experimental distributions. Qualitative comparisons of velocity and turbulent kinetic energy with the experimental values are provided at three separate time steps for the downstream locations provided by the experiment. The time-steps coincide with three distinct events during the transient – the transition from forced to mixed convection, flow reversal, and natural convection. For simplicity, these events are

categorized into Case 1, Case 2 and Case 3 respectively. To support the qualitative comparisons in each case, the validation metric is used at several query points along the line traces and the skin-friction coefficient to determine which model is most appropriate in comparison to the experimental results.

Experimental Facility

The RoBuT is a versatile and unique open loop wind tunnel designed to acquire data that is suitable for CFD model validation. The RoBuT utilizes a Ferris wheel design, in which a rectangular test section is contained within a 4.8 m rotatable wheel. To account for non-isothermal flow conditions, the test section contains one heated wall, heavily instrumented with temperature and heat-flux sensors. The RoBuT is able to rotate 180 degrees, such that the position of the blower and test section can be oriented to accommodate buoyancy aided or opposed flow as well as any intermediate angle between the two configurations. The test section consists of a rectangular channel 2.0 m in length with a cross sectional area of 0.305 m x 0.305 m. One wall is heated while the remaining three are optically clear for ease of data acquisition via particle image velocimetry (PIV). For the heated wall, the actual heated section spans 0.279 m wide and 1.89 m in the flow direction. Six heaters controlled by three separate power supplies are evenly distributed along this length. The heated plate assembly is made of Aluminum 2024 with a nickel-plated surface to minimize the emissivity to 0.03 such that the effect of radiation is negligible. Thermocouples are embedded within 3.18 mm of the aluminum plate surface, followed by heat flux sensors for system response quantities all

contained within the assembly with sufficient insulation such that thermal losses through the walls may be neglected. To capture thermal boundary conditions for computational models, 307 thermocouples are used at the inlet and walls, while hydraulic inlet conditions are captured using PIV.

Prior to the inflow reaching the test section, the flow is conditioned using a series of square rib turbulators, a chilled water radiator, honeycomb flow straightener and two high porosity screens. The flow configuration in this study is the buoyancy opposed case where the conditioned flow accelerates through the contraction and into the test section. The origin for the coordinate system is at the center of the utmost upstream location of the test section, where positive x is in the stream wise direction, positive y is normal to the heated wall and the z-component spans the lateral direction. Aside from capturing the inlet data for boundary conditions, the PIV system is used to capture line traces of velocity and Reynolds stresses from the heated wall to the top of the test section at three stream wise locations downstream from the origin at 0.16, 0.78, and 1.39 m respectively. Further technical detail about the instrumentation used in the experimental facility design and operation is omitted from this study and the reader is directed to [8] for more information.

The transient run is initialized with a steady flow, characterized by the corresponding Reynolds and Grashof numbers at the three downstream locations mentioned above. The Richardson number, Ri_x, is defined as the ratio of buoyant to inertial forces and serves as a very useful parameter while defining the impact of buoyant forces on the flow.

$$Gr_x = \frac{g\rho^2\beta(T_s - T_\infty)x^3}{\mu^2} \quad (1)$$

$$Re_x = \frac{\rho U_{bulk} x}{\mu} \quad (2)$$

$$Ri_x = \frac{Gr_x}{Re_x^2} \quad (3)$$

The flow initialization begins by allowing the heated plate to reach a set point temperature, at which point the blower is turned on and set to the specified flow rate. The initialization is complete once the set point for both the heated plate temperature and the flow rate are maintained for a five-minute period. At this point the data acquisition system deems that steady-state conditions have been met and the blower is shut off and the transient begins. PIV data is taken at a frequency of 5 Hz for a total of 20.2 s as the flow decelerates and eventually reverses due to the increase in buoyant driving force. The data is ensemble averaged over 100-200 runs for each location and time in order to generate reliable values for the mean thermal and flow variables for boundary conditions and system response quantities. The ensemble averaging over m number of repeated runs for a general scalar value u_m, is defined as a function of its phase, Φ.

$$\bar{u}(\Phi) = \frac{1}{N_m}\sum_{m=1}^{N_m} u_m(\Phi) \tag{4}$$

Similarly, in order to calculate the second order quantities, such as the shear component in the Reynolds stresses, $\overline{u'v'}$, both the mean and fluctuating components are required.

$$\overline{u'v'}(\Phi) = \frac{1}{N_m}\sum_{m=1}^{N_m} [u_m(\Phi) - \bar{u}_m(\Phi)][v_m(\Phi) - \bar{v}_m(\Phi)] \tag{5}$$

Ensemble averaged values for temperature are provided for the inlet and walls, as well as x and y components of velocity and their corresponding normal and shear Reynolds Stresses at the inlet and downstream line traces at each phase during the transient. The uncertainty at each point for the thermal conditions and system response quantities is determined based on a 95% confidence interval using the method outlined by Coleman and Steele [26] and defines the bias, random and total uncertainty in the ensemble averaged values. The uncertainties in the PIV measurements are found using a modified method by Timmins et al. [27]. This method creates a surface of uncertainty based on a number of dependent variables taken from the raw PIV images, resulting in a more realistic non-uniform uncertainty estimate. The method proposed by Wilson and Smith [28] is employed to more accurately estimate the uncertainty in the instantaneous values, as to better assess the extent to which they propagate into the mean quantities.

Computational Methodology

The test section for the RoBuT is used as the computational domain for the assessment of CFD models, based on the built dimensions specified by Lance and Smith [8] to maximize the equivalence between the experiment and computational model. The three-dimensional computational domain is discretized into three separate, highly orthogonal, structured grids of increasing element count containing 250,000, 2 million and 6.75 million elements respectively. These grids are chosen such that the resulting refinement factor between each mesh is above the minimum suggested value for use with the Grid Convergence Index (GCI) to assess the error due to spatial discretization [25]. Previous numerical investigations on the RoBuT by Clifford and Kimber [29] and Lance and Smith [30] under similar mixed convection flow conditions have shown that these meshes are sufficient to lower the uncertainty due to discretization to levels below the experimental uncertainty. The simplicity of the geometric model allows for very high-quality mesh to be used, which is especially convenient for near wall modeling. The mesh in the near wall region is highly refined using an initial spacing of 3.048×10^{-5} m which is then smoothly graded into the free-stream using a bi-exponential point distribution [31]. This is done so that the non-dimensional wall distance, y^+, is kept below unity, which is within applicable values for the near-wall modeling and relations used in the computation models chosen. The schematic presented in Figure 2 shows a cross-section view of the computational grid as well as the domain for the CFD model which contains the heated wall section, inlet, outlet and adiabatic

walls. At three locations downstream along the heated wall, line traces are imposed to acquire system response quantities to compare with experiment.

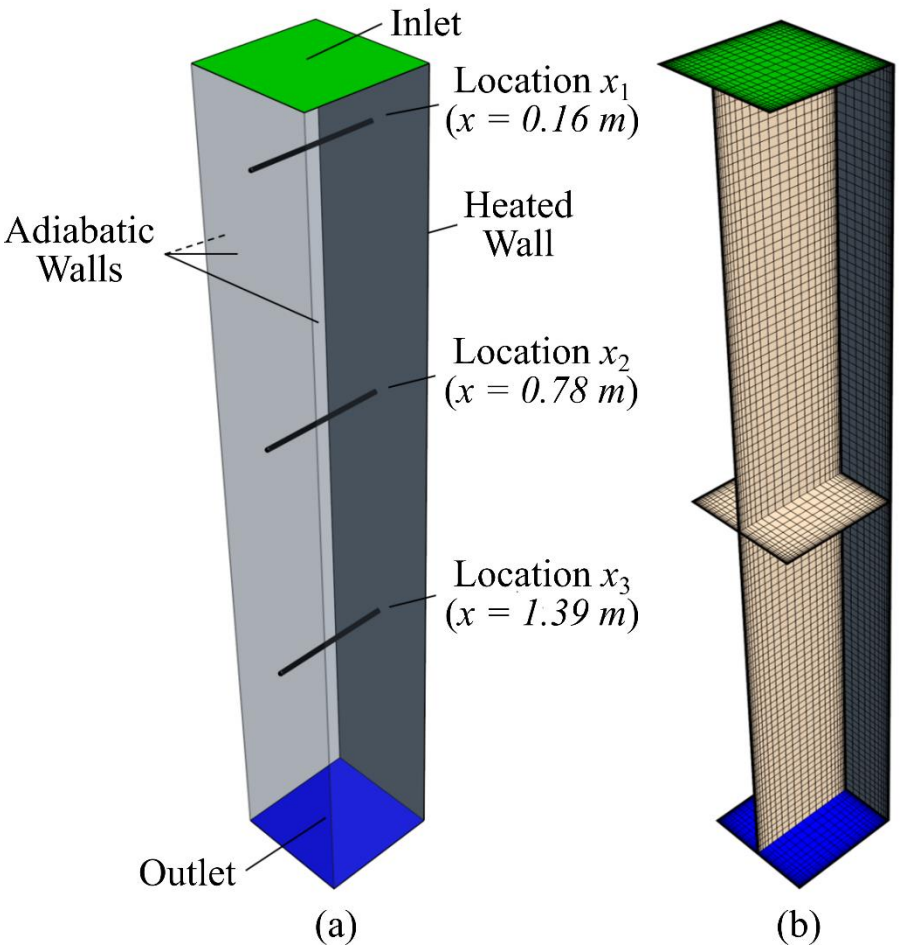

Figure 2: Computational domain for the CFD model (a) and cross-section view of the computational grid (b) for the CFD model.

Governing Equations

The unsteady Reynolds Averaged Navier-Stokes (URANS) form of the equations for continuity, conservation of linear momentum, and conservation of energy take the following form [32],

$$\frac{\partial \rho}{\partial t} + \nabla \cdot (\rho \bar{\mathbf{v}}) = 0 \tag{6}$$

$$\frac{\partial}{\partial t}(\rho \bar{\mathbf{v}}) + \nabla \cdot (\rho \bar{\mathbf{v}} \times \bar{\mathbf{v}}) = -\nabla \bar{p} + \nabla \cdot [\mathbf{T} + \mathbf{R}_{RANS}] + \rho \mathbf{g} \tag{7}$$

$$\frac{\partial}{\partial t}(\rho \bar{E}) + \nabla \cdot (\rho \bar{\mathbf{v}} \bar{E}) = -\nabla \cdot \bar{p} \bar{\mathbf{v}} + \nabla \cdot [(\lambda + \lambda_{RANS}) \nabla T] + \nabla \cdot (\mathbf{T} + \mathbf{R}_{RANS}) \bar{\mathbf{v}} \tag{8}$$

In this representation of the governing equations, the overbar denotes mean quantities while the lowercase represents fluctuating quantities. It is clear to see that this form of the governing equations closely resemble their non-averaged counterparts with the exception of an extra term in the momentum and energy equation, more commonly known as Reynolds stress tensor ($\mathbf{R}_{RANS}$) and turbulent thermal conductivity (λ_{RANS}) respectively. The most common closure method for the Reynolds stress tensor is to introduce an eddy-viscosity to represent the effect of turbulence on the mean flow quantities.

$$\mathbf{R}_{RANS} = 2\mu_t \bar{\mathbf{S}} - \frac{2}{3}\rho k \delta_{ij} \tag{9}$$

The variables μ_t and k represent the eddy-viscosity and turbulent kinetic energy respectively. In a similar fashion, the effect of turbulence on the heat transfer is modeled using a linear constitutive relation based on the turbulent viscosity and the turbulent Prandtl number.

$$\lambda_{RANS} = \frac{\mu_t C_p}{Pr_t} \tag{10}$$

To complete the closure, most turbulence models solve evolution equations for the turbulent kinetic energy as well as a secondary variable such as turbulent dissipation rate (ϵ) or specific dissipation rate (ω). The generic forms of these evolution equations are shown in Equations (11), (12) and (13).

$$\frac{\partial}{\partial t}(\rho k) + \nabla \cdot (\rho k \bar{\mathbf{v}}) = \nabla \cdot \left[\left(\mu + \frac{\mu_t}{sc_k}\right)\nabla k\right] + P_b + P_k - \rho\epsilon \tag{11}$$

$$\frac{\partial}{\partial t}(\rho \epsilon) + \nabla \cdot (\rho \epsilon \bar{\mathbf{v}}) = \nabla \cdot \left[\left(\mu + \frac{\mu_t}{sc_\epsilon}\right)\nabla \epsilon\right] + \frac{\epsilon}{k} C_{\epsilon 1}(P_k + C_{\epsilon 3} P_b) - C_{\epsilon 2}\rho \frac{\epsilon^2}{k} \tag{12}$$

$$\frac{\partial}{\partial t}(\rho \omega) + \nabla \cdot (\rho \omega \bar{\mathbf{v}}) = \nabla \cdot [(\mu + sc_\omega \mu_t)\nabla \omega] + P_\omega - \rho \beta_\omega \omega^2 \tag{13}$$

Where the terms P_k and P_b represent the production of turbulence due to shear and buoyancy respectively, while P_ω corresponds to the production of the specific dissipation rate. The equations above contain numerous constants and coefficients ($sc_k, sc_\epsilon, sc_\omega, C_{\epsilon1}, C_{\epsilon2}, C_{\epsilon3}, \beta_\omega$) defined through empirical relations to encompass a wide range of flow regimes. The above-mentioned equations provide the basis for the majority of eddy-viscosity based RANS models, however, depending on the particular model formulation, the values of these of these coefficients may range from constant values to functions of local flow variables.

Turbulence Models

Several turbulence models have been investigated in this study due to their historical success in resolving mean flow quantities from complex flow conditions as well as their availability and frequent use in both research and industry. This includes variations of the standard two-equation linear eddy-viscosity models (Two-Layer Realizable $k-\epsilon$, $k-\omega$ Shear Stress Transport), low Reynolds number models (Abe-Kondoh-Nagano, v^2f), as well as a full Reynolds Stress Transport model (Elliptic Blending Reynolds Stress Transport Model) to gauge the performance of turbulence models of varying complexity. All of the aforementioned models are standard models available within the commercial CFD software package Star-CCM+ (v. 13.02.011-R8). While several additions to these models such as production limiters and scale corrections are available within the Star-CCM+ framework, special care is taken to ensure that the original formulation provided by the references for each model is preserved. Standard

wall functions are avoided within this study as their underlying local equilibrium assumptions are not valid within complex buoyant flow regimes. Instead, the low y^+ variants of these models are imposed for improved near wall performance.

Two-Layer (Xu) Realizable k-ε (RKE)

The RKE model [33] is a variant of the popular two equation $k-\epsilon$ model that employs a reformulation of the turbulence dissipation rate equation as well as a dynamic formulation for the closure variable C_μ to satisfy realizability constraints to the Reynolds stresses. These additions to the standard model greatly improve the generality of the $k-\epsilon$ model to be applicable for a variety of complex flows. Common to most RANS models, the RKE model utilizes the eddy viscosity assumption to address the influence of turbulence on the mean flow quantities. However, the inclusion of a non-constant C_μ in the definition of the turbulent viscosity heightens the sensitivity of the model to complex flow topologies, greatly improving the prediction of mean flow quantities in comparison to the standard model.

In wall bounded flows, the near wall treatment for turbulent quantities is usually taken care of using the wall function approach. This approach makes use of the local equilibrium assumptions within the logarithmic region in the near wall to impose constraints on turbulence parameters. The wall function approach loosens the constraint on the grid refinement in the near wall region, however in the case of buoyant flows, these assumptions are no longer valid, and the standard wall function approach cannot be used. Instead, a two-layer approach is implemented which uses the standard two-

equation RKE model in the free stream and a one equation model for the dissipation in the near wall. In this study, the one equation model by Xu et al. [16] is used for the near wall dissipation due to its formulation for improved prediction of buoyant flows.

k-ω Shear-Stress Transport Model (SST)

A common criticism of any $k-\epsilon$ based turbulence model is the near wall behavior of the turbulent dissipation rate. In each model, either a wall treatment based on the law of wall or a non-physical damping function must be applied for the turbulent dissipation rate to obey asymptotic behavior at the wall. The low Reynolds number $k-\epsilon$ models, which utilize damping functions in the near wall region, also have a very strict mesh requirement in the near wall region in order to resolve the viscous sublayer. The $k-\omega$ based turbulence models utilize a different secondary variable, specific dissipation rate (ω), which can be resolved through the boundary layer to the wall to avoid the use of standard wall functions [34]. One downfall of the standard $k-\omega$ model however, is the strong sensitivity of the mean flow to ambient or free-stream values.

The shear-stress transport (SST) variant of the standard $k-\omega$ model combines the near wall boundary layer resolution that is inherent in the $k-\omega$ formulation, with the favorable free-stream behavior of the $k-\epsilon$ model. To accomplish this, the standard two equation $k-\epsilon$ model is transformed using a simple substitution between the turbulent dissipation rate, ϵ, and the specific dissipation rate, ω. The transformed model equations are identical to the standard $k-\omega$ model with an additional cross-diffusion term between the turbulent kinetic energy and specific dissipation rate. The SST variant

implements a blending function within the cross-diffusion term, which provides a smooth transition between the $k-\omega$ model in the near wall and the $k-\epsilon$ model in the free-stream. The turbulent viscosity for the SST model variant differs from the standard $k-\omega$ model to include the influence of the shear stress component, similar to the half-equation model of Johnson-King [35], to greatly improve the model performance in the presence of strong adverse pressure gradients.

Abe-Kondoh-Nagano Low-Reynolds Number k-ε Model (AKN)

The AKN model is a low-Reynolds number variant of the standard $k-\epsilon$ model with the inclusion of empirically defined damping functions for near wall treatment of turbulent quantities [36, 37]. The main improvement of the model is based on its redefinition of the friction velocity which is incorporated into the damping functions in the near wall region. This redefinition improves the generality of this model to include better prediction of reattachment and separated flows. In comparison to the standard $k-\epsilon$ models, the near wall resolution of low-Reynolds number models show improved predictions of wall shear stress and heat transfer in complex, wall bounded flows.

v^2f Model (V2F)

The v^2f turbulence model is a variant of the $k-\epsilon$ family of models, but in addition to solving for turbulent kinetic energy and dissipation rate, two extra evolution equations are solved for the wall normal component of stress and an elliptic relaxation function [38-40]. This variant implements a turbulent velocity scale by using the wall normal stress component as opposed to the turbulent kinetic energy. Most low Reynolds number

damping functions attempt to scale the turbulent viscosity to mimic this effect. However, in order to accurately represent the boundary condition at the wall for the normal stress component, an elliptic equation for the relaxation parameter is introduced to account for the non-local wall effects. The addition of these non-local effects at the wall give the v^2f model an advantage over many models in the calculation of near wall behavior such as wall shear stress, heat transfer and areas where transitional flow may occur.

Elliptic Blending Reynolds Stress Model (EB-RSM)

Reynolds Stress Transport models do not impose the same closure as the standard eddy-viscosity models presented in Equation (9), and instead a second moment closure method is used in which the components of the Reynolds Stress tensor are solved directly. The evolution equation for the specific Reynolds stress tensor, **R**, is provided by in (14).

$$\underbrace{\frac{\partial}{\partial t}(\rho\mathbf{R})}_{\substack{Temporal\\ Term}} + \underbrace{\nabla\cdot(\rho\mathbf{R}\bar{\mathbf{v}})}_{Advection} = \underbrace{\mathbf{D}}_{\substack{Reynolds\ Stress\\ Diffusion}} + \underbrace{\mathbf{P}}_{\substack{Turbulent\\ Production}} + \underbrace{\mathbf{G}}_{\substack{Buoyancy\\ Production}} - \underbrace{\mathbf{\Pi}}_{\substack{Pressure\\ Strain}} + \underbrace{\mathbf{E}}_{\substack{Turbulent\\ Dissipation}} \tag{14}$$

This improved closure of RANS equations provides a much more accurate representation of the effect of turbulence on the mean flow by removing the isotropic assumption on the Reynolds stress tensor imposed by standard eddy-viscosity models. The second order closure results in more accurate predictions of complex flows which

are a common deficiency in standard RANS models, however the transport equation for the Reynolds Stresses contains unknowns which must be modeled to close the model. The greatest challenge associated with Reynolds Stress closure is the modeling of the pressure-strain term, which includes the modeling of the fast and slow pressure-strain as well as the wall reflection effects. The model used in this study is the elliptic blending Reynolds Stress model first developed by Manceau and Hanjalic [41] which is based on Durbin's original Reynolds Stress model [39] for improved predictions for wall bounded flows.

Boundary Conditions

The boundary condition data obtained from the experiment is interpolated onto the cell centroids of its counterpart in the computational domain using a triangulation based linear interpolation scheme. Along with the temperature, the velocity components at the inlet are interpolated onto the computational grid. The x and y-components are obtained from the experimental data while equality is assumed between y and z-components. The turbulent quantities from the experiment are presented in terms of the Reynolds Stresses ($\overline{u'u'}$, $\overline{v'v'}$, $\overline{u'v'}$) hence the same interpolation procedure is performed when providing boundary conditions for each component in the Reynolds Stress Model. However, due to the inherent isotropic assumption associated with eddy-viscosity models, individual components of the Reynolds Stresses cannot be used as boundary conditions, so instead the turbulent kinetic energy is used. The turbulent kinetic energy is calculated by using the normal components of the Reynolds Stresses, while the other

relevant turbulent quantities at each cell at the inlet are calculated using the relations below.

$$k = \frac{1}{2}\left(\overline{u'u'} + \overline{v'v'} + \overline{w'w'}\right) \cong \frac{1}{2}\left(\overline{u'u'} + 2\overline{v'v'}\right) \tag{15}$$

$$\epsilon = C_{\mu}^{3/4}\frac{k^{3/2}}{l} \tag{16}$$

$$\omega = \frac{k^{1/2}}{C_{\mu}^{1/4} l} \tag{17}$$

$$v^2 = \frac{2}{3}k \tag{18}$$

In similar fashion, the ensemble averaged temperature is interpolated to cell centroids of the computational grid at each wall. The transient nature of the runs require that the boundary conditions update as the simulation progresses. The experimental data provides boundary conditions at each location as function of phase, i.e., every 0.2 seconds, which corresponds to the data acquisition frequency. In order to ensure a smooth transition between updated boundary conditions, linear interpolation for points sharing the same spatial coordinates between subsequent time steps is employed. While this assumption of linear behavior between time steps may not be completely valid, it provides a more reasonable physical interpretation of the evolution of the boundary

conditions as opposed to step-like changes. The material properties of the fluid are evaluated using high order polynomials presented in Table 1 based on the elevation in Logan, UT as functions of temperature at a constant pressure provided from the atmospheric instrumentation within the experimental facility.

Table 1: Coefficients for the high-order polynomials used for the evaluation of thermophysical properties. [42]

Coefficient	Thermophysical Property			
	Density $(\rho)[\mathrm{kg}\cdot\mathrm{m}^{-3}]$	Dynamic Viscosity $(\mu)[\mathrm{Pa}\cdot\mathrm{s}]$	Thermal Conductivity $(\lambda)[\mathrm{W}\cdot\mathrm{m}^{-1}\cdot\mathrm{K}^{-1}]$	Specific Heat $(C_p)[\mathrm{J}\cdot\mathrm{kg}^{-1}\cdot\mathrm{K}^{-1}]$
a_0	13.7866	-2.9230×10^{-7}	-0018	1444.3975
a_1	-0.2722	7.7361×10^{-8}	1.2036×10^{-4}	-12.7733
a_2	0.0032	3.4928×10^{-11}	3.4782×10^{-7}	0.1820
a_3	-2.6615×10^{-5}	-1.2406×10^{-12}	-9.5329×10^{-7}	-0.0016
a_4	1.5804×10^{-7}	8.7951×10^{-15}	9.8472×10^{-9}	1.0344×10^{-5}
a_5	-7.0672×10^{-10}	-4.1422×10^{-17}	-6.4867×10^{-13}	-4.8080×10^{-8}
a_6	2.4306×10^{-12}	1.4512×10^{-19}	3.0091×10^{-15}	1.6951×10^{-10}
a_7	-6.5025×10^{-15}	-3.9089×10^{-22}	-1.0254×10^{-17}	-4.6030×10^{-13}
a_8	1.3585×10^{-17}	8.1831×10^{-25}	2.6219×10^{-20}	9.6925×10^{-16}
a_9	-2.2099×10^{-20}	-1.3312×10^{-27}	-5.0683×10^{-23}	-1.5139×10^{-18}
a_{10}	2.7711×10^{-23}	1.6678×10^{-30}	7.3834×10^{-26}	1.9823×10^{-21}
a_{11}	-2.6266×10^{-26}	-1.5788×10^{-33}	-7.9862×10^{-29}	-1.8744×10^{-24}
a_{12}	1.8199×10^{-29}	1.0923×10^{-36}	6.2226×10^{-32}	1.2941×10^{-27}
a_{13}	-8.6951×10^{-33}	-5.2122×10^{-40}	-3.3029×10^{-35}	-6.1576×10^{-31}
a_{14}	2.5603×10^{-36}	1.5328×10^{-43}	1.0693×10^{-38}	1.8054×10^{-34}
a_{15}	-3.5014×10^{-40}	-2.0936×10^{-47}	-1.5935×10^{-42}	-2.4584×10^{-38}

Computational Procedure

All simulations are performed using the segregated flow solver available in the commercial software package Star-CCM+ (v. 13.02.011-R8). Star-CCM+ employs a collocated finite-volume formulation which iteratively solves the flow field by using the SIMPLE algorithm to link the pressure and velocity fields. The temperature dependent material properties provide an incompressible, variable density for the calculation of the buoyancy force while the turbulence production due to the effect of buoyancy is modeled using the simple-gradient diffusion hypothesis. Each transient simulation is first initialized by a steady-state simulation based on the boundary conditions at the time $t = 0\ s$. The steady-state solution is deemed converged once the normalized residuals of the model equations reached below the threshold of 1×10^{-10}. Details of the discretization and solver settings for all simulations is presented in Table 2. A second-order upwind differencing scheme is used for convection term in all governing equations while temporal discretization is performed using a second-order implicit backwards differencing method with a time-step size of $\Delta t = 1.25 \times 10^{-3} s$. The time step size is chosen to ensure that the well-known Courant-Friedrichs-Lewy (CFL) condition is kept below unity for all three grids.

$$CFL = \Delta t \left(\sum_{i=1}^{n} \frac{u_{x_i}}{\Delta x_i} \right) \leq 1 \tag{19}$$

Although the use of an implicit time-stepping scheme relieves the dependence on this condition for stability, compliance with this condition ensures that flow information travels only between neighboring cells so that the transient nature of the problem may be approximated as closely as possible. The inner loop iterations of the SIMPLE algorithm continue for each time step until the normalized residuals for each relevant quantity reach below a specified tolerance of 1×10^{-6}. Previous numerical studies have shown that satisfying scaled residual tolerances lower than 1×10^{-6} is sufficient for tight convergence of all relevant quantities [43], hence the convergence criterion for each time step is considered strict enough such that iteration error is negligible. Round off error is also assumed to be negligible due to the use of a double precision solver for all simulations. The transient simulation is then stepped in time from $t = 0 - 18.2\ s$.

Table 2: Simulation settings used in the transient simulations.

Simulation Setting	**Selection**
Simulation Type	3D, Implicit-Unsteady
Solver	Segregated
Material Properties	Temperature-Dependent Polynomial
Pressure-Velocity Coupling	SIMPLE
Turbulence Closure	Reynolds Averaged Navier-Stokes
Momentum Discretization	Second-Order Upwind
Energy Discretization	Second-Order Upwind
Turbulence Discretization	Second-Order Upwind

Numerical and Input Uncertainty Quantification

To assess the credibility of the turbulence models used in this study it is important to quantify the impact that the underlying mathematical assumptions and numerical methodology have on the solution. All models, albeit mathematical or otherwise, are subject to some level of uncertainty. The uncertainty associated with a numerical model typically stems from two sources, numerical uncertainty and input uncertainty. The numerical uncertainties arise from the spatial and temporal discretization of the governing equations, while input uncertainty quantifies the extent in which the model inputs derived from the experiment impact the solution. The discretization of the partial differential equations which govern the system is the first step in obtaining a numerical approximation for a given model. The uncertainty associated with this discretization is greatly impacted by the refinement and structure of the computational grid as well as the numerical scheme implemented for the discretization process. In an ideal situation, the solution will converge asymptotically as the computational grid is further refined, however in some cases the nature of the solution may express oscillatory or other non-asymptotic behavior, causing further complications in assessing the relevant uncertainty. The most accepted method for quantifying the discretization uncertainty is to implement a variation of the Richardson extrapolation through use of the grid convergence index (GCI) proposed by Roache [44]. The GCI method uses the difference in the obtained solutions between systematically refined grids to define the uncertainty in terms of the grid refinement factor and the observed order of accuracy based on a 95% confidence interval [25]. Many challenges are present in using the GCI method for unstructured or

graded meshes, particularly in the calculation of observed order of accuracy. These issues and several others has led to the development of variations to the original GCI method [45-48], leaving discretion up to the user to utilize the most appropriate method. Calculating the discretization uncertainty using the GCI method requires that all query points must have same spatial location. To accomplish this, the solutions obtained on the coarsest and finest grid is interpolated on the medium density grid. The discretization uncertainty for any variable, ϕ, is then calculated using the GCI method,

$$\sigma_{GCI} = \frac{F_s}{r_{21}^p - 1} |\phi_1 - \phi_2| \tag{20}$$

The terms ϕ_1 and ϕ_2 represent the solutions on the finest and medium mesh respectively while F_s provides a factor of safety of either 3.0 or 1.25 depending on whether two or three grids are used in the analysis. To calculate the observed order of accuracy, p, the method outlined by Celik et. al [49] is implemented which iteratively solves the following set of equations,

$$p = \frac{1}{ln(r_{21})} \left| ln \left| \frac{e_{32}}{e_{21}} \right| + q(p) \right| \tag{21}$$

$$q(p) = ln \left(\frac{r_{21}^p - s}{r_{32}^p - s} \right) \tag{22}$$

$$s = 1 * sgn\left(\frac{e_{32}}{e_{21}}\right) \tag{23}$$

To avoid erroneous estimations of the observed order of accuracy commonly caused by any discrepancy between observed and formal order of accuracy, an additional step is implemented as recommended by Oberkampf and Roy [25] . The criteria for this adaptation to the GCI calculation, summarized in Table 3, effectively limits the observed order of accuracy as well as the factor of safety based on its solution to Equations (21), (22) and (23) in relation to the formal order of accuracy.

Table 3: Adaptation for calculation of the observed order of accuracy for standard GCI procedure [25].

$\left\|\frac{p - p_f}{p_f}\right\|$	$\boldsymbol{F_s}$	$\boldsymbol{p}$
≤ 0.1	1.25	p_f
> 0.1	3.00	$min(max(0.5, p), p_f)$

The terms e_{32} and e_{21} represent the difference between two solutions on their corresponding grids ($e_{32} = \phi_3 - \phi_2, e_{21} = \phi_2 - \phi_1$) . Likewise, the grid refinement factors represent the refinement from coarse to finer meshes using a representative cell size based upon the total volume within the domain V, and N number of cells.

$$h = \left[\frac{1}{N}\sum_{i=1}^{N}(\Delta V_i)\right]^{\frac{1}{3}} \tag{24}$$

$$r_{21} = \frac{h_2}{h_1}; r_{32} = \frac{h_3}{h_2} \tag{25}$$

The grids are chosen such that the system response quantities for the steady state solution are expected to converge monotonically with further refinement. While it is difficult to ensure that the same convergence behavior occurs at every time step in such a long transient, the strict convergence tolerance and conservative time step selection aims to drive the solution to replicate this behavior as best as possible. In fact, the GCI methodology requires that the solution lies within this asymptotic region, otherwise the grid should be further refined until monotonic convergence is achieved. Certainly not all solutions will exhibit this ideal convergence behavior, hence this method encounters problems when dealing with solutions which do not converge monotonically, especially those which exhibit oscillatory convergence. It is not uncommon for there to be oscillatory behavior within the asymptotic region for problems which contain complex physics, leading to an overestimation of the discretization uncertainty using the GCI method. Even with this overestimation, the mean discretization uncertainty along each line trace is very small, hence these data points are not filtered out and the resulting discretization uncertainty is regarded as a conservative estimate. The GCI method is applied to the previously mentioned computational grids of 250,000, 2 million and 6.75

million elements for all turbulence models and subsequent system response quantities during the transient. Figure 3 shows the observed convergence behavior for the EB-RSM for both velocity and turbulent kinetic energy at downstream location $x_2\left({}^{x}/_{L} = 0.2\right)$ for $t = 3.0\ s$. The convergence for both quantities shows a smooth monotonic trend while the similarity between the two finest grids provides further justification for the grids used in this study. The average discretization uncertainty for velocity at this time step is 0.33% of the mean value and 2.18% for the turbulent kinetic energy. While this is only a small sample of the acquired simulation data, the convergence trends as well as the magnitude of the spatial discretization uncertainty is representative of the results for the remaining turbulence models throughout the transient. In addition to the spatial discretization, the discretization of the temporal term for transient analyses may introduce additional numerical uncertainties. The temporal discretization uncertainty is largely impacted by the underlying discretization scheme as well the size of the time step imposed to march the solution. While the magnitude of the temporal discretization uncertainty is often quite small in comparison its spatial counterpart [25], several works have stressed the importance of its inclusion in the quantification of numerical uncertainty [50-52]. Similar to the difficulties mentioned in calculating the discretization uncertainty using the GCI method, these studies also recognize this practice may be considerably more difficult for non-idealized flow conditions, such as the conditions experienced in the current study. Due to the small time step size ($CFL_{MAX} < 1.00$) and strict convergence criteria used in the current investigation, the magnitude of the

temporal discretization uncertainty is not expected to be significant in comparison to spatial discretization or input uncertainty.

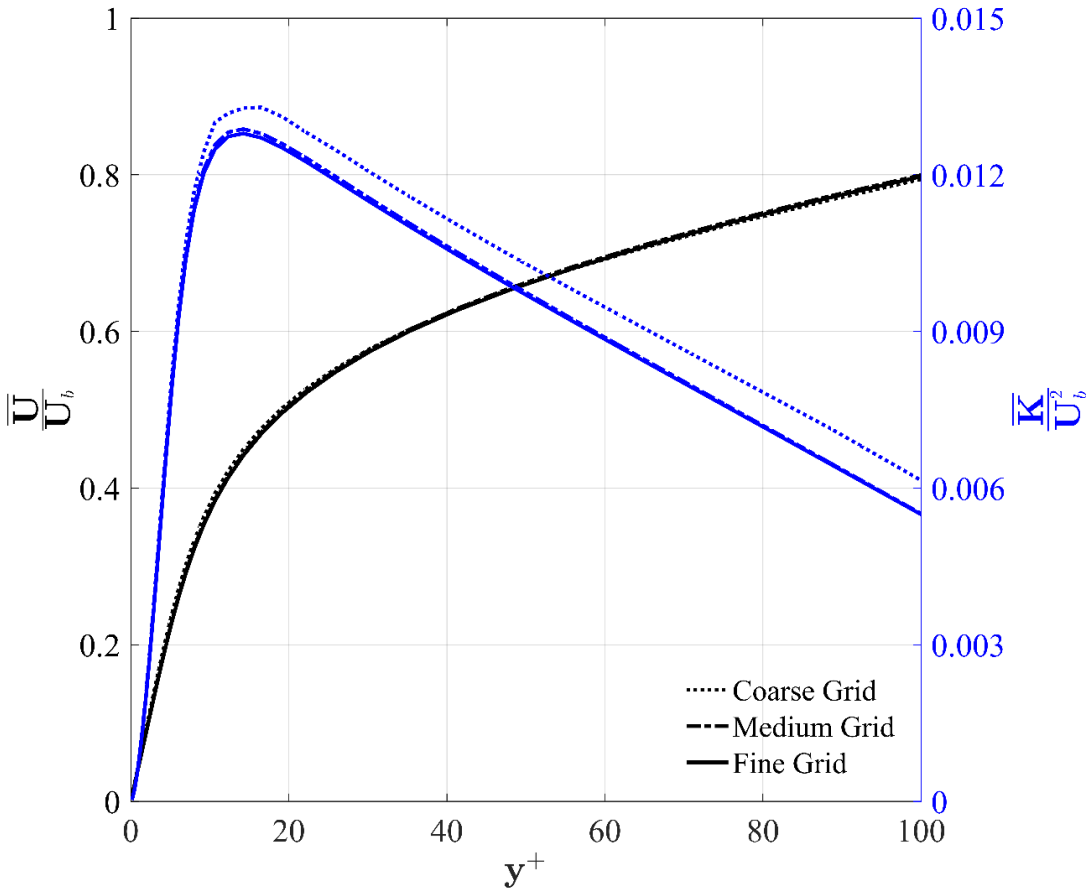

Figure 3: Convergence behavior of velocity and turbulent kinetic energy with increasing grid size for the EB-RSM at the second downstream at location $\boldsymbol{x_2}\left(\boldsymbol{x/L = 0.2}\right)$ for $\boldsymbol{t = 3.0\ s}$.

To investigate the validity of this assumption, the transient simulation is performed using two separate time-steps ($\Delta t = 1.25 \times 10^{-3}\ s$ and $\Delta t = 6.25 \times 10^{-4}\ s$) on the medium

density grid with the SST model. In order to assess the congruence between the two solutions, the skin-friction coefficient is monitored at the three downstream locations (x_1, x_2, x_3) for all time-steps. The relative differences between time-steps is found to be insignificant throughout the transient, reaching a maximum of 1.58% over the entirety of the transient. The average relative difference between the two solutions at each time-step throughout the transient is an order of magnitude lower than this maximum value at 0.16%. These marginal differences indicate a low sensitivity to different time-step size, therefore, the temporal discretization uncertainty is neglected in the current investigation.

The numerical solution is also impacted by the uncertainty in the experimental values which are used as inputs to the model in the form of boundary conditions. To consider how these various inputs impact the simulation globally, the Latin hypercube sampling method is applied to each experimental data point used as an input to the simulation. Using this method, a random sample is chosen from the CDF of each experimental data point, which is divided into bins of equal probability. The LHS method greatly reduces the number of samples required for statistical convergence in comparison to an equivalent Monte Carlo method with simple random sampling. In this study, the CDF for each experimental data point is divided into 100 bins, resulting in 100 separate simulations per turbulence model. Due to the similarity between the solutions for the medium and fine density grids, the aforementioned simulations are all performed on the medium density grid. The accumulation of these solutions for each model creates a unique discontinuous EDF for all system response quantities at each query point within

the domain. Assuming that each discontinuous EDF is appropriately defined using a normal distribution based on a 95% confidence interval, the corresponding input uncertainty for any variable ϕ can then be calculated using the standard definitions for the mean and variance of a variable based on N_{LHS} number of samples.

$$\bar{\phi} = \frac{1}{N_{LHS}} \sum_{i=1}^{N_{LHS}} \phi_i \tag{26}$$

$$\sigma_{INPUT}^2 = \frac{1}{N_{LHS}} \sum_{i=1}^{N_{LHS}} (\phi_i - \bar{\phi})^2 \tag{27}$$

The large computational expense required for the calculation of the input uncertainty negates the feasibility to apply the LHS method for the entirety of the transient simulation. Such a calculation, compounded by the number of models investigated and the inevitable convergence issues from imposing a wide range of randomized boundary conditions, requires significant simplifications in order to become a viable option within the current investigation. Instead, the LHS procedure is only carried out for the steady-state solution at $t = 0\ s$ and applied for all time steps for the model validation procedure. This simplification provides an appropriate compromise based on the premise that the randomized conditions imposed at the boundaries are able to propagate through the entire domain and the effects of the input parameters on the system response quantities downstream may be quantified. The two independent source of uncertainty,

discretization uncertainty (GCI) and the input uncertainty (LHS), can then be used to calculate the model validation uncertainty for each model by taking the sum of the square of each component [24].

$$\sigma_{VAL} = \sqrt{\sigma_{GCI}^2 + \sigma_{INPUT}^2} \tag{28}$$

Generally speaking, for a systematically refined structured grid such as this case, the resulting discretization uncertainty is insignificant in magnitude when compared to the input uncertainty.

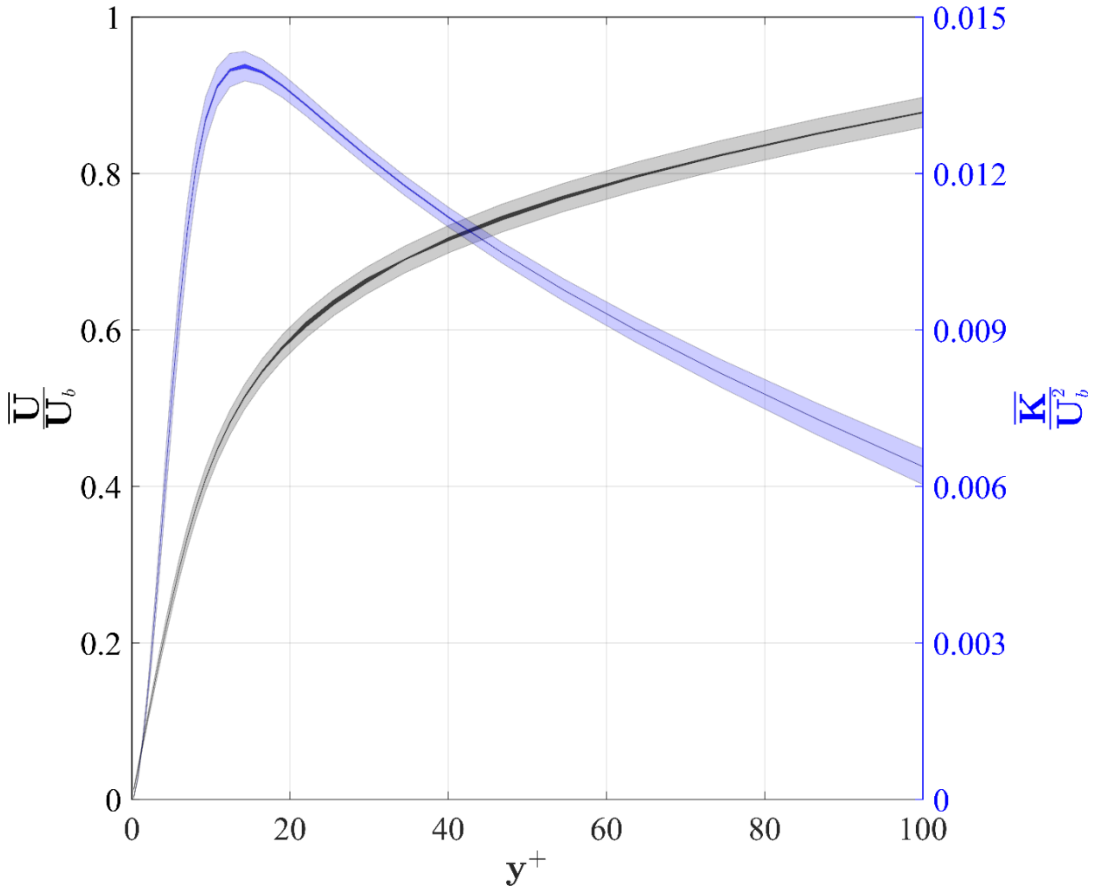

Figure 4: Corresponding uncertainty bands for discretization (solid) and total uncertainty (shaded) for velocity and turbulent kinetic energy for the EB-RSM at the second downstream location $\boldsymbol{x_2\left(x/L = 0.2\right)}$ for $\boldsymbol{t = 0\ s}$.

Figure 4 shows the difference in discretization and total uncertainty for the turbulent kinetic energy and velocity at the second downstream location $x_2\left(x/L = 0.2\right)$ for $t = 0\ s$. The discretization uncertainty, represented by the solid areas, is insignificant in comparison to the total numerical uncertainty denoted by the large shaded regions.

Validation Metric

The goal of any validation study is to be able to quantify the accuracy of a given model through use of a comparative metric based on its performance in reproducing important system response quantities. This metric can vary from purely qualitative comparisons to a full quantification of statistical disparity between model and experiment. Discretion in choosing the fidelity of this metric is dictated by the amount of information present in the empirical data as well as the experience of the modeler to conduct a meticulous numerical investigation. In the case where the results from both the experiment and numerical models are deterministic in nature, the accuracy of a model can be quantified mathematically by taking the relative difference between the two values. However, purely deterministic comparisons are not indicative of true, observable quantities from experimental measurements. Every data point is associated with some uncertainty and contains its own unique distribution of possible values. A simple yet useful way to compare these stochastic results is by using the area metric [53]. This metric is based on the Minkowski distance between the empirical distribution function (EDF) and the CDF based on the possible values for the numerical and experimental results, respectively.

$$\Delta_{\phi} = \int_{-\infty}^{\infty} |N(\phi) - E(\phi)| \, d\phi \tag{29}$$

The calculation of Equation (29) is significantly simplified by assuming a continuous normal distribution for each function based on a 95% confidence interval. The corresponding confidence bounds for the CDF is defined using standard deviation based on the maximum uncertainty at each experimental data point while the bounds for the simulation EDF is defined using Equation (28). A graphical representation of Equation (29) can be seen in Figure 5, where the shaded area provides a measure of disparity between the two distributions, while taking into account their respective shapes. The integral is evaluated numerically using the trapezoidal rule with the upper and lower bounds defined as three standard deviations of maximum and minimum of the numerical or experimental mean. Evaluating the integral in the bounds of three standard deviations is deemed suitable as it encompasses 99.7% of the data from the EDF and CDF. The remaining data within the tails of the distributions is not significant enough to have an impact on the validation results. The magnitude of the area between the two distributions is arbitrary if presented on its own, however when these areas are presented for several models, it provides a relative comparison to rank the most suitable models. The result which encompasses the smallest area is deemed the closest representation of the empirical results, with a value of zero being an exact match.

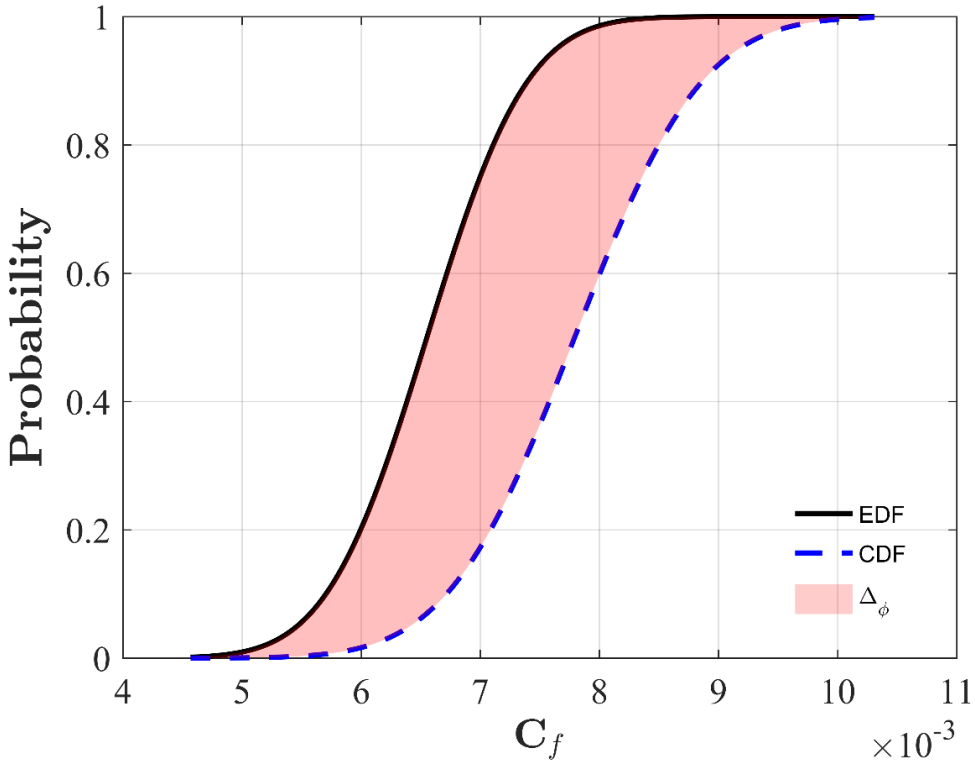

Figure 5: Graphical representation of the area metric used for the comparison of CDF's.

Results

The simulation results are divided into three different cases due to the spectrum of flow regimes involved during the transient to provide an efficient manner in which to digest the results. The first case spans from $t = 0 - 6$ s and involves the decelerating period for the flow, taken directly after the power to the blower is shut off. While the buoyancy force is increasing as the flow decelerates, the majority of this case is well within the forced convection regime. The final two cases comprise the time intervals from $6 - 12$ s and $12 - 18$ s, respectively. The flow physics that occur during case two are the most complex as the flow continues to decelerate and buoyancy begins to dominate as the

primary driving force. The flow momentarily passes into the laminar regime, followed by a full reversal of the flow direction driven by strong density gradients and lack of inertial driving force. Finally, during the third case, the flow develops into fully turbulent natural convection. Qualitative comparisons between the experimental and numerical models is presented for the turbulent kinetic energy and mean velocity profiles for the region close to the heated wall as a function of y^+ calculated using the experimental wall shear stress. To support these qualitative observations, the area validation metric is applied at every third data point along the experimental line traces for all system response quantities. To maintain continuity with the numerical and input uncertainty calculations, all comparisons presented herein are based on the numerical solutions on the medium density grid. The results from the area metric along each line trace is presented for each point during the specified time step, as well as the sum of these values to compare the statistical equivalence between each model and experiment. In addition, for each case, the area-based validation metric is imposed on the skin friction coefficient, derived from the wall shear stress.

$$C_f = \frac{\tau_{wall}}{\frac{1}{2}\rho U_b^2} \tag{30}$$

$$\frac{\sigma_{C_f}}{C_f} = \sqrt{\left(\frac{\sigma_{\tau_{wall}}}{\tau_{wall}}\right)^2 + \left(\frac{\sigma_\rho}{\rho}\right)^2} \tag{31}$$

The uncertainty for this derived quantity is calculated by propagating the uncertainty in the wall shear stress and density as shown in Equation (31). The uncertainty in the wall shear stress is calculated using Equation (28), while the uncertainty in the density is found by evaluating its corresponding polynomial based on the maximum and minimum deviations from the mean temperature at that location. The area metric is evaluated at locations x_1, x_2 and x_3 and summed for each at all time steps within each case. This provides further comparative ranking of the turbulence models in the forced convection, flow reversal, and natural convection regime separately to better assess their performance throughout the transient. Ideally, the same validation metric would be used for the heat flux, however in comparison to the experimental data, the results from the numerical models are vastly different in both shape and magnitude. This can be explained by investigating the design of the heated wall and the location of the heat-flux sensor. The heat-flux sensor is located below the surface of the 3.18 mm aluminum face plate which is kept at a constant temperature. However, the thermal mass of the aluminum plate corresponds to a very large thermal time constant ($\tau > 400\ s$) and acts as a low-pass filter for the heat-flux sensor. Due to the thermal considerations of the aluminum plate, as well as the location of the heat flux sensor, the experimental set-up is unable to accurately capture the temporal evolution of the surface heat-flux over such a small period of time (18.2 *s*). The numerical approach required in such a case represents a significant increase in simulation resources since a conjugate heat transfer model would be run. The computational requirements for the current work are already quite extreme, and a further increase is not desirable.

Case 1 - (t = 0 – 6 s)

As mentioned above, the first case involves the deceleration of the flow as the fan within the blower begins to slow down. Table 4 shows the range of values for both the Reynolds and the Richardson number at each location downstream during this period of the transient. During this time, there is a significant decrease in the Reynolds number at all locations due to the diminishing inertial driving force from the blower. As a result, the effect of the buoyancy force begins to grow, causing the local Richardson numbers to increase by an order of magnitude.

Table 4: Flow characteristics during Case 1 - ($\boldsymbol{t = 0 - 6\ s}$)

$\boldsymbol{x(m)}$	$\boldsymbol{Re_x(t = 0\ s)}$	$\boldsymbol{Re_x(t = 6\ s)}$	$\boldsymbol{Ri_x(t = 0\ s)}$	$\boldsymbol{Ri_x(t = 6\ s)}$
0.16	23,000	8,210	0.027	0.217
0.78	112,000	40,024	0.129	1.011
1.39	201,000	71,325	0.231	1.832

The results for Case 1 include both velocity (Figure 6, Figure 7 and Figure 8) and turbulent kinetic energy (Figure 9, Figure 10 and Figure 11) at $t = 5.0$ s for all three downstream locations. In each figure, the simulation results are presented against the experimental data with corresponding uncertainty bands for qualitative evidence of the accuracy for each quantity, while the markers along the experimental line traces

represent the query points used in the area validation metric. In the early onset of the transient, the mean velocity at each location downstream is well characterized by most models. This is mainly due to the flow being well within the forced convection regime which is typically the most applicable for RANS turbulence models. The one outlier to this trend is the RKE-Xu model, which in this case uses a one-equation model for the dissipation in the near wall which is specifically designed for improved performance for buoyant flows. The generality for this model seems to be quite poor, which can be seen in the velocity prediction at the first downstream for $t = 5\ s$ at location x_1 in Figure 6(a). Even 5 seconds after the fan is shut off, the first downstream location is still very much within the forced convection regime and compared to the other models, the velocity prediction for the RKE-Xu differs in both shape and magnitude. This discrepancy is clearly represented by the area metric along the line trace in Figure 6(b) where the under prediction of velocity in the freestream by the RKE-Xu model corresponds to larger disagreement with the otherwise tight grouping of the other models. Qualitatively, velocity at the other two downstream locations, shown in Figure 7(a) and Figure 8(a), seem to be well predicted by all models in terms of shape but the magnitude is slightly under predicted. At all three locations, the results of the area validation metric show that the AKN model shows the highest level of congruence with the experiment, particularly at the furthest downstream location $x_3(^{x}/_{L} \sim 0.70)$, which shows excellent agreement in the near wall. The poor velocity predictions by the RKE-Xu model may be explained by the vast over estimation of the turbulent kinetic energy in the near wall region. This behavior, which is likely a result of the dissipation equation in

the near wall region tuned for buoyant flows, is most noticeable in Figure 9(a). While some of the other models such as the EB-RSM, marginally over predict this system response quantity in the near wall (Figure 9(b)) the overall prediction of the line trace shown in Figure 9(c), is on par with all other models with the exception of the RKE-Xu. Minus the over prediction in turbulent kinetic energy at x_1 for the RKE-Xu model, all of the models seem to coincide well enough with the experiment to lie within the uncertainty bands in Figure 10(a) and Figure 11(a). The large uncertainty bands corresponding to the experimental results for turbulent quantities is attributed to the difficulty in acquiring a sufficient number of samples for the ensemble average of transient phenomena. Many of the same observations from comparing the turbulent kinetic energy and velocity plots can be confirmed by using the modified area metric shown in Figure 12 for the skin friction at all time steps in Case 1. The V2F model, similar to the RKE-Xu model, performs best at increasing levels of buoyancy, while the SST model outperforms all other models in the forced convection regime at position x_1. The most well-rounded models at all positions are the EB-RSM model and AKN model. For the Reynolds Stress model, this comes as no surprise due to its second moment closure formulation which improves performance in complex flows such as regime change. In the case of the AKN model, the near wall formulation for low-Reynolds number models aids in the prediction or onset of a change in flow regime for wall bounded flows.

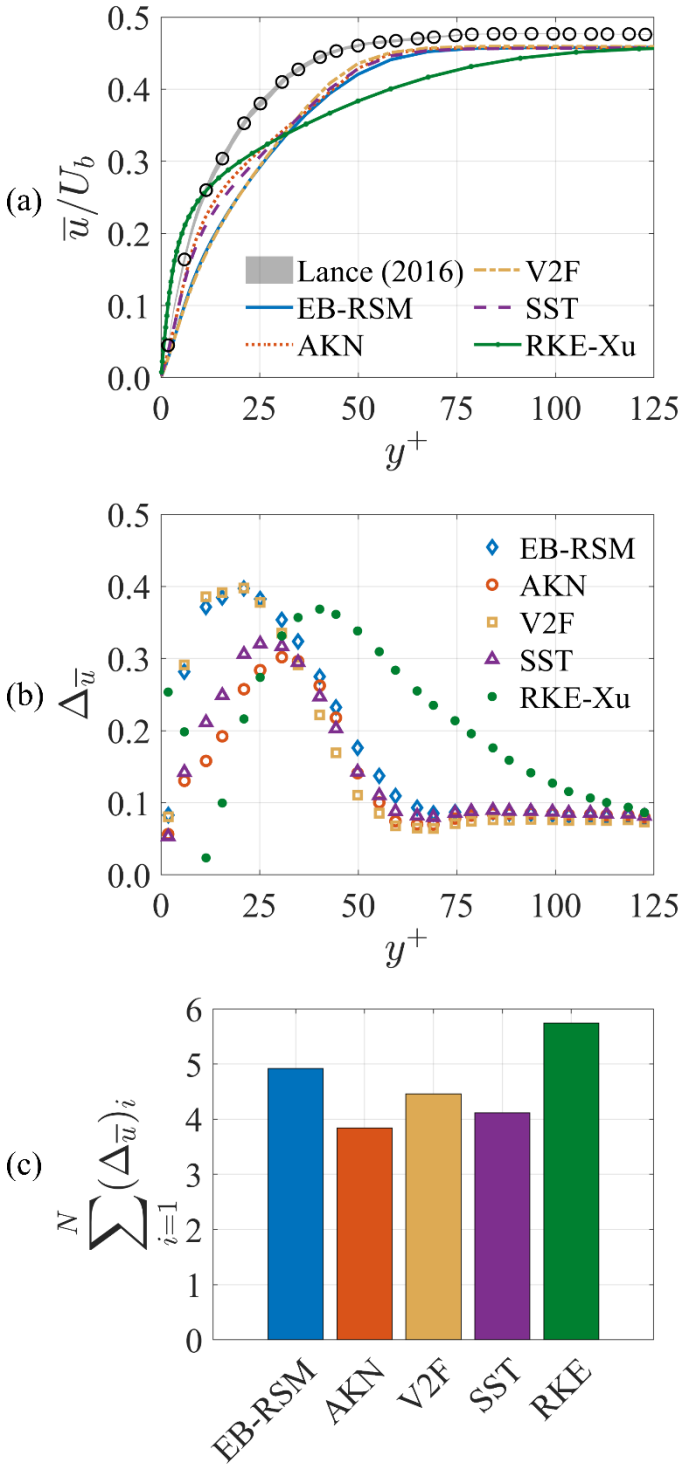

Figure 6: (a) Velocity, (b) results of the area metric at query points, and (c) summation of area metric along the line trace at location $\mathbf{x_1}(\mathbf{x}/\mathbf{L} \sim \mathbf{0.08})$ at $\mathbf{t = 5.0\ s}$.

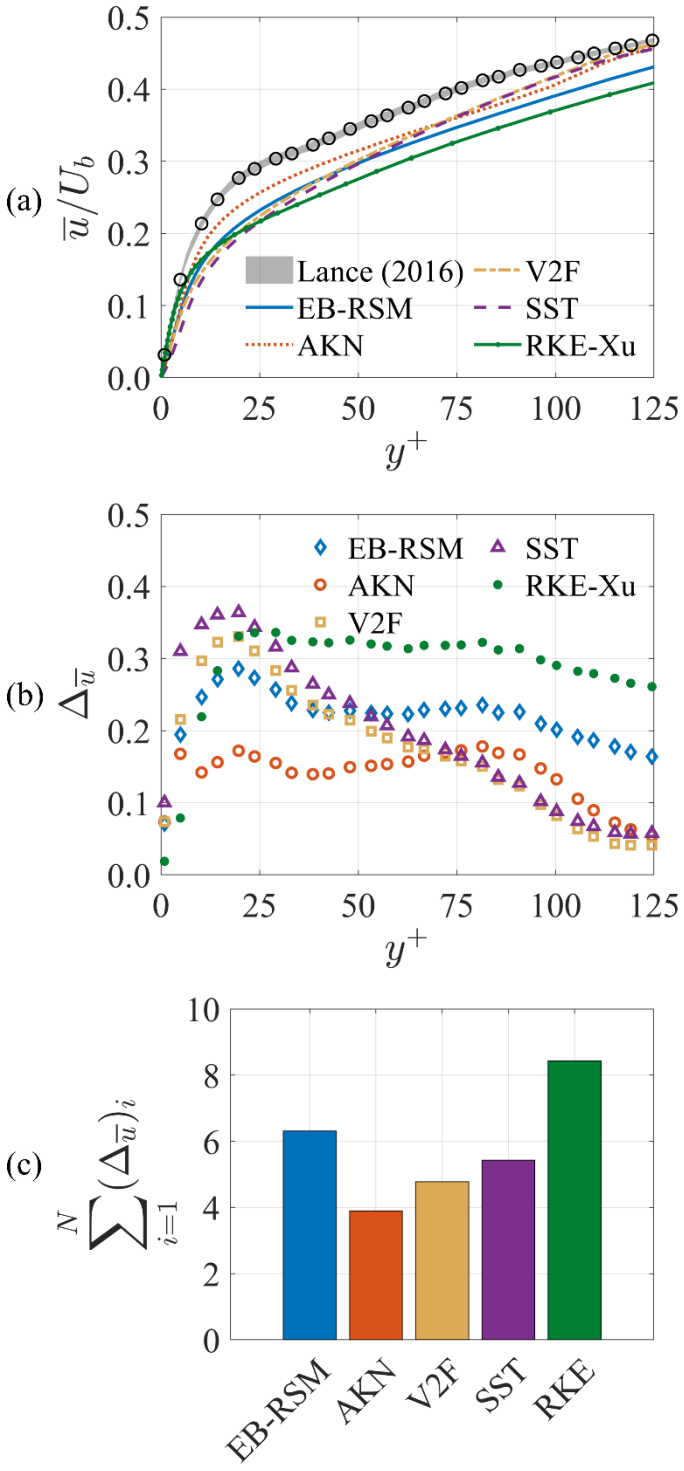

Figure 7: (a) Velocity, (b) results of the area metric at query points, and (c) summation of area metric along the line trace at location $\mathbf{x_2}(\mathbf{x}/\mathbf{L} \sim \mathbf{0.20})$ at $\mathbf{t = 5.0\ s}$.

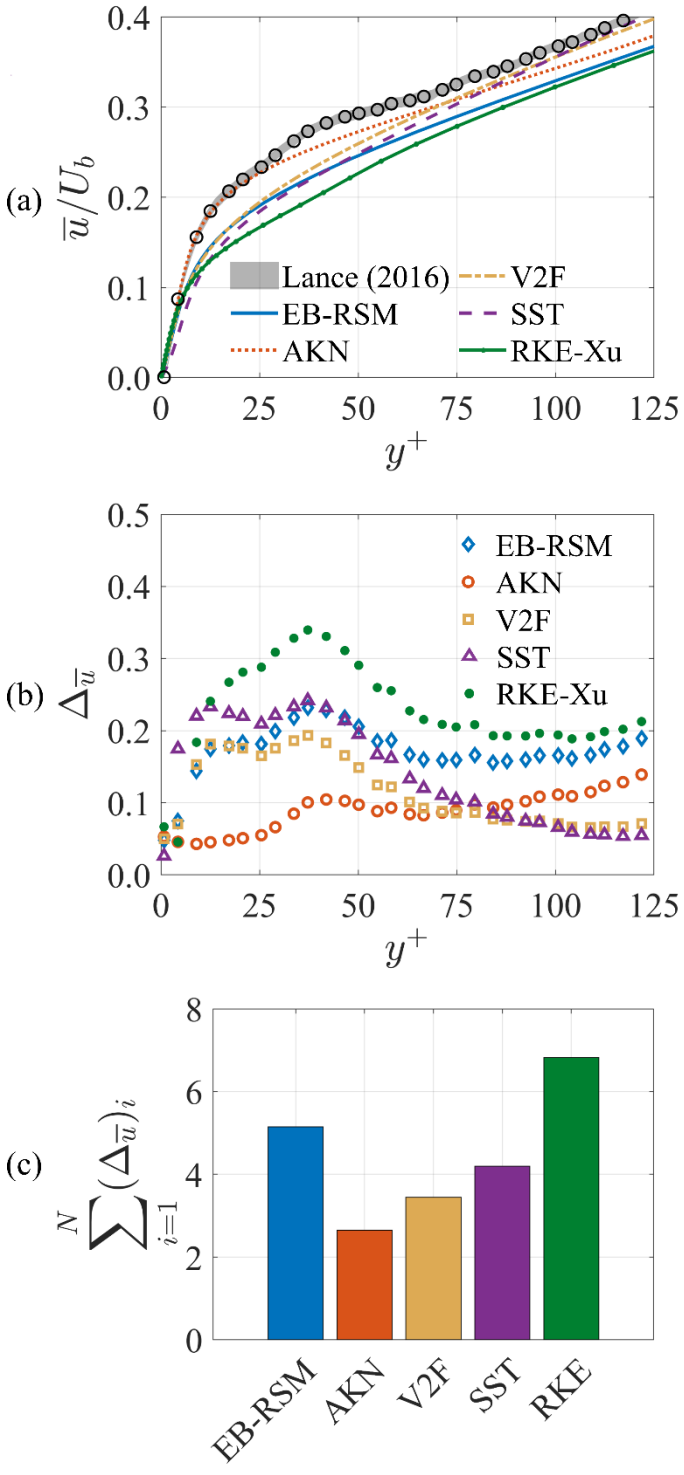

Figure 8: (a) Velocity, (b) results of the area metric at query points, and (c) summation of area metric along the line trace at location $\boldsymbol{x_3}\left(\boldsymbol{x}/\boldsymbol{L} \sim \mathbf{0.70}\right)$ at $\mathbf{t = 5.0\ s}$.

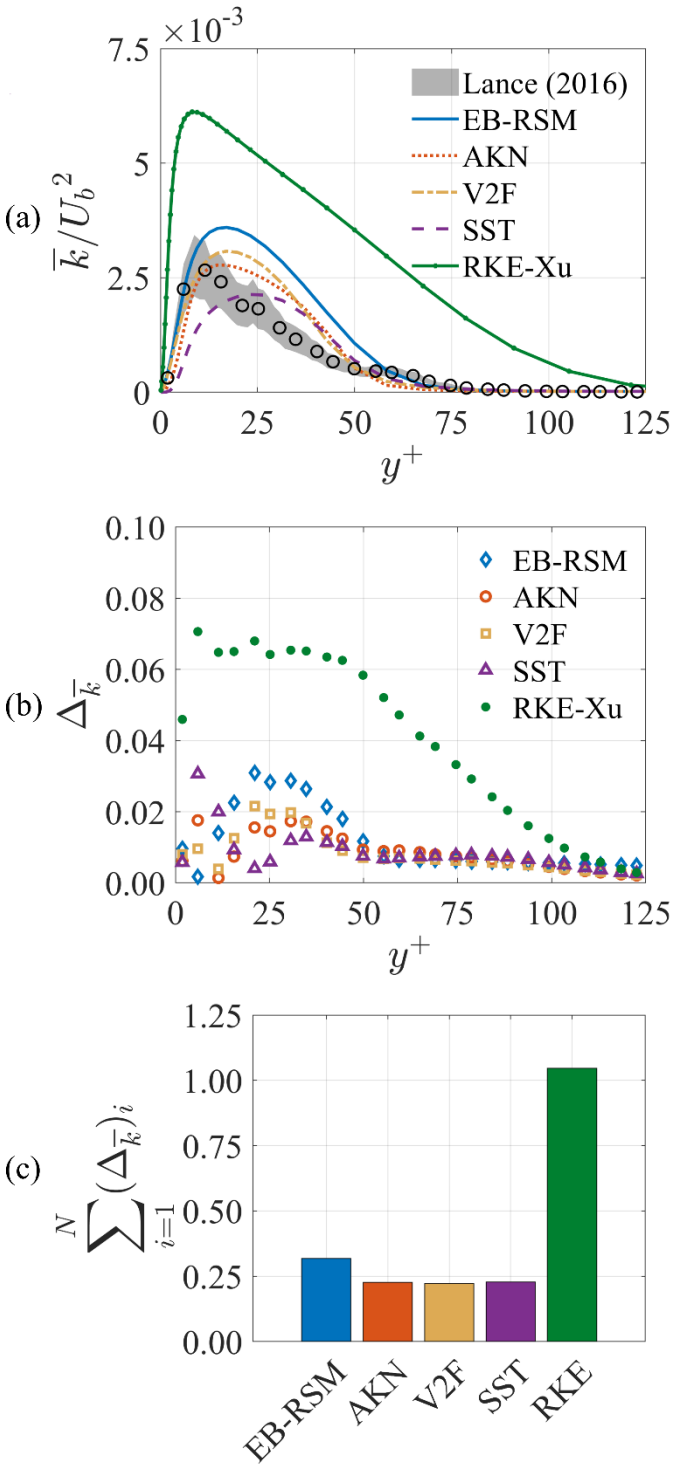

Figure 9: (a) Turbulent kinetic energy, (b) results of the area metric at query points, and (c) summation of area metric along the line trace at location $\boldsymbol{x_1}(\boldsymbol{x}/\boldsymbol{L} \sim \mathbf{0.08})$ at $\boldsymbol{t} = \mathbf{5.0}\ \boldsymbol{s}$.

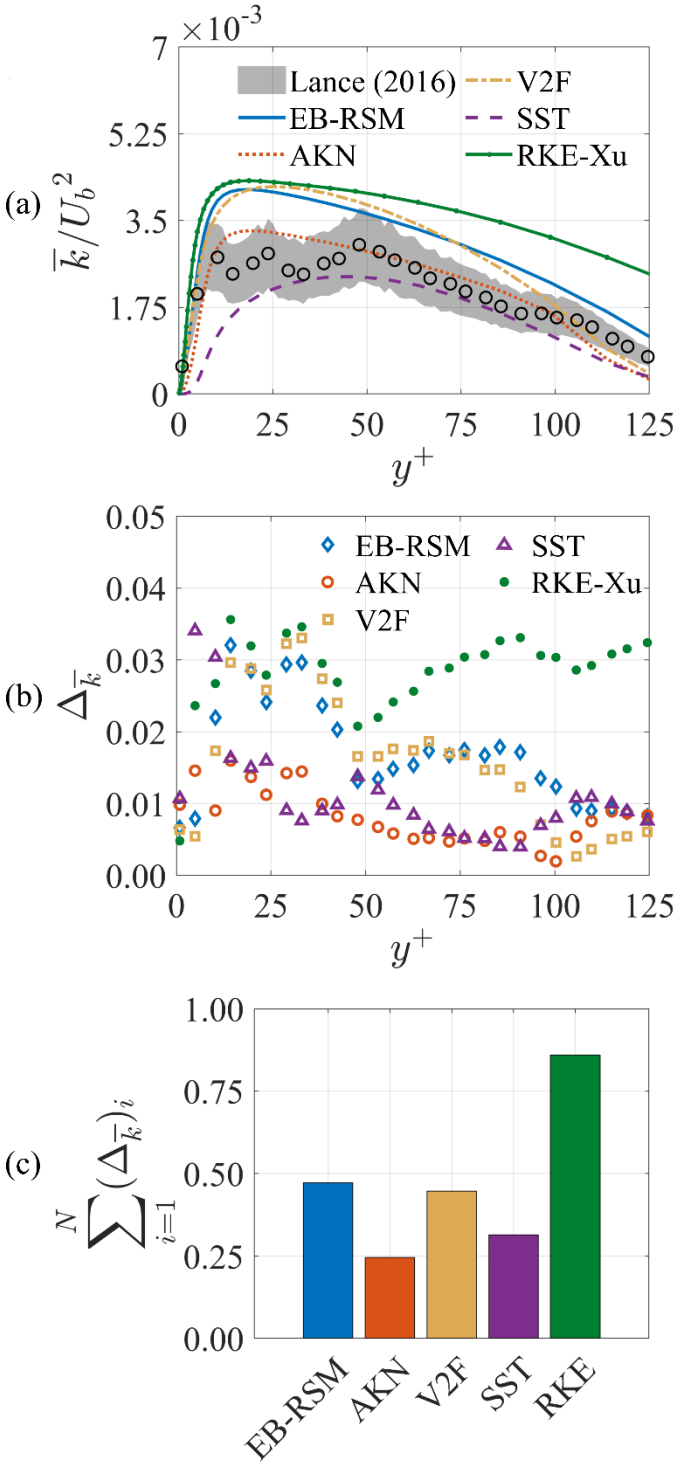

Figure 10: (a) Turbulent kinetic energy, (b) results of the area metric at query points, and (c) summation of area metric along the line trace at location $\mathbf{x_2}(\mathbf{x}/\mathbf{L} \sim \mathbf{0.20})$ at $\mathbf{t} = \mathbf{5.0\ s}$.

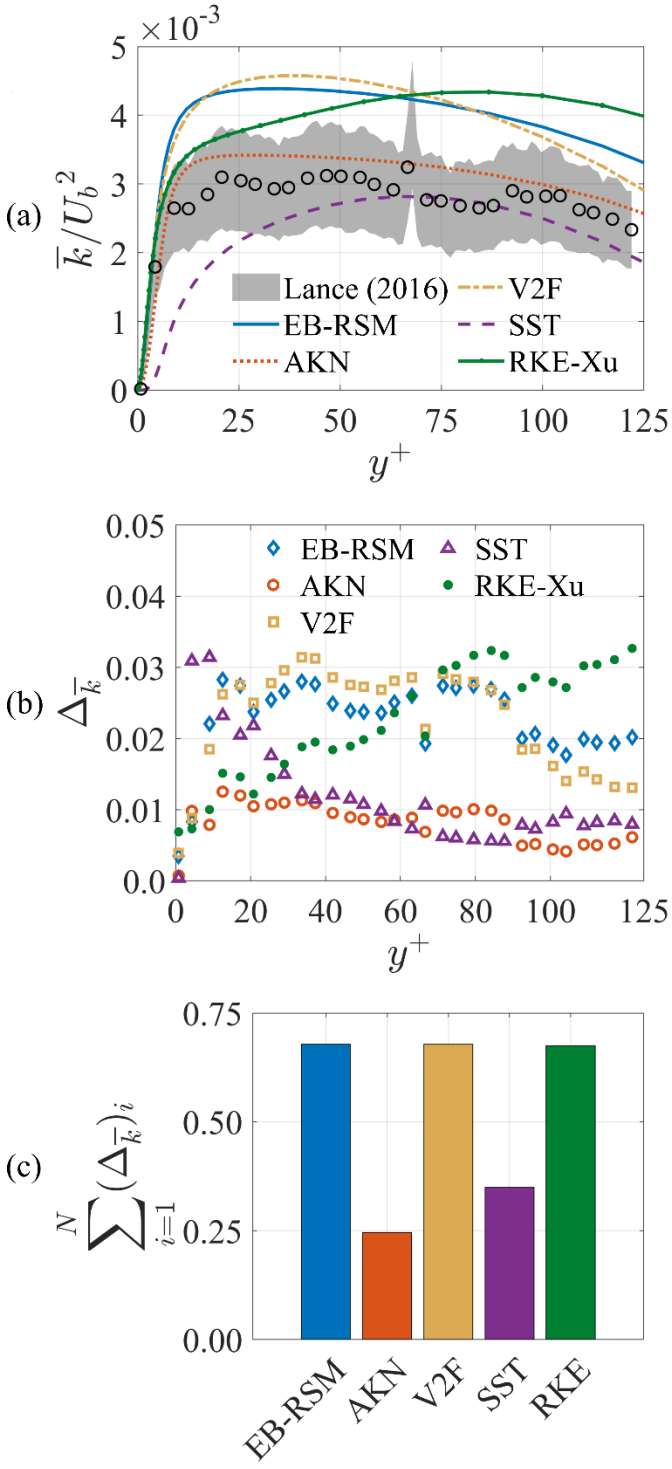

Figure 11: (a) Turbulent kinetic energy, (b) results of the area metric at query points, and (c) summation of area metric along the line trace at location $\mathbf{x_3}(\mathbf{x}/\mathbf{L} \sim \mathbf{0.70})$ at $\mathbf{t} = \mathbf{5.0\ s}$.

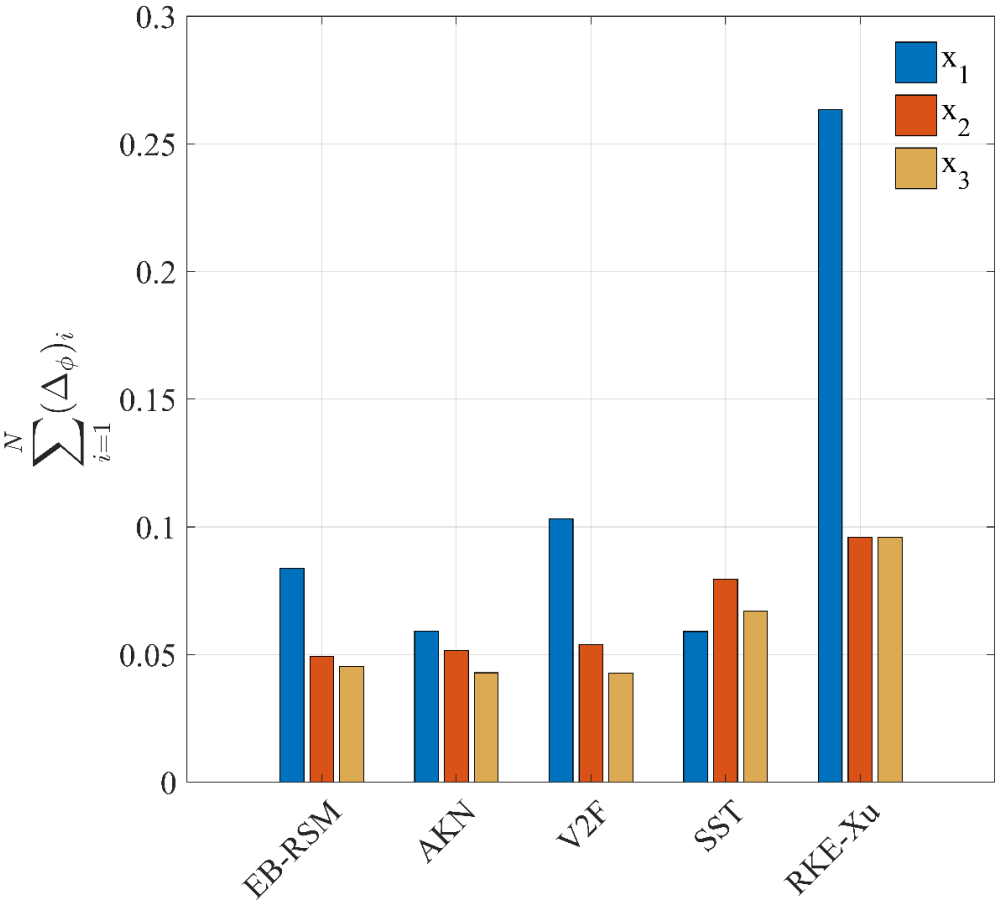

Figure 12: Results of the area metric for the skin friction coefficient for t = 0 – 6s.

Case 2 - (t = 6 – 12 s)

The second case involves the most complex physics during the transient as the ratio of inertial to buoyant forces diminishes to the point of a full flow reversal. As previously mentioned, more intricate turbulence models have had some success in the prediction of transitional flow regimes, however in this case the flow undergoes not only a change in regime but also direction. The latter requires a period of stagnation for at least an instant prior to the change of direction, in which the flow then accelerates due to a strong buoyant driving force near the heated wall. The results for the velocity after the occurrence of the flow reversal are shown Figure 13, Figure 14 and Figure 15 at $t = 10\ s$ of flow time for the three downstream locations. It is clear that the velocity prediction for EB-RSM during this time is quite poor, especially at x_2 and x_3 downstream positions, where the model grossly underestimates the mean free stream velocity. Similar behavior is exhibited by the AKN model at the x_2 position, which is confirmed with the area metric along the line trace in Figure 14(b) and Figure 14(c). While the values themselves are arbitrary, their relative magnitudes suggest that at this particular time step, the dissimilarity between the experimental results and the predictions by the AKN and EB-RSM model is more than two times that of the other RANS models. This is in contrast to the velocity predictions for the RKE-Xu model which has recovered well from the previous predictions in the forced convection regime to provide a much-improved representation of the resulting mean flow. While there is some consistency in the velocity predictions for the SST and RKE-Xu model at the three downstream locations, the more sophisticated models have a much more sporadic range

of over and under prediction. The turbulent kinetic energy at the downstream locations shown in Figure 16, Figure 17 and Figure 18 follows similar trends as in Case 1, making it difficult to ascertain the source of the erroneous velocity predictions. The AKN model, which exhibits highest similarity to the experiment at the x_2 position shown in Figure 17(b) and Figure 17(c) exhibits the complete opposite behavior in terms of velocity shown in Figure 14(b) Figure 14(c). Conversely, the V2F model at the same position (x_2) has excellent agreement with experiment for velocity according to Figure 14(b) and Figure 14(c), however the results for the area metric for the turbulent kinetic energy (Figure 17(b) and Figure 17(c)) shows significantly higher dissimilarity to the experiment than the other models. This disconnect between the predictions of these system response quantities for the same model shows that there is a complex interplay between modeled quantities which is not shown simply with comparisons of these system response quantities. In the case of the two-equation eddy-viscosity models, this interplay boils down to how well the combination of predictions of turbulent kinetic energy and turbulent dissipation rate can produce a turbulent viscosity which appropriately quantifies the amount of turbulence within the flow. As the models become more complex (V2F, EB-RSM etc.) there are more contributing variables, which complicates the matter of troubleshooting discrepancies in the model.

The RKE-Xu model still over predicts the turbulent kinetic energy in comparison to the experimental results, however in this case the over prediction is isolated very close to the wall, ($y^+ < 10$). This behavior is not shared by any of the other models, leaving reason to believe that the empirically tuned near wall treatment is the culprit. The two-

layer wall treatment uses a blending of the turbulent viscosity between the one-equation model in the near wall and the two-equation model to ensure smooth transition between the two regions. It is possible that this unphysical shape of the turbulent kinetic energy is a result of poor blending of the turbulent viscosity within the region due the change in flow regime.

It is likely the poor predictions during Case 2 are caused by the complex physics present during this time in the transient, however, the assumptions about the value of the inlet conditions may also contribute to this behavior. As mentioned previously, the PIV measurements for the boundary conditions provided data in the x (stream-wise) and y (normal to the heated plate) directions, while the z-component for velocity is assumed to be equal to the y-component. This assumption is not uncommon, and has been utilized with success in the same experimental facility [23]. However, in this case, as the flow begins to slow down, the magnitude of the y-component of velocity begins to approach the magnitude of the x-component, in which the assumption of equality between the y and z components has no foundation. Without detailed knowledge of the third direction, it is challenging to accurately represent the flow conditions at the inlet. This is especially apparent in the times near the flow reversal where the velocity in the stream-wise direction becomes completely stratified. In this case, it is difficult to pinpoint whether the poor predictions are due to the inability of the model to reproduce the impact of buoyancy on the mean flow, or an inaccurate representation of the boundary conditions which gets progressively less accurate as the flow becomes more complex. Regardless, the overall accuracy of all models is negatively impacted during this time in the

transient. The results for the validation metric for Case 2 in Figure 19 show that the second downstream location, x_2, has the highest dissimilarity from the empirical results for all models except for the EB-RSM. While the free stream velocity predictions are poor for the EB-RSM, its unique elliptic blending of the pressure strain in the near wall region gives this model superior prediction of the near wall velocity gradients. This improvement over the other turbulence models to replicate the inhomogeneous wall effects during this time can be seen at all locations downstream.

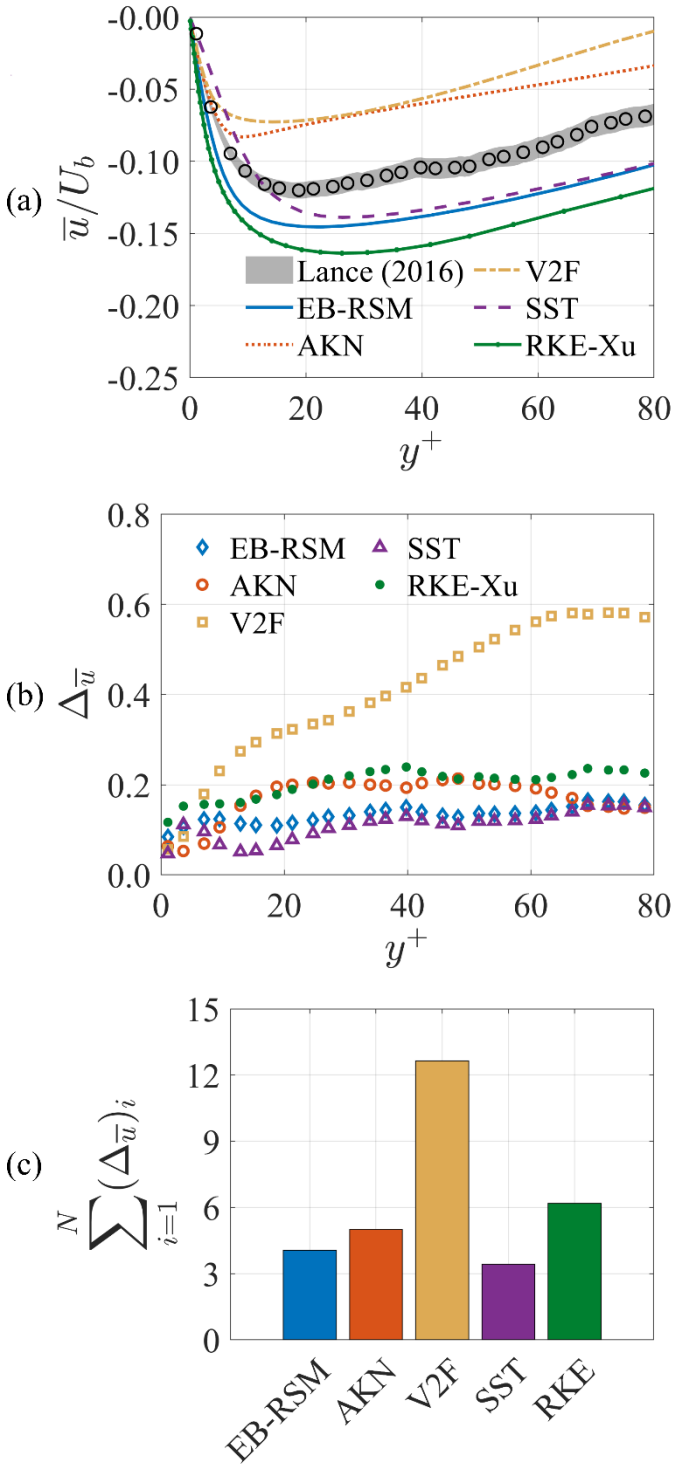

Figure 13: (a) Velocity, (b) results of the area metric at query points, and (c) summation of area metric along the line trace at location $\mathbf{x_1}\left(\mathbf{x}/\mathbf{L} \sim \mathbf{0.08}\right)$ at $\mathbf{t = 10.0\ s}$.

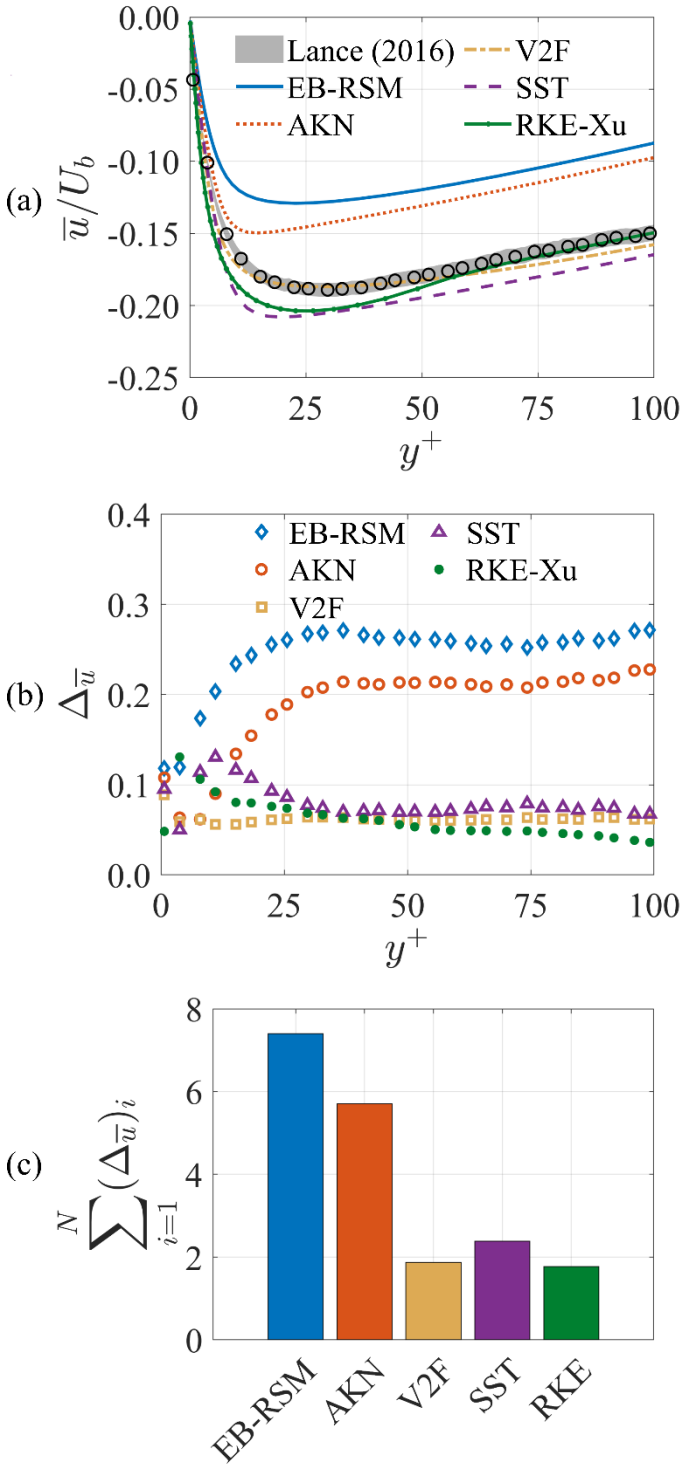

Figure 14: (a) Velocity, (b) results of the area metric at query points, and (c) summation of area metric along the line trace at location $\mathbf{x_2}\left(\mathbf{x}/\mathbf{L} \sim \mathbf{0.20}\right)$ at $\mathbf{t = 10.0\ s}$.

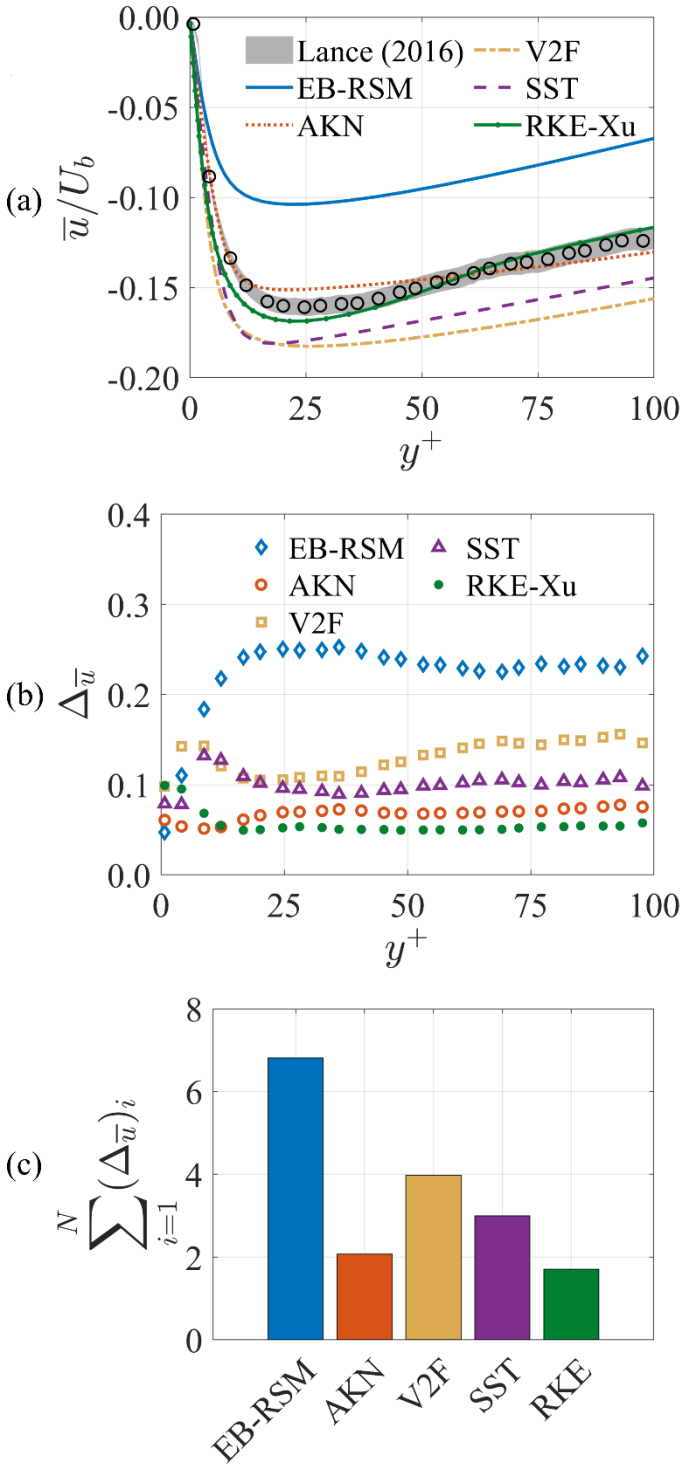

Figure 15: (a) Velocity, (b) results of the area metric at query points, and (c) summation of area metric along the line trace at location $\mathbf{x_3}(\mathbf{x}/\mathbf{L} \sim \mathbf{0.70})$ at $\mathbf{t = 10.0\ s}$.

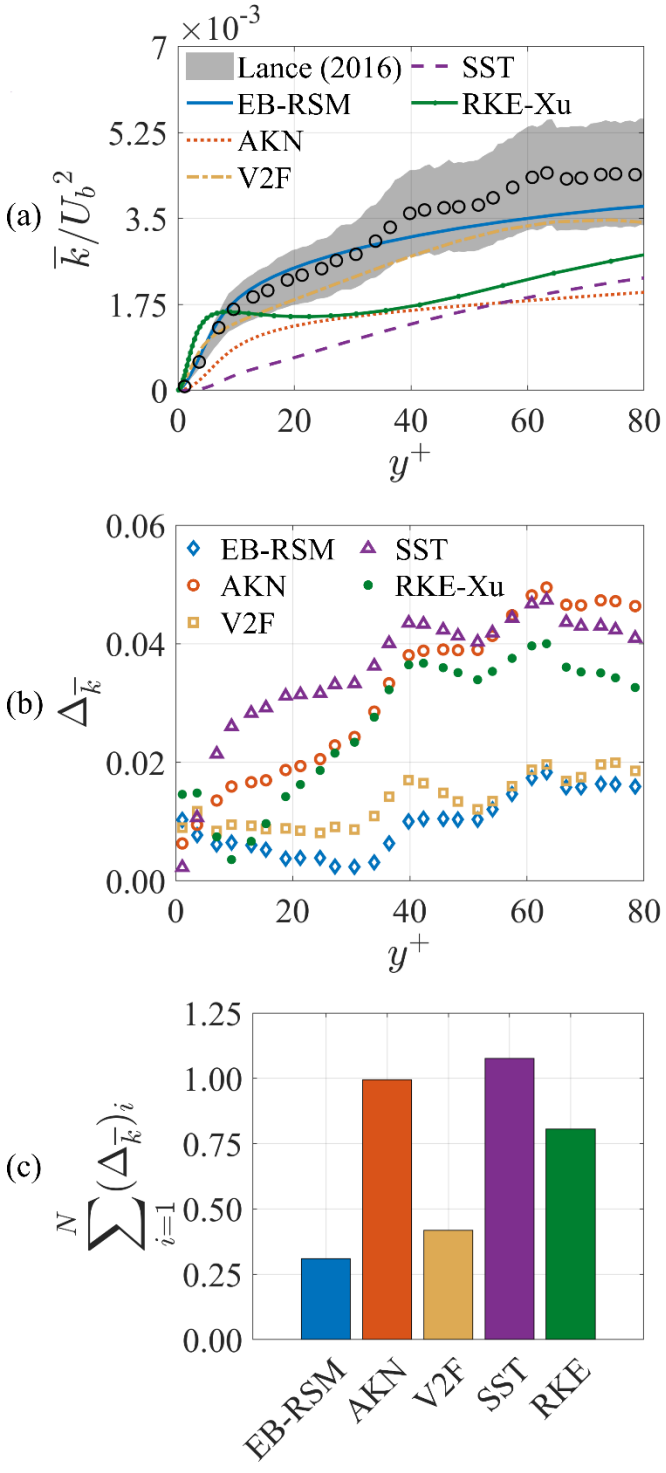

Figure 16: (a) Turbulent kinetic energy, (b) results of the area metric at query points, and (c) summation of area metric along the line trace at location $\mathbf{x_1}(\mathbf{x}/\mathbf{L} \sim \mathbf{0.08})$ at $\mathbf{t} = \mathbf{10.0\ s}$.

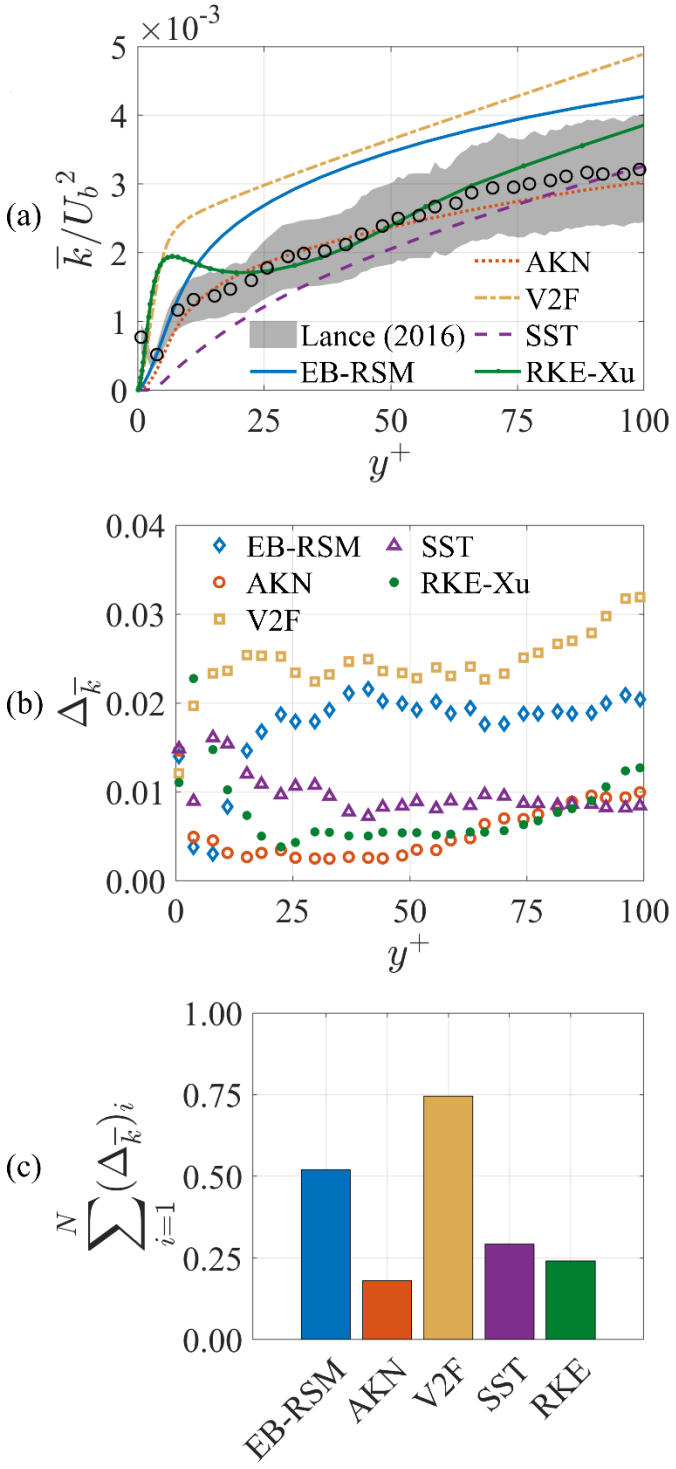

Figure 17: (a) Turbulent kinetic energy, (b) results of the area metric at query points, and (c) summation of area metric along the line trace at location $\mathbf{x_2}(\mathbf{x}/\mathbf{L} \sim \mathbf{0.20})$ at $\mathbf{t} = \mathbf{10.0\ s}$.

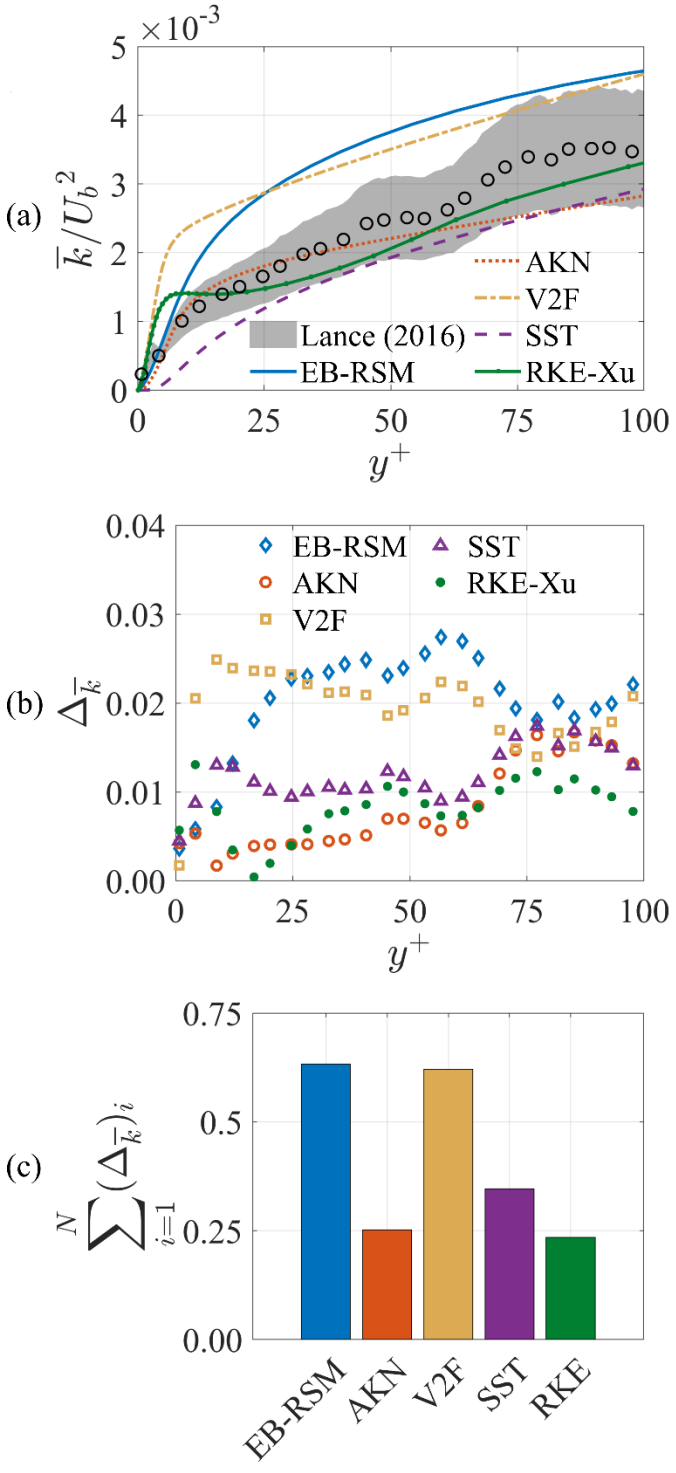

Figure 18: (a) Turbulent kinetic energy, (b) results of the area metric at query points, and (c) summation of area metric along the line trace at location $\mathbf{x_3}(\mathbf{x}/\mathbf{L} \sim \mathbf{0.70})$ at $\mathbf{t} = \mathbf{10.0\ s}$.

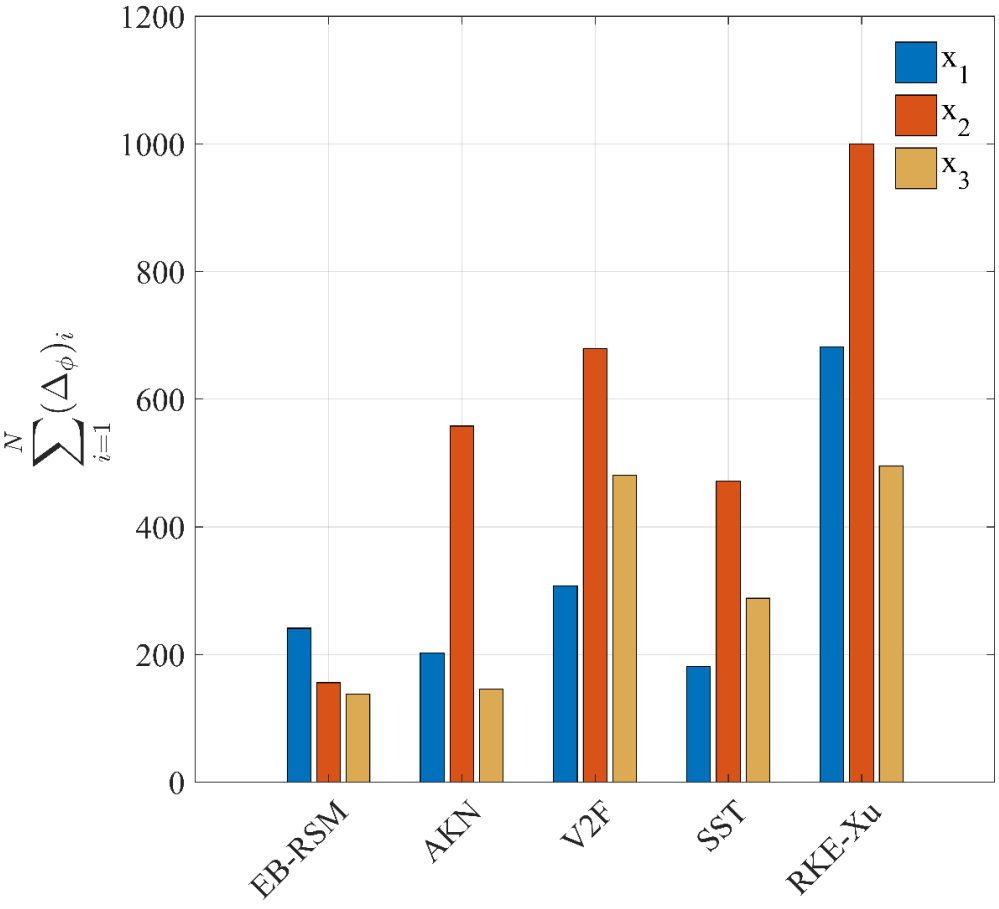

Figure 19: Results of the area metric for the skin friction coefficient for t = 6 – 12s.

Case 3 - (t = 12 – 18.2 s)

The final case takes place after the flow reversal, as the flow along the heated plate develops into turbulent natural convection with flow exiting through the top of the test section. The mean velocity profiles at $t = 15s$ in Figure 20(a), Figure 21(a) and Figure 22(a) show that the EB-RSM is in excellent agreement with the experimental results while all other models seem to over predict the free-stream velocity. This observation is shown most clearly by the area metric in Figure 20(c) where the monotonic trend of the graph highlights the performance of the EB-RSM in capturing this particular system response quantity. In Figure 20(b), both the AKN and V2F models produce comparable values to the EB-RSM for the area metric in the near wall, however the predictions begin to deviate from the experimental values as they approach the free stream. The over prediction velocity is most apparent at the second downstream location, x_2, where the maximum velocity for the RKE-Xu model is roughly twice that of the experimental results. As a consequence, the sum of the area metric in Figure 21(c) shows that the dissimilarity between experimental result and the RKE-Xu model is roughly four times higher than the EB-RSM and double the results from the AKN and SST. The difficulties at the x_2 location may be due to a transitional region along the heated plate as the flow is transitioning to fully turbulent natural convection. This behavior is not as pronounced close the flow boundaries at locations $x_1$and x_3, perhaps due to influence from the boundary conditions. Interestingly, the RKE-Xu model performs quite poorly in the natural convection regime, despite the use of near wall treatment tuned for improvement in buoyant flows. The empirical nature in which the model is developed proves to be

detrimental to the generality and applicability for different scenarios. The AKN and EB-RSM each perform well in predicting the turbulent kinetic energy shown in Figure 23, Figure 24 and Figure 25 while the V2F model provides reasonable predictions in comparison to the previous case. In particular, at the x_1 location the results of the area metric in Figure 23(b) and Figure 23(c) show that the difference in overall prediction between the AKN and V2F model is marginal, despite an over prediction in the near wall similar to the RKE-Xu model. The SST model, which is formulated for highly turbulent forced convection flows, under predicts the turbulent kinetic energy at all locations to the point where it lies outside of the large uncertainty bands in the experimental data. The under predictions in turbulent kinetic energy for the SST score similarly to the over predictions for the same system response quantity in the V2F and RKE-Xu model in the area metric in Figure 23(b) and Figure 24(b). This under prediction of turbulent kinetic energy for the SST model is not uncommon, and has also been observed by other authors for the same model under buoyancy influenced flow conditions [29]. The most striking contrast to the experimental results is the RKE-Xu model however, expressing a much different shape than the logarithmic distribution characteristic of the other models. Not only does the RKE-Xu model seemingly over predict the turbulent kinetic energy in the near wall, it also under predicts the turbulent kinetic energy in the free stream. These erroneous predictions from the RKE-Xu model are also apparent in the results for the validation metric in Figure 26, scoring higher than all other models in every downstream position. The problems observed in the velocity prediction at the second downstream position, x_2, are also present in the near wall

gradients, which can be seen in the high values for the area metric. At all other downstream locations, the SST and AKN model provide comparable results for the area metric in comparison to the EB-RSM, while the V2F model underperforms in the natural convection regime.

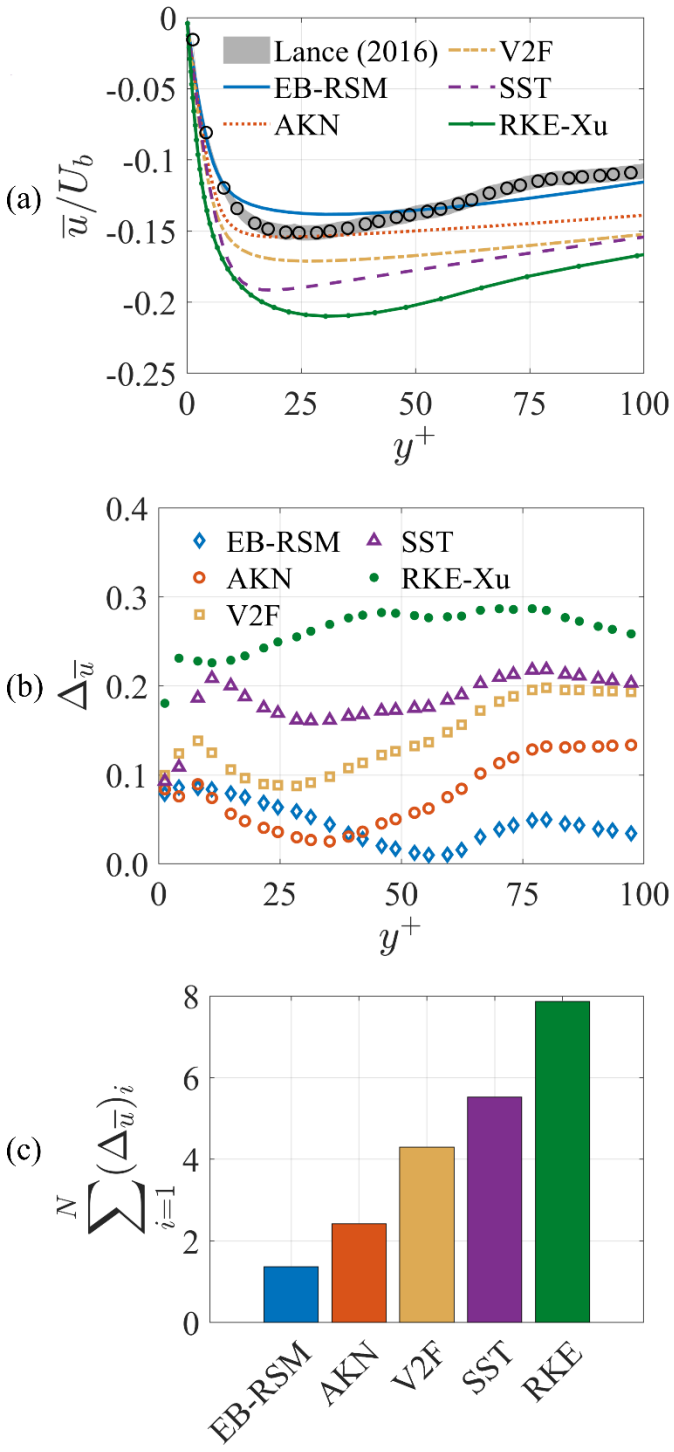

Figure 20: (a) Velocity, (b) results of the area metric at query points, and (c) summation of area metric along the line trace at location $\mathbf{x_1}(\mathbf{x}/\mathbf{L} \sim \mathbf{0.08})$ at $\mathbf{t = 15.0\ s}$.

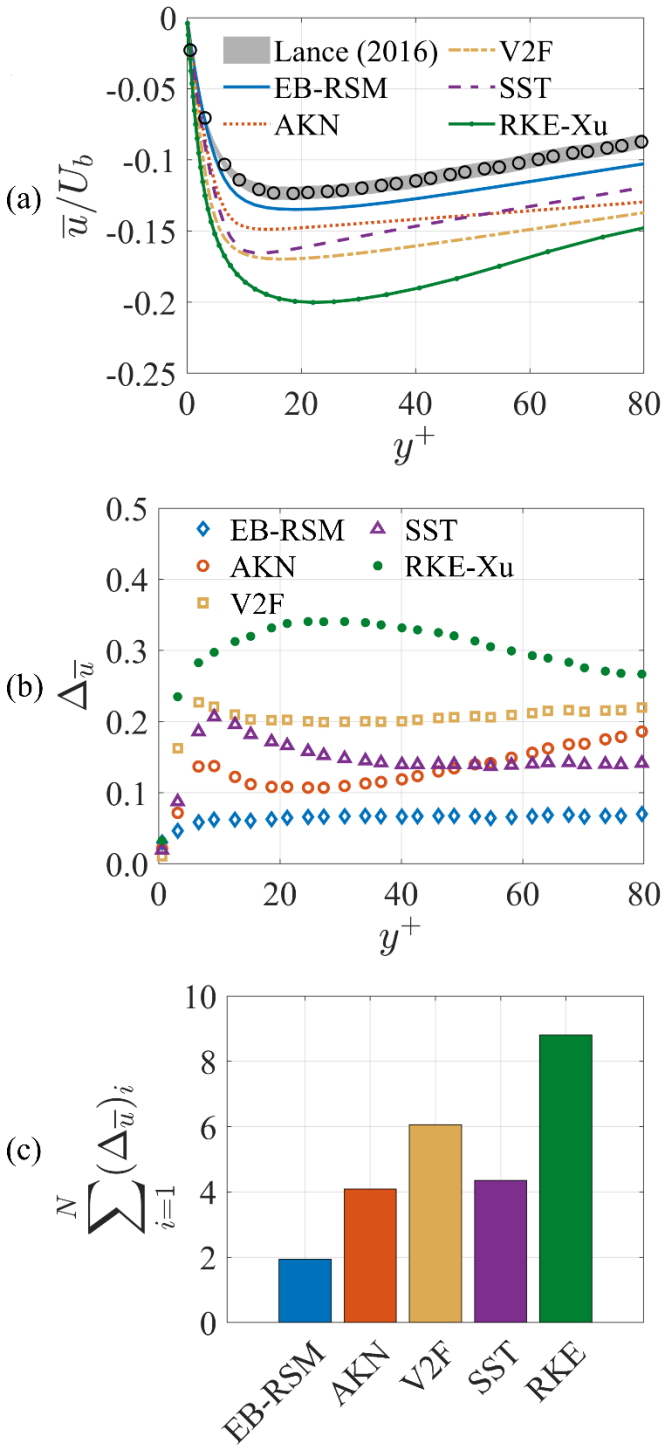

Figure 21: (a) Velocity, (b) results of the area metric at query points, and (c) summation of area metric along the line trace at location $\mathbf{x_2}\left(\mathbf{x}/\mathbf{L} \sim \mathbf{0.20}\right)$ at $\mathbf{t = 15.0\ s}$.

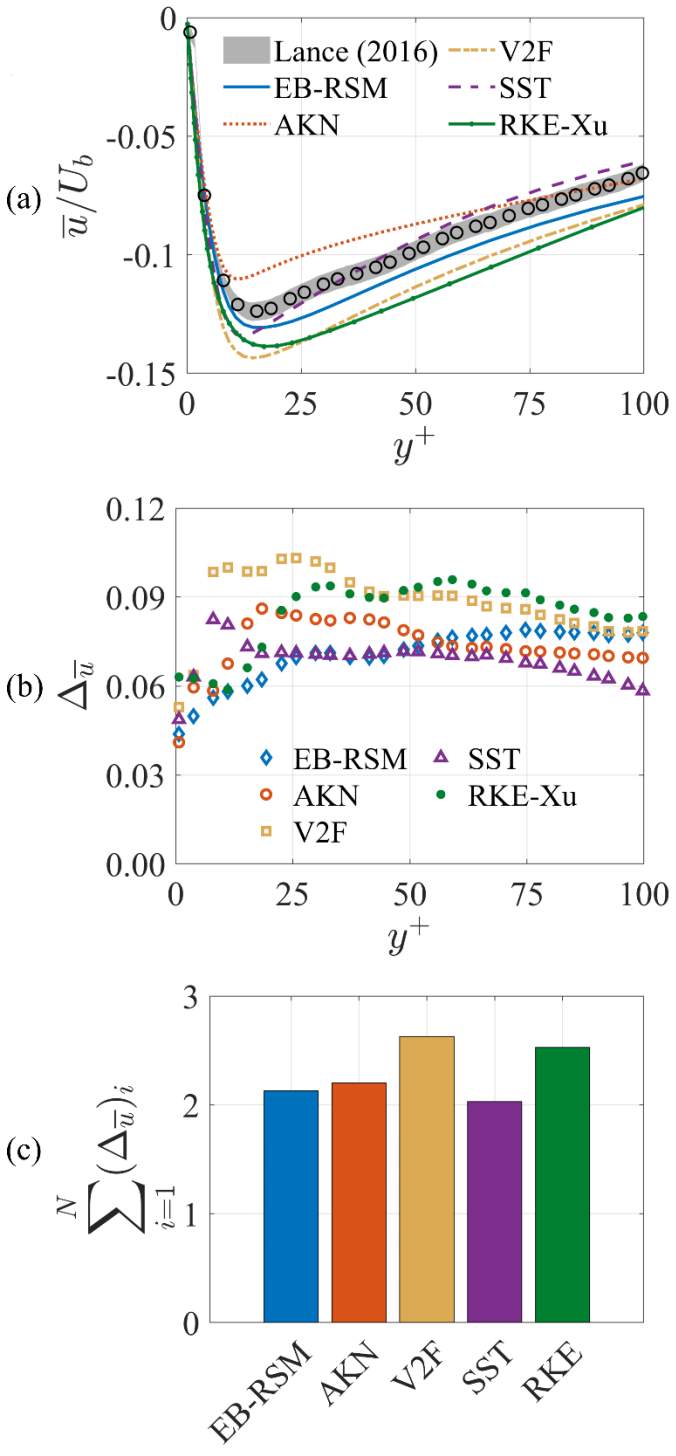

Figure 22: (a) Velocity, (b) results of the area metric at query points, and (c) summation of area metric along the line trace at location $\mathbf{x_3}\left(\mathbf{x}/\mathbf{L} \sim \mathbf{0.70}\right)$ at $\mathbf{t = 15.0\ s}$.

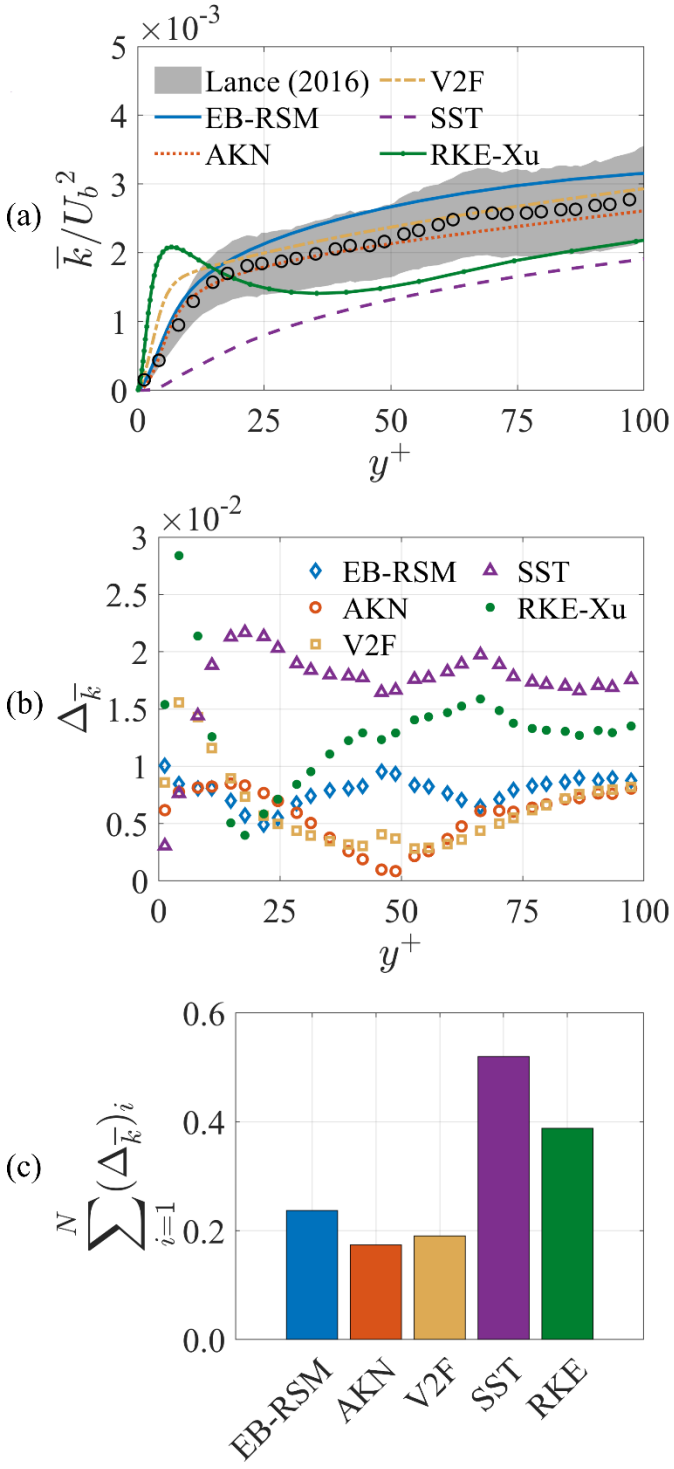

Figure 23: (a) Turbulent kinetic energy, (b) results of the area metric at query points, and (c) summation of area metric along the line trace at location $\mathbf{x_1}(\mathbf{x}/\mathbf{L} \sim \mathbf{0.08})$ at $\mathbf{t} = \mathbf{15.0\ s}$.

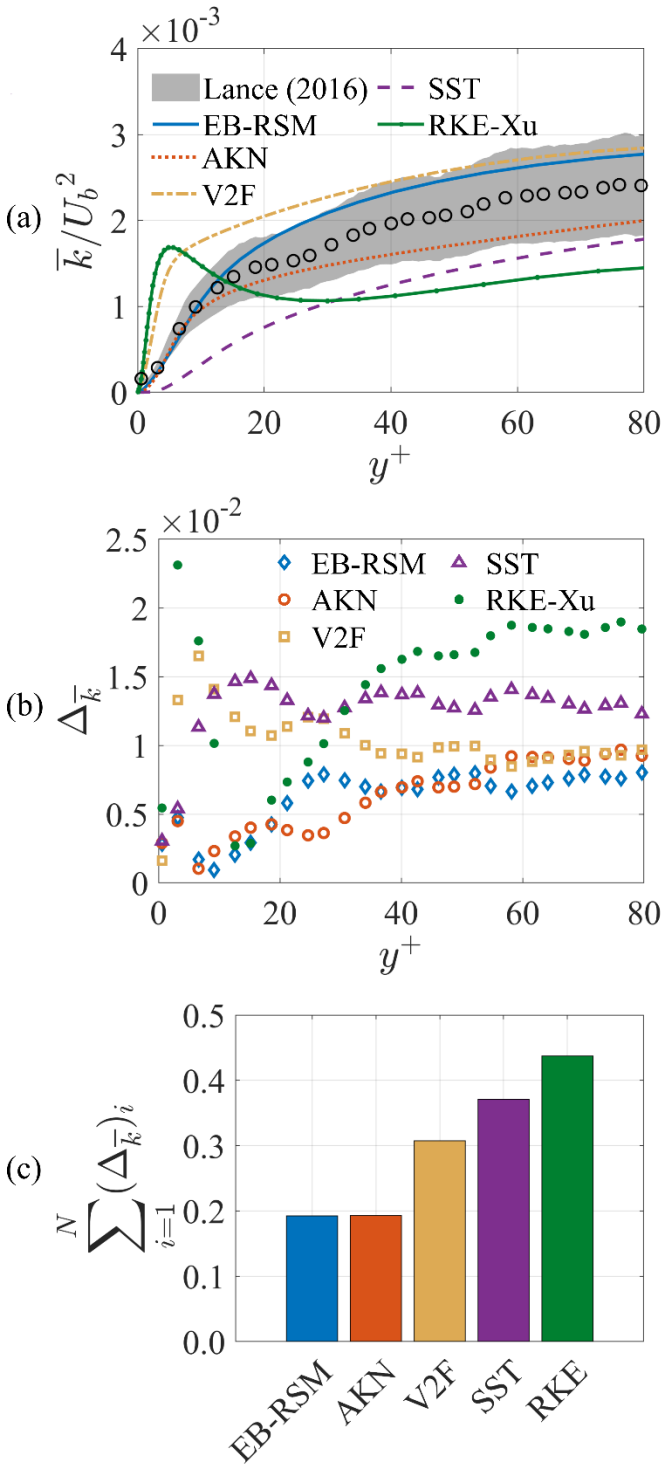

Figure 24: (a) Turbulent kinetic energy, (b) results of the area metric at query points, and (c) summation of area metric along the line trace at location $\mathbf{x_2}(\mathbf{x}/\mathbf{L} \sim \mathbf{0.20})$ at $\mathbf{t} = \mathbf{15.0\ s}$.

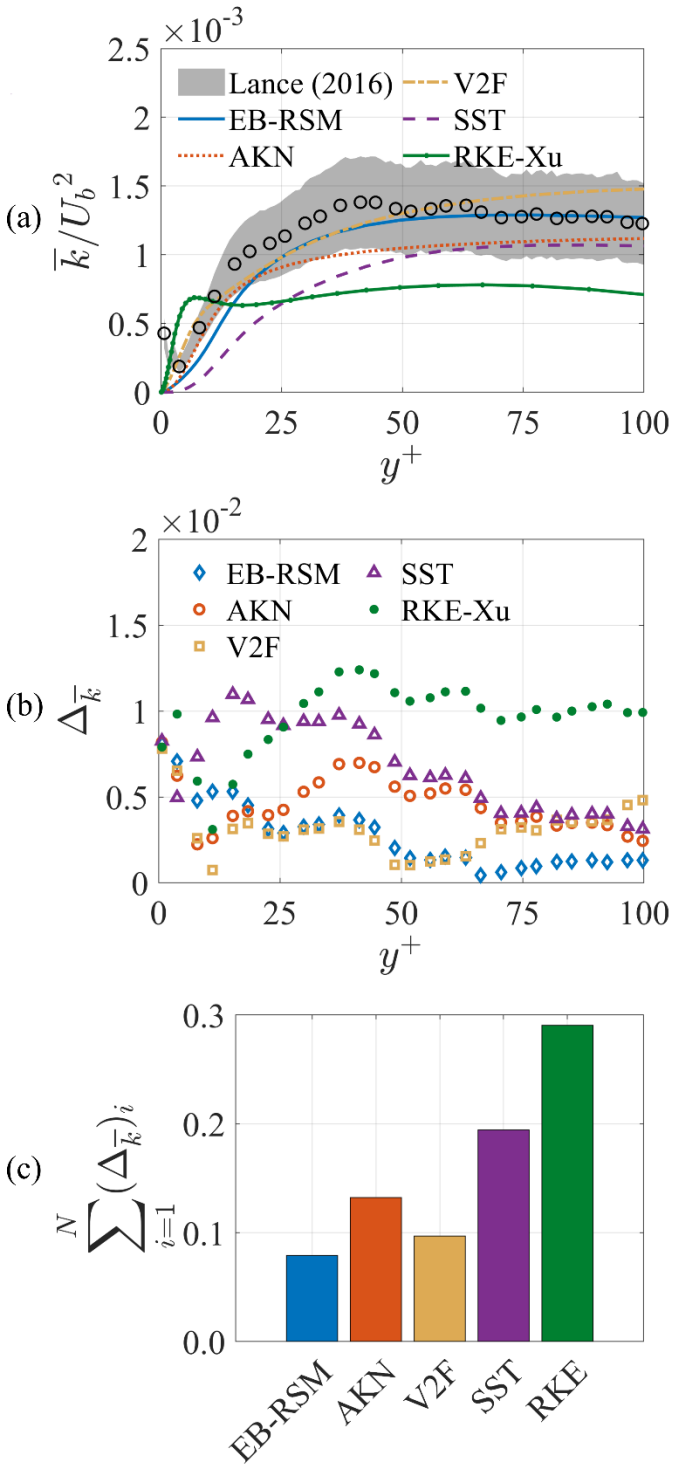

Figure 25: (a) Turbulent kinetic energy, (b) results of the area metric at query points, and (c) summation of area metric along the line trace at location $\mathbf{x_3}(\mathbf{x}/\mathbf{L} \sim \mathbf{0.70})$ at $\mathbf{t} = \mathbf{15.0\ s}$.

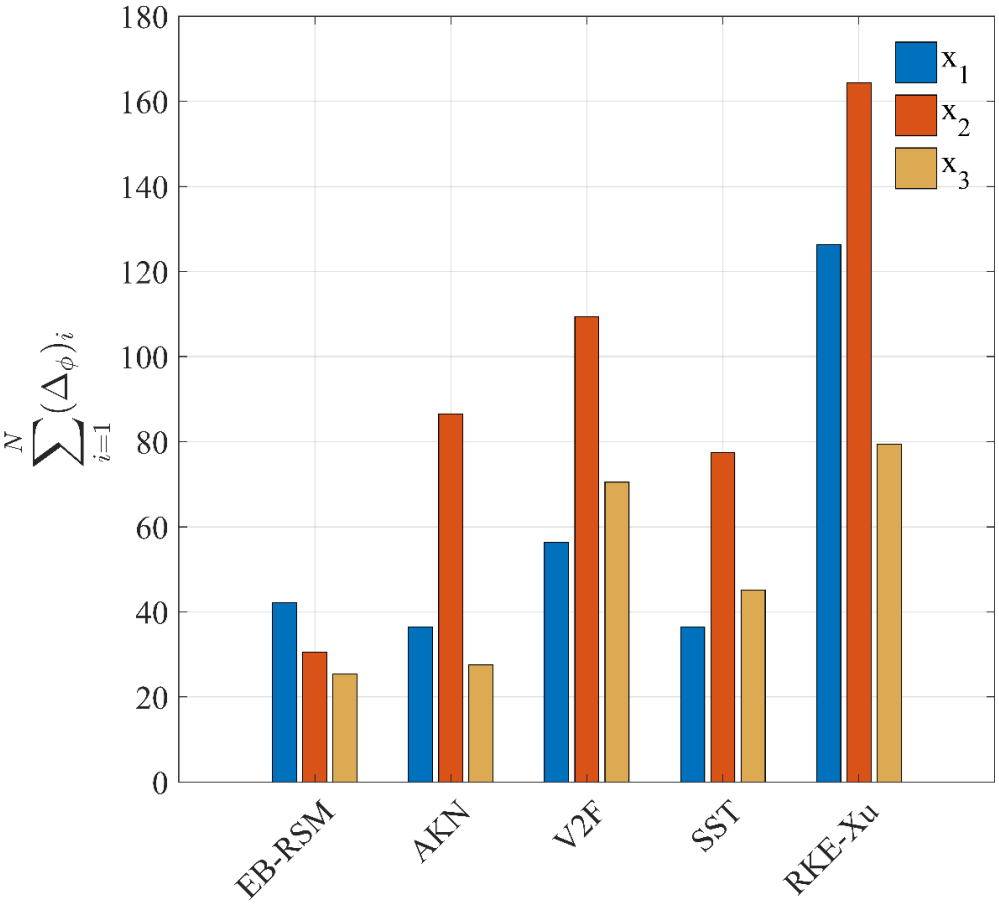

Figure 26: Results of the area metric for the skin friction coefficient for t = 12 – 18s.

CHAPTER III

COMPARISON AGAINST DIRECT NUMERICAL SIMULATION DATABASE

Background

The turbulence model assessment presented in Chapter II confirms the concerns raised in a previous study [4] that there is a significant amount of discrepancy in the prediction of system response quantities for buoyancy influenced flow regimes between different turbulence models. These findings are particularly alarming considering that the conditions for the most recent investigation are simplified, idealized environments in comparison to those experienced in standard industry practice. Considering these observations, the most logical route to providing well-informed modeling decisions for such conditions is to narrow the scope of the assessment to one model based on the results from most recent analyses. Immediately, the RKE-Xu model is removed from further consideration as it consistently provides poor predictions of system response quantities. In fact, the predictions are so poor in some cases, that the general applicability of this model is in question. This is not to suggest that the underlying RKE model is flawed, but rather the near-wall treatment (one-equation model of Xu [16]) lacks generality and accuracy even in the application of thermally induced buoyant flows, in which it is designed. The SST model is one of the most widely used turbulence models due to its seemingly vast range of applicability. However, the SST model is not known for its performance in buoyant flow regimes, as recognized in the present study, and its formulation already contains a large amount of empiricism, which makes it

difficult to extend its applicability. Elliptic relaxation models such as the V2F model are prevalent in literature for the application of buoyant flows [54], primarily due to their improved fidelity in capturing anisotropy caused by wall effects. However, in the current analysis, the results of the V2F model are rather sporadic and do not show any marked improvement in predictions compared to the other models. The two models which remain from the current analysis, EB-RSM and the AKN model, outperformed all other models in the calculation of the transient. This comes as no surprise for the EB-RSM, as it does not impose the eddy-viscosity hypothesis which has been known to fail in buoyant flow regimes [12, 13]. However, the EB-RSM is considerably more computationally expensive than the two-equation AKN model, and far more complex in its formulation. The AKN model performs quite well in comparison to the EB-RSM, and in many cases, provides a more accurate prediction of the system response quantities. However, the complex physics involved during the transient does not provide an ideal benchmark for model modification. In addition, the lack of reliable heat-transfer data from the transient case eliminates arguably the most important system response quantities in the analysis of a thermal-fluid system. Therefore, while the quantification of underlying numerical and input uncertainties in the aforementioned assessment greatly improves upon previous studies of similar flow physics [4], a detailed analysis of the model based on known solutions to similar flows is required to provide insight into modeling deficiencies. To address this, a DNS database consisting of two canonical mixed convection flow configurations is assembled to compare with the AKN model.

Direct Numerical Simulation (DNS) Database

The canonical flow configurations under consideration include a differentially heated parallel plate channel [10, 11] and a vertical pipe under a constant heat flux condition [9]. In both configurations, the thermophysical properties are defined assuming a constant Prandtl number of 0.71, while the buoyancy force is accounted for using the Boussinesq approximation.

$$Pr = \frac{\nu}{\alpha} \tag{32}$$

$$\rho \boldsymbol{g} = \rho_{ref} \beta \left(T - T_{ref}\right) \boldsymbol{g} \tag{33}$$

This simplification, presented in Equation (33), is based on the premise that the magnitude of the buoyancy force, caused by density variations in the flow, is adequately characterized by the differences in temperature within the fluid. While this assumption is convenient in terms of numerical simplicity and stability, it is only valid if the real variation in density is small, i.e., for very small changes in temperature ($\beta\left(T - T_{ref}\right) \ll 1$). To ensure a fully developed flow field, translational periodicity is assumed in the flow direction. A convenient way to characterize the extent of mixed convection is through the Richardson number, which represents a ratio of the buoyant to inertial forces using the definitions of the Reynolds and Grashof numbers.

$$Re = \frac{\rho U L}{\mu} \tag{34}$$

$$Gr_{Channel} = \frac{g\beta \Delta T L^3}{\nu^2} \tag{35}$$

$$Gr_{Pipe} = \frac{g\beta L^4 q_w}{\lambda \nu^2} \tag{36}$$

$$Ri = \frac{Gr}{Re^2} \tag{37}$$

The characteristic length scale, L, is defined as the half distance between the parallel plates for the channel configuration, while for the pipe, it is defined as the diameter. To account for the different modes of heating, the respective Grashof numbers for the channel and pipe are provided in Equations (35) and (36) where ΔT corresponds to the temperature difference between the two plates and q_w is the wall heat flux. The database for the channel consists of two cases: a forced convection ($\mathrm{Ri} = 0.0$) case and a buoyant case in which the Richardson number is approximately 0.048. The plates are differentially heated; therefore, the buoyant case contains data for buoyancy-aided (heated plate) and buoyancy-opposed (cooled plate) conditions. The schematic for this flow configuration is presented in Figure 27 where the bulk flow is in the positive x-direction. The bounds of the domain are defined in terms of the channel half distance (L), such that the extents of the x, y and z direction is 5πL, 2L and 2πL respectively.

Apart from the physical walls, (Hot Wall and Cold Wall in Figure 27) the x and z extents of the domain are translationally periodic. The bulk Reynolds number in the two cases is slightly different; $\mathrm{Re} = 4560$ and $\mathrm{Re} = 4494$ for the forced and buoyant cases, respectively.

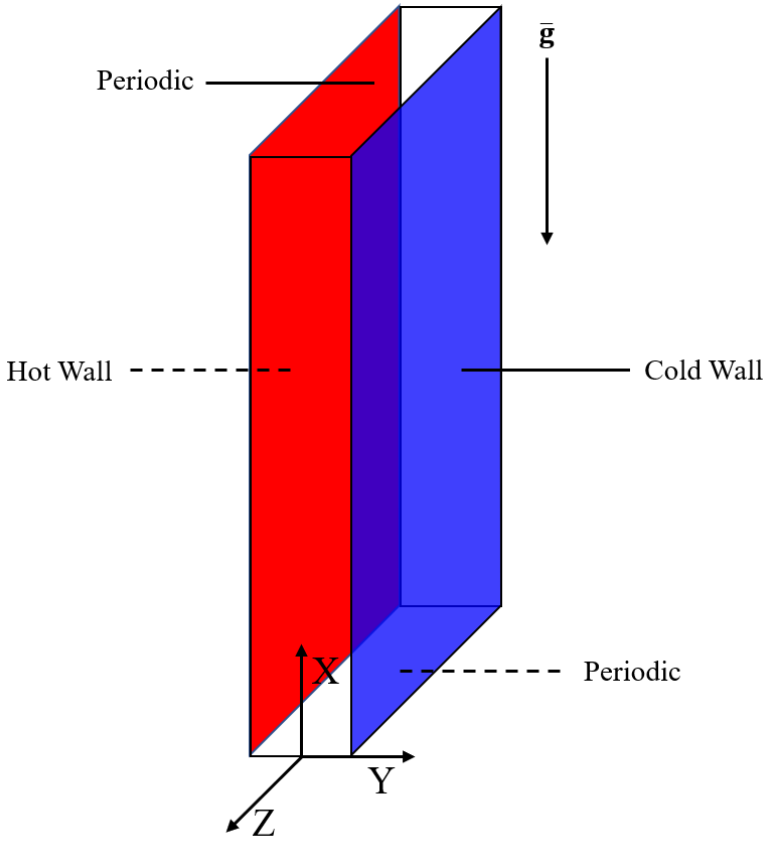

Figure 27: Computational domain for DNS of a differentially heated parallel plate channel.

The pipe database consists of four cases: one forced convection case and three buoyancy-aided and opposed cases of increasing Richardson number. In each of the pipe

cases, the Reynolds number is kept constant ($\mathrm{Re} = 5300$), while the Grashof number is increased by modifying the value of the wall heat flux condition. These three buoyant cases, detailed in Table 5, characterize the various stages of buoyancy influence on the mixed convection regime, namely, the early onset of laminarization (Case B), laminarization (Case C) and recovery (Case D). While this database contains data for both ascending (buoyancy-aided) and descending (buoyancy-opposed) mixed convection regimes, the effects of buoyancy on descending flow is marginal in comparison to ascending flow, where significant deterioration of heat transfer occurs.

Table 5: Details of DNS databases used in the current study.

Case	**Richardson Number**	
	Channel [10, 11]	**Pipe** [9]
Case A	0.00	0.00
Case B	0.048	0.063
Case C	-	0.087
Case D	-	0.241

Fundamentally, the flow domain for the pipe configuration is similar to that of the channel (refer to Figure 28), in that the flow is translationally periodic with a constant heating condition. However, in this case, there is only one set of periodic boundaries and the heating condition is a constant wall heat flux as opposed to the differentially heated constant temperature in the channel.

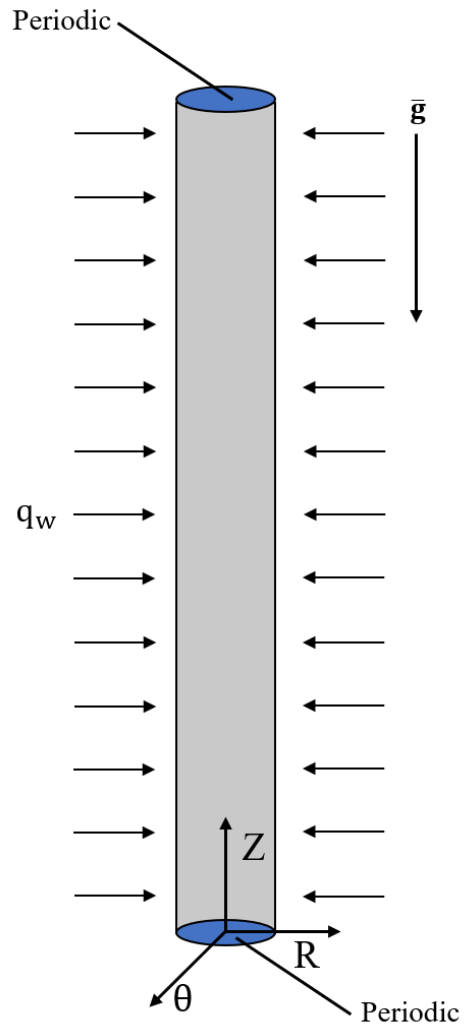

Figure 28: Computational domain for DNS of a heated vertical pipe with a constant heat flux.

To avoid excessive heating caused by a heat flux condition along an infinite domain, an additional sink term is used to ensure that the total energy input into the domain is based on one periodic module [55]. The extents of the pipe domain in the z direction are defined in terms of the pipe diameter, and they differ between the cases for buoyancy-aided and buoyancy-opposed regime (15L and 5L respectively). The longer domain in

the buoyancy-aided regime is required to ensure that production and destruction of the large-scale turbulent structures are captured. Several researchers have highlighted the difficulties RANS models experience in capturing the effects of buoyancy in ascending flow regimes [17-19], which are not present in the same range of Richardson numbers for descending flow. Therefore, the analysis of this database is focused primarily on the ascending mixed convection regime.

Computational Methodology

The schematics shown in Figure 27 and Figure 28 represent the three-dimensional computational domains used in the previously mentioned DNS investigations [9-11]. In the development of appropriate computational domains for the analysis of RANS models, several assumptions are imposed to reduce the computational expense. In the case of the differentially heated parallel plate channel, the extent of the z-direction is assumed to be infinite such that main contributions to the fully developed conditions come from the flow direction (x-direction) as well as the wall normal direction (y-direction) through both thermal and viscous constraints. In this way, the computational domain may be simplified by assuming the flow is properly characterized in two-dimensions (x and y). Schematically, this configuration is shown in Figure 29, with the flow developing in the positive x-direction and the gravitational force acting in the negative x-direction. Similar justifications are applied to the DNS domain for the pipe shown in Figure 30, however, an additional condition is needed to satisfy the geometric constraints imposed by the cylindrical pipe domain.

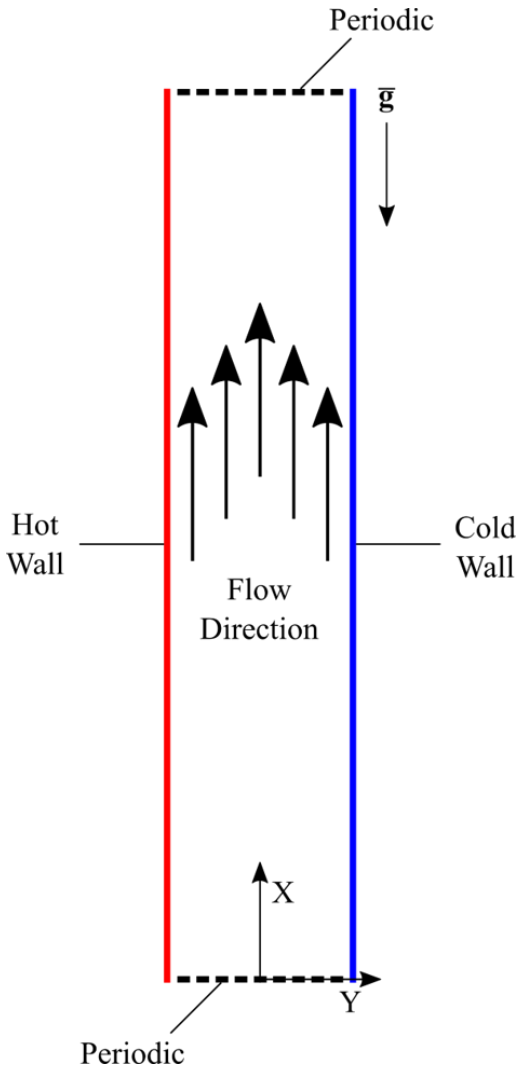

Figure 29: Two-dimensional RANS configuration for a differentially heated parallel plate channel.

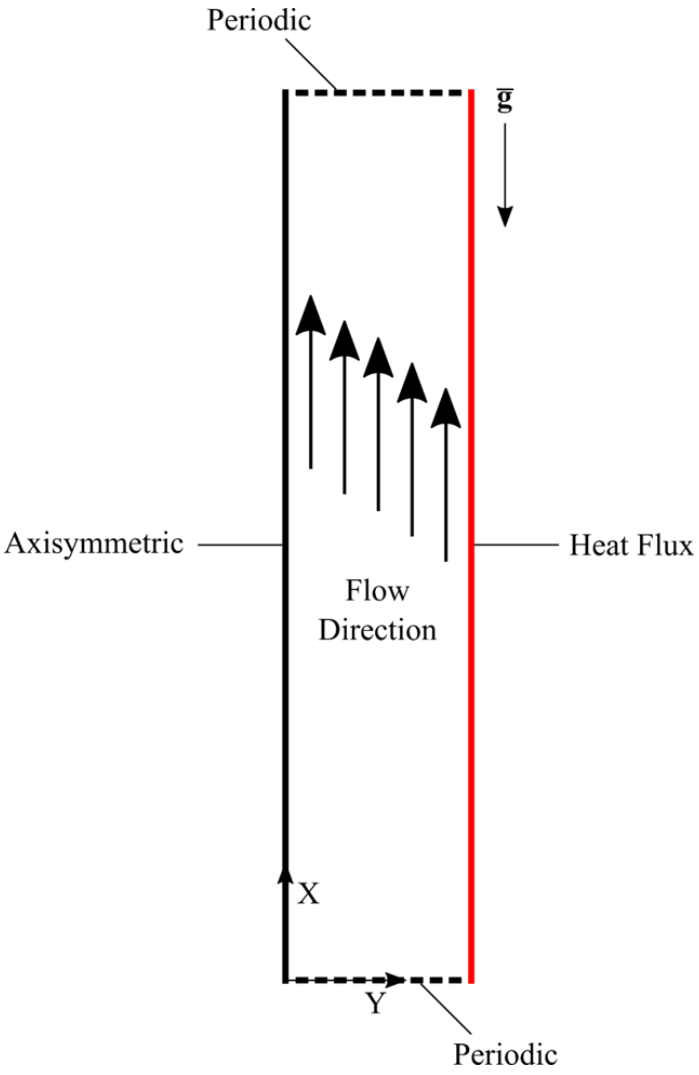

Figure 30: Two-dimensional axisymmetric RANS configuration for ascending pipe flow with a constant heat flux.

Pipe flow is inherently three-dimensional; hence a simple two-dimensional planar geometry will not consider the wall bounding effects enforced by the finite volume of the cylinder domain. To account for the wall effects in the azimuthal direction (Θ), an axisymmetric condition is applied at the center of the pipe which accounts for the full volume of the cylinder domain. To maintain consistency between the coordinate systems of the two simplified RANS domains, the streamwise (z-component) and radial (r-component) components in Figure 28 have been substituted by x (streamwise) and y (radial) in Figure 30. The computational grids for each configuration are meticulously constructed to provide adequate refinement in the near-wall region to resolve turbulent quantities through the viscous sublayer. The near-wall clustering of cells is based on a bi-geometric mesh law which distributes the cells based on initial and end node spacing [31]. Each case is computed on three separate computational grids (Table 6) of increasing cell count to ensure that the discretization uncertainty is appropriately reduced in accordance with the GCI method described Chapter II. The nearest node spacing is chosen to ensure that the maximum wall y^+ is less than unity for all cases. In addition, this nearest node spacing is constant for all three adaptations of the grid in each configuration, such that changes in the maximum wall y^+ between the three grids is insignificant. The medium density grid (Grid ID = 2 in Table 6) for each flow configuration, along with an enhanced representation of the respective near-wall refinement, is presented in Figure 31 and Figure 32. This heavy clustering is required to provide enough points to capture near-wall behavior, where large gradients in system

response quantities are expected. The gradual expansion of the cells smoothly transitions into the larger cells in the free stream, while retaining a moderate cell count.

Table 6: Details of the computational grids used for RANS assessment against DNS database.

Configuration	Grid ID	Cell Divisions		Domain Size (m)	
		X	**Y**	**X**	**Y**
Channel [10, 11]	1	100	60	10	2
	2	200	120		
	3	400	240		
Pipe [9]	1	90	30	0.5	0.05
	2	180	60		
	3	360	120		

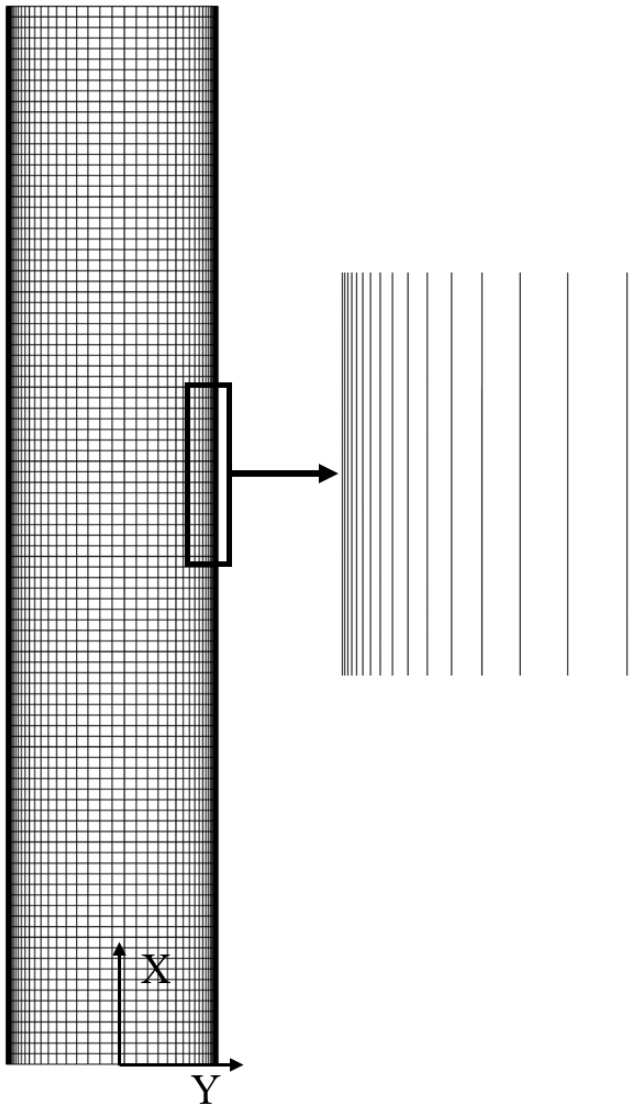

Figure 31: Medium density computational grid for two-dimensional, differentially heated parallel plates channel.

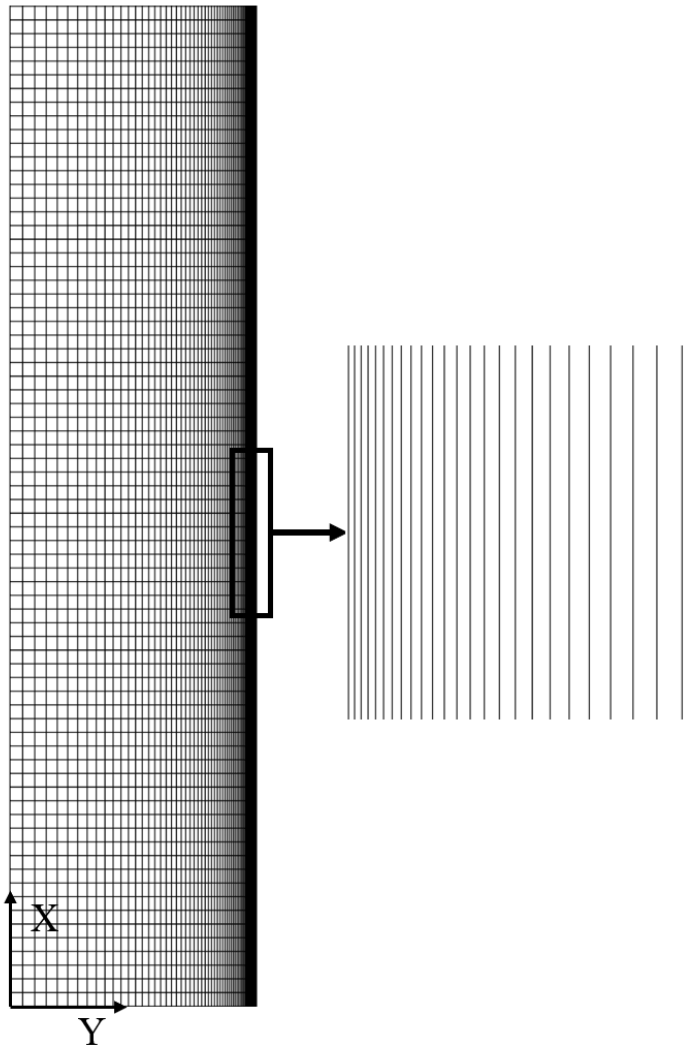

Figure 32: Medium density computational grid for two-dimensional axisymmetric pipe.

Governing Equations

Modeling the turbulent heat-transfer and flow characteristics of the mixed convection cases listed in Table 5 requires the solution to the steady form of the governing equations presented in Equations (38), (39) and (40):

$$\nabla \cdot (\rho \bar{\mathbf{v}}) = 0 \tag{38}$$

$$\nabla \cdot (\rho \bar{\mathbf{v}} \times \bar{\mathbf{v}}) = -\nabla \bar{p} + \nabla \cdot [\mathbf{T} + \mathbf{R}_{RANS}] + \rho \mathbf{g} \tag{39}$$

$$\nabla \cdot (\rho \bar{\mathbf{v}} \bar{E}) = -\nabla \cdot \bar{p} \bar{\mathbf{v}} + \nabla \cdot [(\lambda + \lambda_{RANS}) \nabla T] + \nabla \cdot (\mathbf{T} + \mathbf{R}_{RANS}) \bar{\mathbf{v}} \tag{40}$$

where the terms λ_{RANS} and $\mathbf{R}_{RANS}$ represent the turbulent contribution to mean heat-transfer and flow variables. In standard two-equation eddy-viscosity models such as the AKN model, the Reynolds Stress tensor, $\mathbf{R}_{RANS}$, is modeled using the relation presented in Equation (9). The analogous term in the energy equation, the turbulent heat flux, is modeled using the simple linear relation for the turbulent thermal conductivity, λ_{RANS}, in Equation (10). The AKN model in Star-CCM+ (v. 13.02.011-R8) retains many of the features of the standard two-equation k-ε model (Equations (11) and (12)), while adding damping functions to the turbulent viscosity (f_μ) and the destruction of turbulent dissipation rate (f_2) to resolve the turbulent quantities through the viscous sublayer.

$$\frac{\partial}{\partial t}(\rho k) + \nabla \cdot (\rho k \bar{\mathbf{v}}) = \nabla \cdot \left[\left(\mu + \frac{\mu_t}{\sigma_k}\right)\nabla k\right] + P_b + P_k - \rho\epsilon \tag{41}$$

$$\frac{\partial}{\partial t}(\rho \epsilon) + \nabla \cdot (\rho \epsilon \bar{\mathbf{v}}) = \nabla \cdot \left[\left(\mu + \frac{\mu_t}{\sigma_\epsilon}\right)\nabla \epsilon\right] + \frac{\epsilon}{k} C_{\epsilon 1}(P_k + C_{\epsilon 3} P_b) - f_2 C_{\epsilon 2} \rho \frac{\epsilon^2}{k} \tag{42}$$

$$\mu_t = \rho C_\mu f_\mu k \; max\left(\frac{k}{\epsilon}, C_t\sqrt{\frac{\mu}{\rho\epsilon}}\right) \tag{43}$$

$$f_\mu = \left[1 - \exp\left(-\frac{Re_\epsilon}{14}\right)\right]^2 \left\{1 + \frac{5}{Re_t^{3/4}} \exp\left[-\left(\frac{Re_t}{200}\right)^2\right]\right\} \tag{44}$$

$$f_2 = \left[1 - \exp\left(-\frac{Re_\epsilon}{3.1}\right)\right]^2 \left\{1 - 0.3 \exp\left[-\left(\frac{Re_t}{6.5}\right)^2\right]\right\} \tag{45}$$

This low-Reynolds number variation, presented in Equations (41), (42) and (43), results in the same number of closure constants and coefficients as the standard k-ε model presented in Table 7. The damping functions f_μ and f_2 in Equations (44) and (45) allow for the turbulent quantities to be resolved through the viscous sublayer. The use of local Reynolds numbers, Re_t and Re_ϵ, within the exponential functions provides a smooth transition of turbulent quantities from the near wall into free stream.

$$Re_t = \frac{\rho k^2}{\mu \epsilon} \tag{46}$$

$$Re_\epsilon = \frac{(\nu \epsilon)^{1/4} y}{\nu} \tag{47}$$

Table 7: Closure coefficients used in the AKN model in Star-CCM+ (v. 13.02.011-R8).

C_μ	$C_{\epsilon 1}$	$C_{\epsilon 2}$	$C_{\epsilon 3}$	C_t	σ_k	σ_ϵ
0.09	1.5	1.9	1.0	1.0	1.4	1.4

The production terms, P_k and P_b, represent the production of turbulence due to shear and buoyancy, respectively. An obvious avenue for improving the prediction of buoyant flows is to provide a more accurate representation of the production of turbulence due to the buoyancy force itself. Primarily, this production term is modeled using the simple gradient diffusion hypothesis (SGDH), which is based on the fundamental formulation of Fick's law of diffusion. In the case of an incompressible fluid, the expressions for these production terms are as follows.

$$P_k = \mu_t \bar{\mathbf{S}}^2 \tag{48}$$

$$P_{b_{\mathrm{SGDH}}} = \beta \frac{\mu_t}{Pr_t} (\nabla \bar{T} \cdot \mathbf{g}) \tag{49}$$

This formulation works well in many scenarios, however, it is clear to see that issues arise in the case that the temperature gradient in the direction of the gravitational force is zero. Understandably, there are many situations in which neglecting the turbulence production due to buoyancy is not acceptable, such as free or mixed convection for vertical plates with a Dirichlet type thermal boundary condition. Not only is the SGDH deficient in the above-mentioned cases, but due to its simplistic relation to the turbulent fields through the turbulent viscosity and turbulent Prandtl number, it often greatly under predicts the magnitude of turbulent production from buoyancy. To combat these deficiencies, it is often more practical to use the generalized gradient diffusion hypothesis (GGDH), which was first introduced by Daly and Harlow [56]. The general form was then expanded upon for use in RANS closure for the turbulent heat flux by Ince and Launder [57] to produce the following relation for the turbulent production due to the buoyancy.

$$P_{b_{GGDH}} = -C_\theta \beta \frac{k}{\epsilon} \vec{\mathbf{g}} (\overline{\mathbf{R}}_{RANS} \cdot \nabla T) \tag{50}$$

In this form, the deficiencies apparent in the SGDH are resolved by inclusion of the Reynolds stress tensor and gradient of temperature. In the case where the temperature gradient in the direction of the gravitational force is zero, the GGDH includes the cross-stress term to provide a more realistic, non-zero representation of the buoyant production of turbulence. The SGDH presented in Equation (49) is the default modeling procedure

in StarCCM+ (v. 13.02.011-R8) for this production term. To improve upon this standard model, explicit source terms based on Equation (50) are applied to the k and ϵ equations using built in functionality in the StarCCM+ (v. 13.02.011-R8) framework through custom field functions.

Computational Procedure

In each case, the target Reynolds number is enforced by applying a constant mass flow rate through the domain. The thermophysical properties presented in Table 8 are applied in each case to match the working fluid of the DNS database ($Pr = 0.71$). Similar to the DNS cases, the buoyancy force in Equation (39) is modeled using the Boussinesq assumption presented in Equation (33). To ensure that this assumption is not violated by large temperature differences, the thermal conditions imposed on the domain are specified as a ΔT = 1 K for the differentially heated parallel plates and $q_w = 1\,\frac{W}{m^2}$ for the heated pipe.

Table 8: Thermophysical properties used in RANS comparison to DNS database

Thermophysical Properties			
Density $(\rho)[\mathrm{kg \cdot m^{-3}}]$	Dynamic Viscosity $(\mu)[\mathrm{Pa \cdot s}]$	Thermal Conductivity $(\lambda)[\mathrm{W \cdot m^{-1} \cdot K}]$	Specific Heat $(\mathrm{C_p})[\mathrm{J \cdot kg^{-1} \cdot K^{-1}}]$
1.00	1.775E-5	0.025	1000.00

To match the required Grashof and subsequent Richardson number for each buoyant case listed in Table 5, the gravitational constant is increased accordingly.

Each simulation is performed using the commercial finite-volume software package StarCCM+ (v. 13.02.011-R8) with the settings presented in Table 9.

Table 9: Simulation settings for RANS comparison with DNS database.

Simulation Setting	**Selection**
Simulation Type	2D, Steady
Solver	Segregated
Material Properties	Constant
Pressure-Velocity Coupling	SIMPLE
Turbulence Closure	Reynolds Averaged Navier-Stokes
Momentum Discretization	Second-Order Upwind
Energy Discretization	Second-Order Upwind
Turbulence Discretization	Second-Order Upwind

A second-order upwind differencing scheme is applied to all convective terms in the governing equations on the collocated, structured grids outlined in Table 6. The pressure and velocity fields are coupled through the SIMPLE algorithm, in which the method of Rhie and Chow [58] is used to interpolate the mass flux at the cell faces. The governing equations are iteratively solved using the Algebraic Multigrid (AMG) method available in the segregated flow solver in StarCCM+ (v. 13.02.011-R8) until the normalized residuals for all governing equations have dropped below 1×10^{-10}. All buoyant cases are initialized with the steady-state solution corresponding to the forced convection case

(Case A, Ri = 0.0). The comparison of system response quantities presented herein are obtained at the streamwise center of the computational domains for both the RANS and DNS cases.

Results

The results for each buoyant case listed in Table 5 are plotted against the corresponding forced convection case (Case A) for all system response quantities to show the impact that the buoyancy force has on the subsequent flow variables. The system response quantities for both configurations are normalized with their respective bulk velocity, U_b, and plotted against the non-dimensional wall distance y^+. To keep consistency in the results, the y^+ is calculated using the wall shear-stress from the DNS data for all solutions.

$$u_\tau = \sqrt{\tau_w/\rho} \tag{51}$$

$$y^+ = \frac{\rho u_\tau y}{\mu} \tag{52}$$

The derived quantities (Nusselt number and skin-friction coefficient) are calculated differently for each configuration. In the case of the differentially heated parallel plate channel, these quantities are based on the normal distance between the wall (hot or cold) and the location of the maximum velocity in the domain. In this way, the expression for Nusselt number and skin-friction coefficient take the following forms:

$$Nu = \frac{2q_w d}{\lambda(\langle \bar{T} \rangle - T_w)} \tag{53}$$

$$C_f = \frac{\tau_w}{\frac{1}{2}\rho\langle \bar{u} \rangle} \tag{54}$$

where the quantity d is the normal distance from the wall to location of maximum velocity and the bracketed terms ($\langle \bar{T} \rangle$ and $\langle \bar{u} \rangle$) represent the bulk mean temperature and velocity over the distance d. In the forced convection case (Case A), the distance d is simply the half channel width; however, in the mixed convection case (Case B), the location of maximum velocity is skewed towards the buoyancy-aided side (heated wall). In the case of the heated vertical pipe configuration, the quantity $\langle \bar{u} \rangle$ is replaced with the bulk velocity, U_b, and the Nusselt number is calculated by computing the wall heat-transfer coefficient from the applied heat flux and wall surface temperature.

Figure 33 presents the results for the velocity in both the buoyancy-aided (a) and buoyancy-opposed (b) regimes for the differentially heated parallel plate channel. As expected, the velocity profiles are very well characterized in the forced convection regime (Case A). While slight underpredictions appear in the velocity for Case A between a $y^+ = 25 - 75$, the near-wall gradient of velocity is very accurately captured. In Case B, the AKN model also captures the effect of buoyancy on the velocity profile for both the buoyancy-aided and opposed regimes. Even with this very slight increase in buoyancy ($Ri = 0.0 - 0.047$), the velocity profile deviates from the parabolic profile of

Case A, resulting in an asymmetric profile with the maximum velocity biased towards the buoyancy-aided regime. The increase and decrease in magnitude of the velocity for the buoyancy-aided and opposed regimes is a symptom of the suppressing effect that buoyancy has on the production of turbulence in these respective regimes. This effect is observed most clearly in Figure 34, where the magnitude of the turbulent kinetic energy is reduced in the buoyancy-aided regime (a), while the opposite occurs in the opposed regime (b). The AKN model captures this effect quite well in the opposed regime, as the profile maintains congruence with the DNS results. However, in the case of the buoyancy-aided regime, the AKN model greatly underpredicts the turbulent kinetic energy, particularly very close to the wall. Interestingly, this underprediction of turbulent kinetic energy does not prove to be detrimental in the prediction of derived quantities such as Nusselt number and skin-friction coefficient. A comparison of these derived quantities from the DNS and AKN model is presented in Table 10, as well as the percent difference between the modeled and benchmark results.

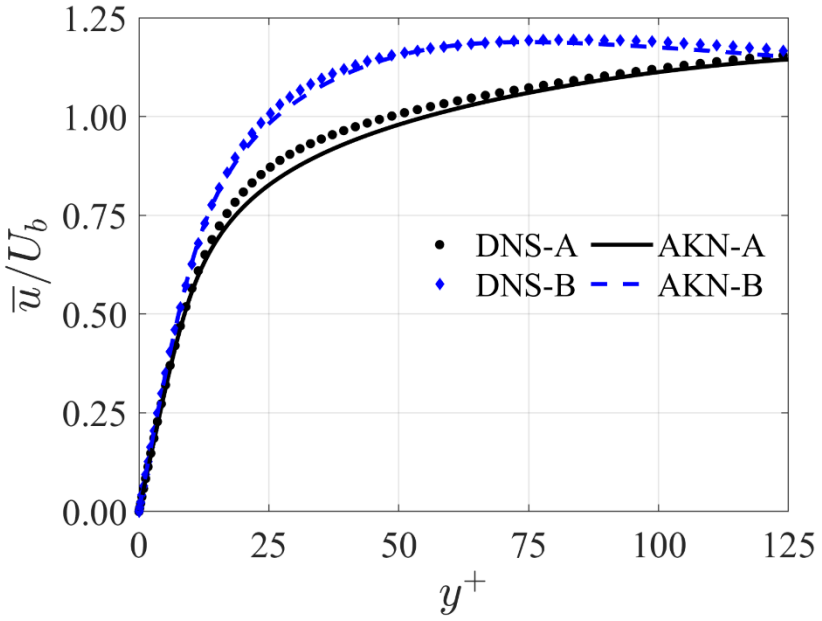

(a)

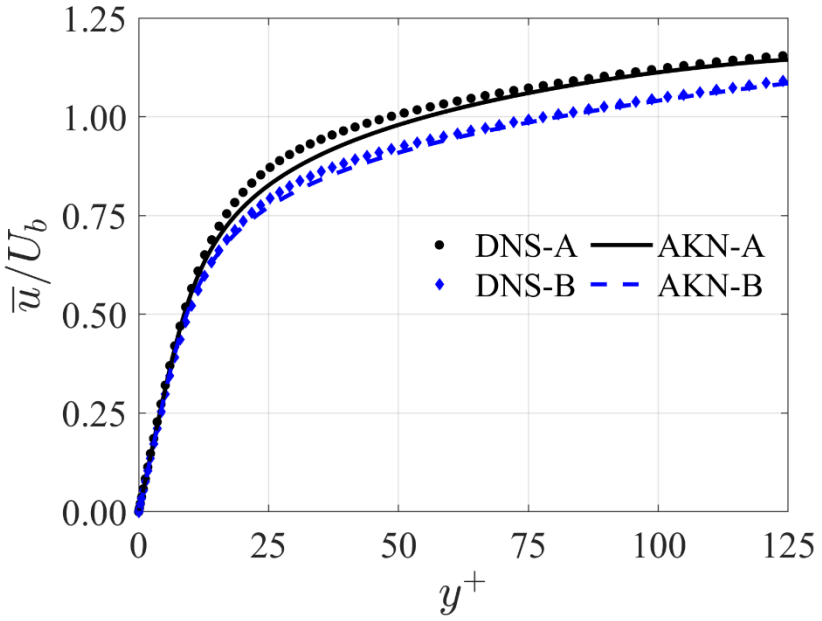

(b)

Figure 33: Line trace of velocity in the differentially heated parallel plate channel for buoyancy aided (a) and buoyancy opposed (b), between DNS (markers) [10, 11] and the AKN model (lines).

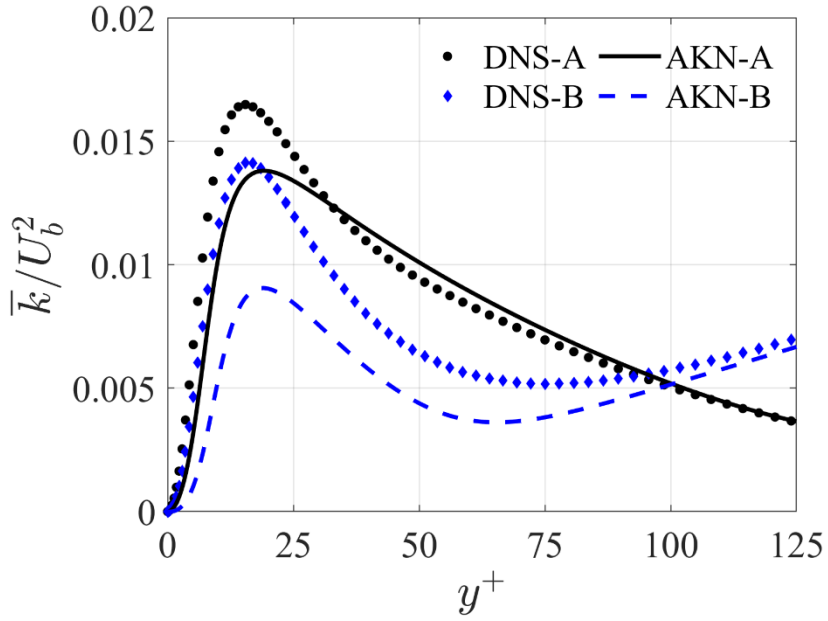

(a)

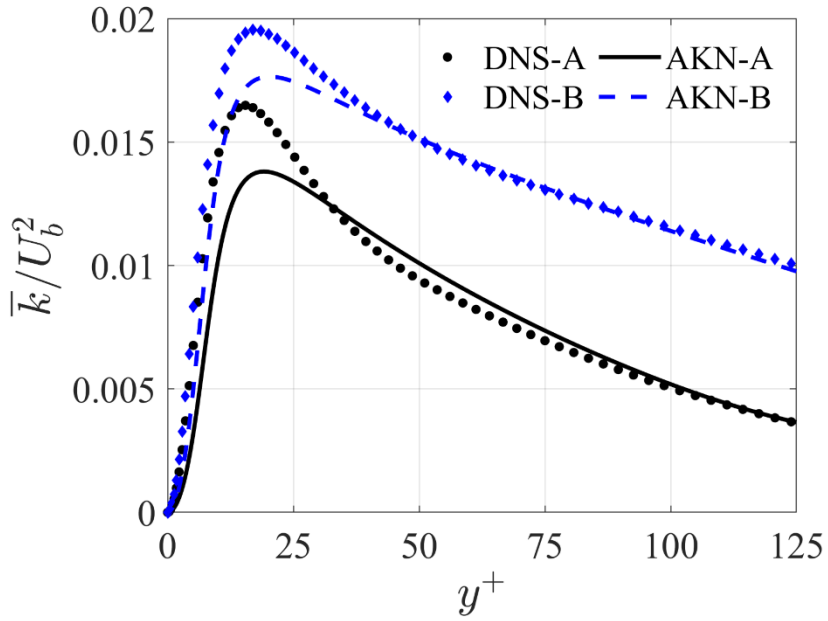

(b)

Figure 34: Line trace of turbulent kinetic energy in the differentially heated parallel plate channel for buoyancy aided (a) and buoyancy opposed (b), between DNS (markers) [10, 11] and the AKN model (lines).

Table 10: Comparative results for Nusselt number and skin-friction coefficient between the AKN model and DNS for a differentially heated parallel plate channel [10, 11]. Absolute percent difference is provided for reference.

Buoyant Case	**Model**	**Nu** **(**BA**,** BO**)**	**$C_f \times 10^{-3}$** **(**BA**,** BO**)**
Case A (Ri = 0.0)	DNS	13.4	8.66
	AKN	14.52 *(8.02%)*	8.67 *(0.12%)*
Case B (Ri = 0.047)	DNS	(7.42, 20.94)	(9.90, 7.90)
	AKN	(7.41, 23.55) *(0.13%,11.73%)*	(10.04, 7.90) *(1.40%, ~0%)*

The resolution of the near-wall velocity gradients in Figure 33 provides highly accurate values for the skin-friction coefficient in comparison to the DNS result. In Case A and the buoyancy-opposed regime in Case B, the percent difference is limited to less than 0.15%, while for the buoyancy-aided regime it is less than 2%. The results for the Nusselt number are also very close to the desired DNS values, with a maximum percent difference of 11.73% in the case of the buoyancy-opposed regime. The results of the skin-friction coefficient for both buoyancy-aided and opposed regimes show that the prediction of the velocity field is very accurate in both buoyant cases. In the prediction the turbulent kinetic energy, the magnitude of the buoyancy-opposed prediction is objectively closer to the DNS result than in the buoyancy-aided regime. In this case, one would expect that the proximity of these solutions should result in better predictions of all other derived quantities. Nonetheless, the accurate prediction of the derived system

response quantities all stem from how well the RANS model can reproduce the effect of turbulence on the mean flow. In the case of this simple two-equation eddy viscosity model, this boils down to the reliability of the turbulent viscosity prediction. The turbulent viscosity for the AKN model is calculated using the relation defined in Equation (43), while the same quantity for the DNS can be approximated using the mean shear stress and wall normal velocity gradient [59].

$$\mu_t \sim \frac{-\overline{u'v'}}{\partial \bar{u}/\partial y} \tag{55}$$

A comparison of the turbulent viscosity ratio for the DNS and AKN model is shown in Figure 35 for both the buoyancy-aided (a) and buoyancy-opposed (b) regimes in comparison to the forced convection results. In both the forced convection (Case A) and the mixed convection (Case B) cases, the AKN model provides an adequate representation of the turbulent viscosity, which translates into the excellent predictions of the previously mentioned system response quantities. By examining Equation (43), it becomes clear how the AKN model may be able to underpredict the turbulent kinetic energy, yet provide excellent predictions of the near-wall derived quantities. This underprediction must be balanced by either the near wall damping function for the AKN model (f_μ) or by the profile for the turbulent dissipation rate (ϵ).

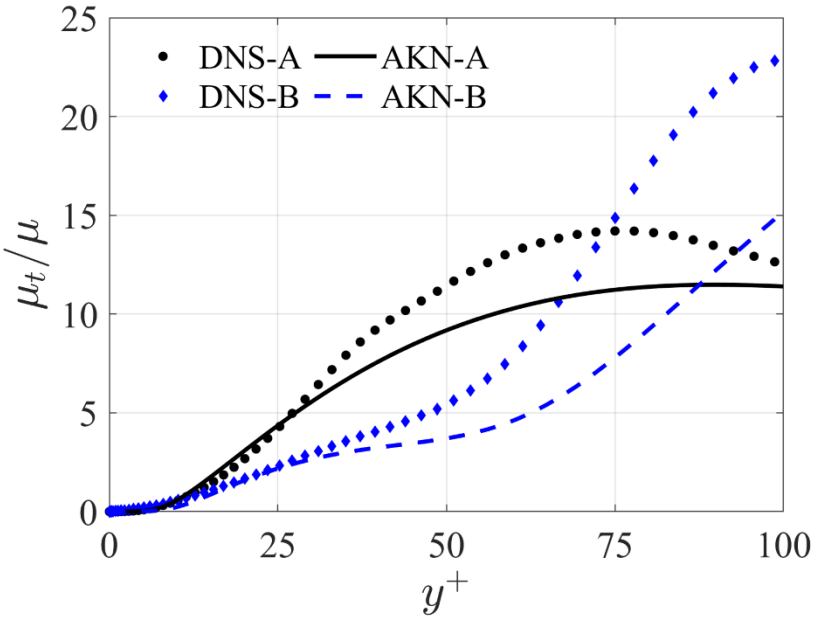

(a)

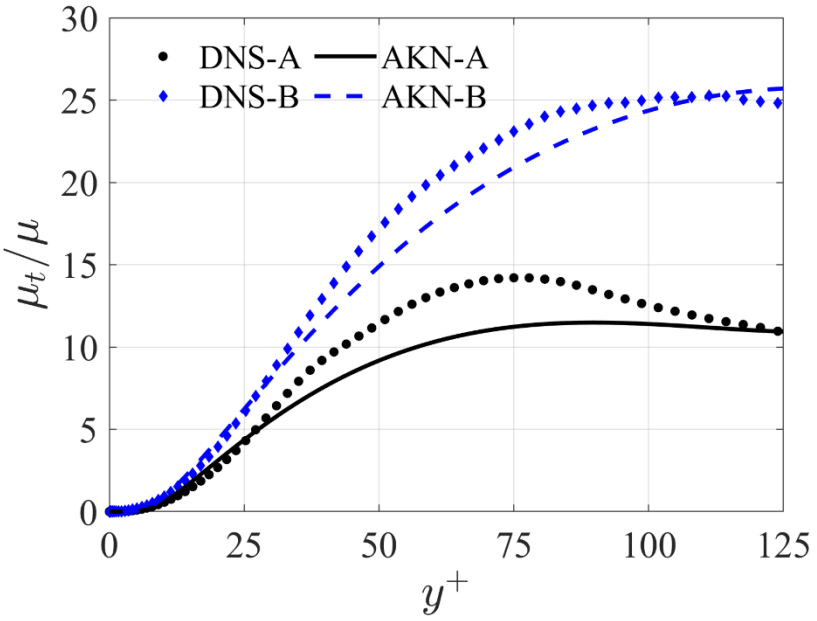

(b)

Figure 35: Line trace of the turbulent viscosity ratio in the differentially heated parallel plate channel for buoyancy aided (a) and buoyancy opposed (b), between DNS (markers) [10, 11] and the AKN model (lines).

The results for the heated vertical heated pipe configuration are presented in the same manner, with each buoyant case (Case B – D) plotted alongside the forced convection case (Case A). Cases B, C and D represent the several stages of buoyancy influence in upward flow regimes - the early onset of laminarization, laminarization and recovery, respectively. Like the channel configuration, Case B has a relatively modest increase in buoyancy force in comparison to Case A ($Ri = 0.00 - 0.063$). While this increase in buoyancy is similar to the change from Case A to Case B in the channel configuration, the distortion of the velocity caused by the reduction in turbulent kinetic energy, shown in Figure 36, is considerably less exaggerated. However, while the reduction in turbulent kinetic energy for the AKN model in Figure 36 (b) shows sensitivity on par with that of the DNS results, the velocity profile remains almost identical to Case A, as seen in the enhanced plot of Figure 36(a). As the buoyancy force increases from Case B to Case C ($Ri = 0.063 - 0.087$), the DNS results show that the flow undergoes a laminarization effect, shown most notably by the precipitous drop in turbulent kinetic energy in Figure 37(b). This reduction in turbulence causes a significant change in the velocity profile, which deviates from the parabolic shape in Case A to an M-shaped profile with the maximum velocity at around $y^+ = 50$. The AKN model is clearly insensitive to the local turbulent effects which cause this phenomenon, which is not surprising due to the highly non-linear physics of the buoyancy induced laminarization, i.e., small changes in buoyancy result in large changes in production and dissipation of turbulence.

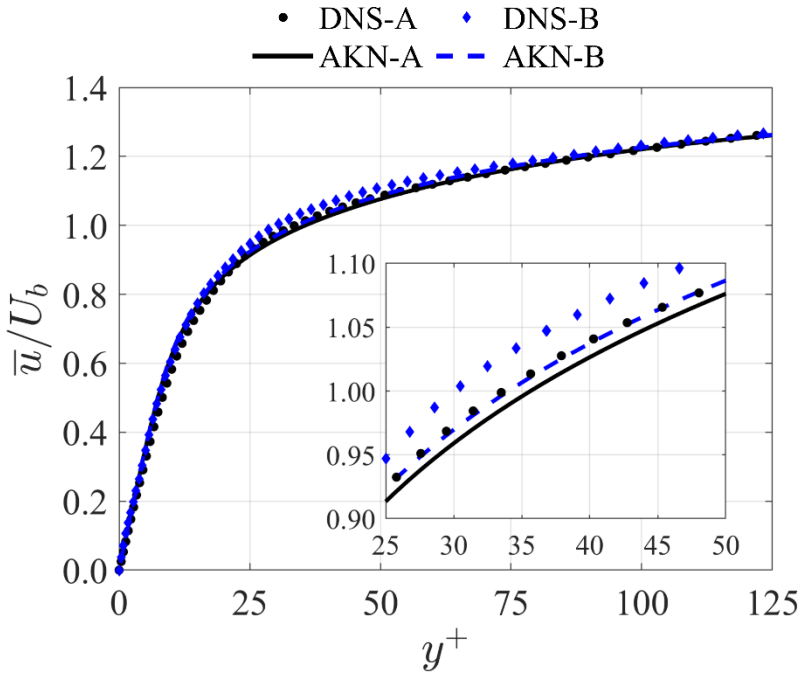

(a)

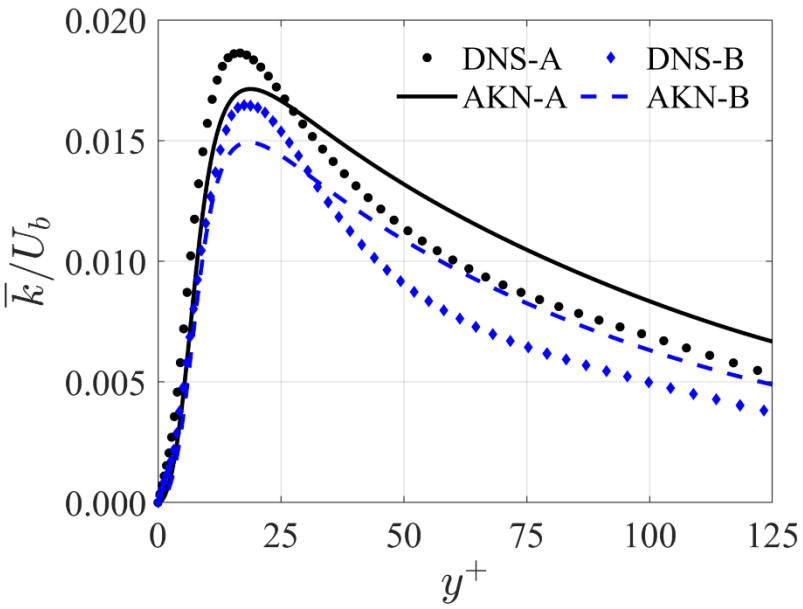

(b)

Figure 36: Comparison of line traces of velocity (a) and turbulent kinetic energy (b) for buoyancy aided flow for Case A and B within the heated vertical pipe configuration between DNS [9] (markers) and the AKN model (lines).

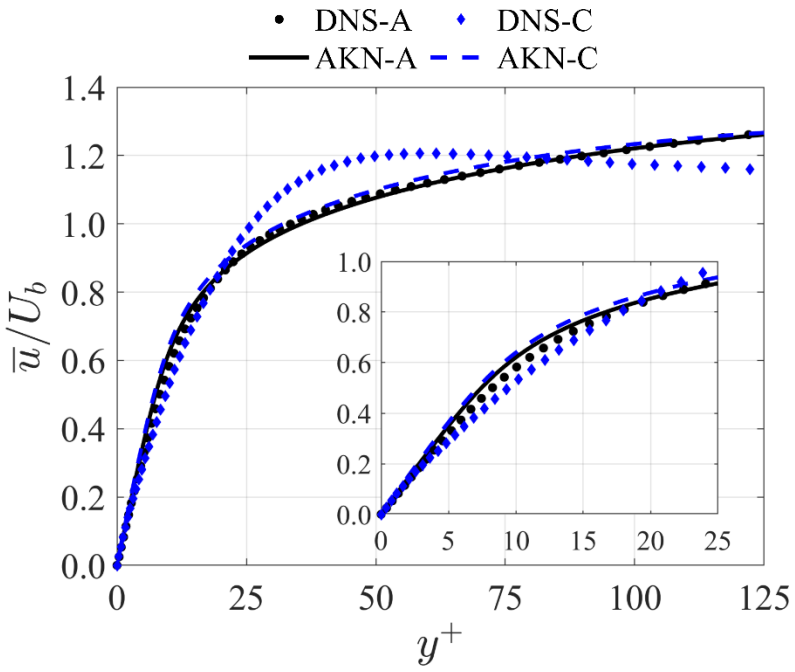

(a)

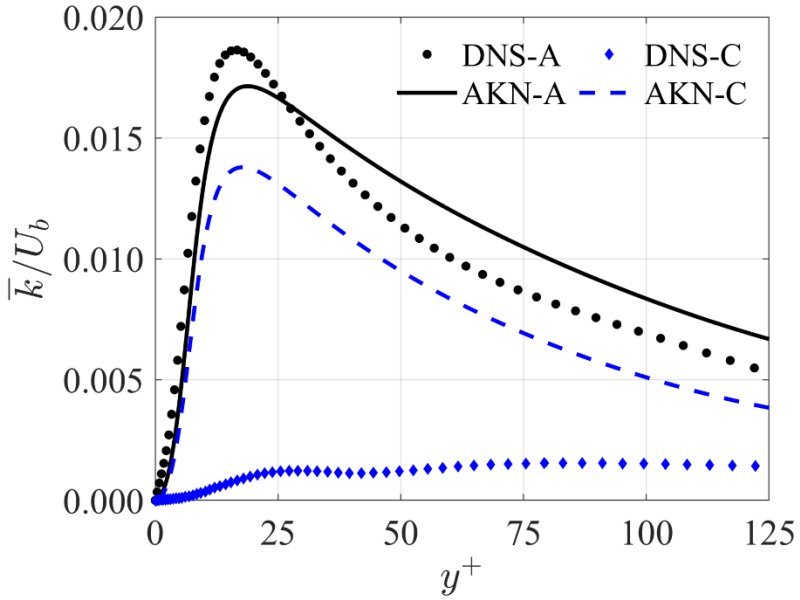

(b)

Figure 37: Comparison of line traces of velocity (a) and turbulent kinetic energy (b) for buoyancy aided flow for Case A and C within the heated vertical pipe configuration between DNS [9] (markers) and the AKN model (lines).

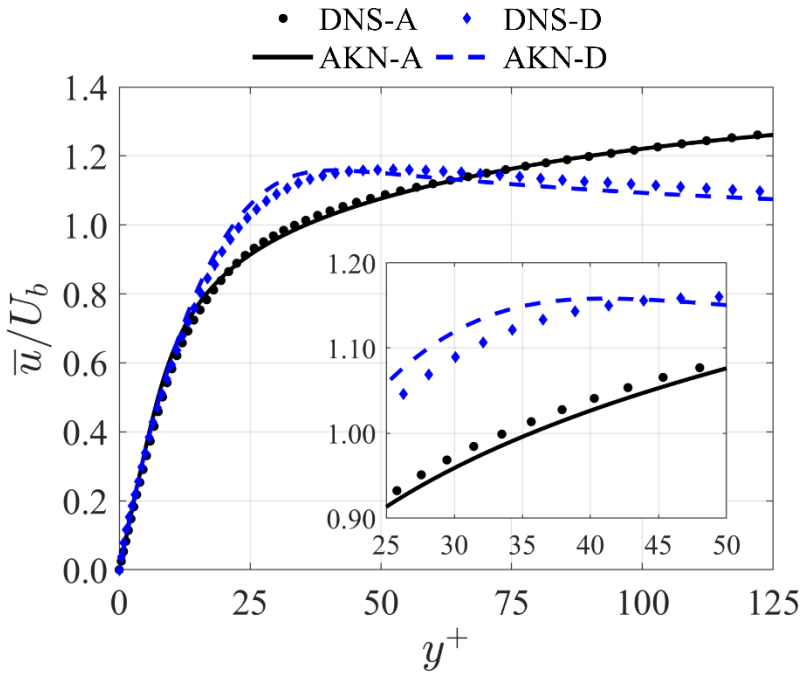

(a)

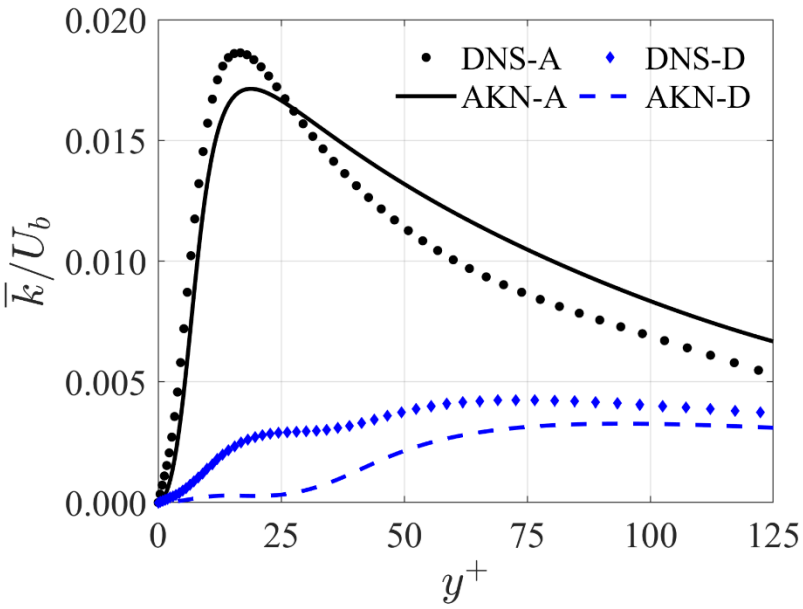

(b)

Figure 38: Comparison of line traces of velocity (a) and turbulent kinetic energy (b) for buoyancy aided flow for Case A and D within the heated vertical pipe configuration between DNS [9] (markers) and the AKN model (lines).

The inset in Figure 37(a) shows that the velocity prediction for the AKN model between Case A and Case C remains virtually unchanged, causing the near-wall gradient to be overpredicted. The inability of RANS based models like the AKN to capture the effects of buoyancy induced laminarization confirms the observations of several previous numerical studies [17-19]. However, the AKN model seems to adequately capture these effects for the early onset of laminarization (Case B), as well as in the recovery regime (Case D) shown in Figure 38. In Figure 38 (a), the M-shaped velocity profile is well characterized using the AKN model, which coincides with a considerably better prediction of the turbulent kinetic energy in Figure 38(b). While the near-wall turbulent kinetic energy is underpredicted in this case, similar observations from Case B in the channel configuration show that this does not necessarily result in poor predictions of derived quantities.

A comparison of the Nusselt number and skin-friction coefficient between the AKN model and the DNS for buoyancy-aided flow in a heated vertical pipe is presented in Table 11 for each case. Results for the forced convection (Case A), as well as the recovery regime (Case D), are in excellent agreement with the DNS values. However, in the intermediate Richardson number cases (Case B and Case C), the accuracy of the AKN model drops off significantly. While the predictions of Nusselt number and skin-friction coefficient for Case B are considerably closer to the DNS than those of Case C, the values of these quantities do not deviate much from Case A, hinting towards the model's insensitivity to effect of buoyancy.

Table 11: Comparative results for Nusselt number and skin-friction coefficient between the AKN model and DNS for a heated vertical pipe flow [9].

Buoyant Case	Model	Nu	$C_f \times 10^{-3}$
Case A (Ri = 0.0)	DNS	18.3	9.28
	AKN	19.25 *(5.06%)*	9.77 *(5.14%)*
Case B (Ri = 0.063)	DNS	15.68	8.75
	AKN	17.88 *(13.11%)*	9.70 *(10.30%)*
Case C (Ri = 0.087)	DNS	7.67	7.95
	AKN	17.12 *(76.24%)*	9.64 *(19.22%)*
Case D (Ri = 0.241)	DNS	10.45	1.10
	AKN	10.17 *(2.72%)*	1.15 *(4.44%)*

This is most notable for the skin-friction coefficient, which only changes by 1.33% between Cases A and C (from 9.77 to 9.64 × 10^{-3}), while the DNS changes by more than 15% over the same cases (from 9.28 to 7.95 × 10^{-3}). The overpredictions in these quantities for Case C are not surprising considering the poor results for velocity and turbulent kinetic energy shown in Figure 37. However, it is more telling to observe the drastic effect these predictions have on the resulting turbulent viscosity ratio in Figure 39, which serves as the interconnecting link between all dependent variables. The prediction of turbulent viscosity by the AKN model changes very little between cases A

and C, which provides reasoning for the subsequent lack of change in the system response quantities. On the other hand, the DNS results show that the steep drop of Nusselt number in Case C is directly correlated to an elongated region of reduced turbulent viscosity, i.e., laminarization. In this case, the DNS indicates this laminarization region extends out to a $y^+ \sim 45$ whereas the AKN model only exhibits a reduction in the turbulent viscosity in the free stream, with no changes in the near-wall behavior. The inability to predict any amount of laminarization until the recovery regime of Case D results in an overprediction of Nusselt number by 76.24% and 19.22% for the skin-friction coefficient. Differences of this magnitude for such idealized numerical conditions raises concerns as to the general applicability of the AKN model in capturing the intricate effects of thermally induced buoyant flows.

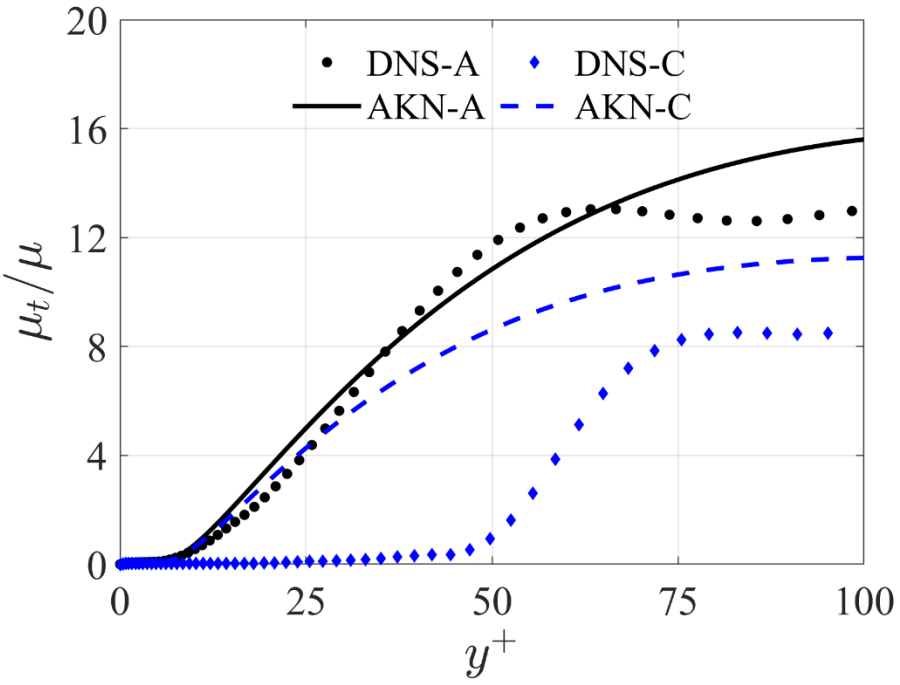

Figure 39: Turbulent viscosity ratio for buoyancy aided flow for Case A and C within the heated vertical pipe configuration between DNS [9] (markers) and the AKN model (lines).

CHAPTER IV

MODEL MODIFICATION AND VALIDATION

Background

The analysis presented in Chapter III explores the applicability of the standard AKN model within buoyancy influenced flow regimes through a comparison against well trusted DNS databases for mixed convection flows. These databases include buoyancy-aided and opposed-flow within a differentially heated parallel plate channel [10, 11], as well as buoyancy aided flow in a heated vertical pipe [9]. The combination of these two canonical flow configurations encompass a wide range of buoyancy-influenced flows, which are characterized by their respective Richardson number ($Ri = 0.0, 0.047, 0.063, 0.087, 0.241$). The results show that the AKN model provides excellent predictions of system response quantities in the case of forced convection ($Ri = 0.0$) and flows with a small influence of buoyancy ($Ri = 0.047$). However, as the influence of buoyancy is increased further ($Ri = 0.063 - 0.087$), the model predictions fail to capture the anticipated laminarization effects in the mean flow and turbulent system response quantities. The insensitivity to buoyancy for the AKN model becomes most apparent in the laminarization case (Case C in Table 11), where the poor prediction of the mean velocity and turbulent kinetic energy is emphasized by grossly overpredicted values of Nusselt number and skin-friction coefficient. The level of disparity between the DNS and AKN model predictions is attributed to the inability to properly characterize the influence of buoyancy on the turbulent kinetic energy, which is

controlled by the turbulent viscosity. In the case of forced convection and low buoyancy cases (Figure 35) this disparity is minimal, and the turbulent effects on the mean flow are captured well. However, at increased levels of buoyancy, the turbulent viscosity is completely misrepresented by the AKN model, resulting in failure to reproduce the intricate effects of buoyancy on the system response quantities. As the buoyancy force is increased past these intermediate Richardson numbers to the recovery regime ($Ri = 0.241$), the predictions of the AKN model agree well with those of the DNS results.

The gap between reliable predictions of the AKN model at different Richardson numbers raises concerns as to its suitability for buoyancy influenced flow regimes, which may have contributed to some of the difficulties the model experienced during the transient analysis in Chapter II. The deceleration period prior to the flow reversal ($t = 0.0 \sim 10.0\ s$) includes mixed convection flow regimes over a vast range of Richardson numbers, many of which lie above and below those covered in the current DNS databases. At any time during the transient, a discrepancy akin to those observed in Case C of the DNS comparative analysis could propagate into additional divergence from experimental measurements. These concerns, coupled with the inherent difficulties in modeling the transient phenomena in the RoBuT, would tend to produce further deviation from the benchmark system response quantities. While it is difficult to ascertain which of these complications is the main contributor to the poor predictions throughout the transient, the comparison with the DNS database shows that there is direct correlation between the prediction of the turbulent viscosity and the accuracy of the system response quantities of interest (Nusselt number and skin-friction coefficient).

In this case, the turbulent viscosity serves as the link which defines the complex interplay between momentum, energy, turbulence and buoyancy. However, the simplistic relation for the turbulent viscosity which is imposed by many RANS-based models is often far too general to be applicable for all possible flow conditions (Equation (43)), particularly those which exhibit a high level of anisotropy and non-linearity. To account for these conditions, many ad-hoc modifications are made to the standard models to extend their applicability. These modifications appear in a number of different ways, such as source terms in the governing equations [60, 61], production limiters [62], or even damping functions in the case of low-Reynolds number models [36, 37, 63-65]. Regardless of the formulation, these additions either directly or indirectly affect the turbulent viscosity, helping to extend the applicability of the underlying model while preserving its original generality and flexibility. Similar methods can be used to increase the suitability of the AKN model for buoyancy-influenced flow regimes. As a low-Reynolds number formulation, the AKN model already incorporates several modifications to the standard k-ϵ model via damping functions in the expression for turbulent viscosity (f_μ) and in the destruction of the turbulent dissipation rate (f_2), which are defined in Equations (44) and (45), respectively. In theory, these two damping functions could be optimized, either by reformulating one or both to be a function of buoyancy, or simply by manipulating the several constants within the functions to change the resulting shape. A recent investigation by Oler et al. [66] showed the feasibility of the latter using the low-Reynolds-number model of Yang and Shih [64]. In this study, the constants within the turbulent viscosity damping function are varied to

provide improved predictions for system response quantities within the differentially heated parallel plate channel of Kasagi and Nishimura [11]. While this method does not guarantee that the model is predictive outside of this range, it highlights the importance of the turbulent viscosity in providing accurate predictions of system response quantities. Rather than meticulously tune the constants within the damping functions for the AKN model for each buoyant case, efforts are focused on developing a buoyancy-dependent source term to account for the intricate effects of buoyancy observed in the DNS databases. Particular attention is focused on the heated vertical pipe database, as this database contains sequential cases of increasing Richardson number, while the channel database only contains one buoyant case at a low Richardson number. In addition, the comparison against the pipe database showed a progressive decline in predictive capacity of system response quantities at intermediate Richardson numbers, while the same comparison for the singular buoyant channel case yields excellent predictions. Without sufficient reference points at various Richardson numbers, it is impossible to confirm the same non-linear relationship between buoyancy and heat transfer for buoyancy-aided flow within a parallel plate channel. The difficulties experienced in the current analysis, as well as those noted in previous RANS model assessments [17-19] based on the DNS results of [9], provide further motivation for using this database as the primary benchmark for model development tailored for buoyancy-influenced flows.

Model Development

The current analysis against the DNS databases shows that the AKN model lacks sufficient sensitivity to capture the intricate effects of buoyancy on the mean flow characteristics. The most egregious example of this insensitivity is in the laminarization case (Case C), where a slight increase in Richardson number from Case B results in almost no change in the system response quantities. Comparing the profiles for turbulent kinetic energy between the DNS and the AKN model shows that the RANS based AKN model vastly over predicts this quantity, particularly in the buffer region near the wall ($5 < y^+ < 30$). This overprediction contributes to a complete misrepresentation of the turbulent viscosity, which negatively impacts the predictions of velocity and near-wall diffusion. To correct this behavior, an additional term must be added to the governing equations to effectively reduce the turbulent viscosity in the near-wall region. While it is difficult to determine the specific form of an additional term from this simple observation, a closer look at the modeled form of the turbulent viscosity and the desired DNS result provides some intuition. Ignoring all constants and limiters in the definition for the turbulent viscosity in Equation (43) leaves the following simplified relation.

$$\mu_t \sim f_\mu \frac{k^2}{\epsilon} \tag{56}$$

Using Equation (56) as a reference, the turbulent viscosity can effectively be reduced by modifying the damping function f_μ, or by creating a source or sink term in the governing

equations for the scalar turbulent kinetic energy and/or its rate of dissipation. In the original AKN model [36], particular care is taken in the development of the damping function to ensure that the asymptotic behavior of turbulence in the near-wall region is properly captured. Therefore, modifications to this function may negatively impact the generality of the model, especially for wall-bounded flows. As an alternative, a source term placed in the transport equation for the turbulent dissipation rate effectively works as a sink for turbulent kinetic energy, allowing for much of the original model to be preserved. The original formulation of the AKN model is very simple, with the only changes to the standard $k-\epsilon$ coming in the form of the aforementioned damping functions in Equations (44) and (45). This is in contrast to the formulation of many other low-Reynolds number models such as the Launder-Sharma [63], Yang-Shih [64], and Cotton-Kirwin [67] variants, which include additional source terms to the governing equations for turbulent kinetic energy and the turbulent dissipation rate. In these model formulations, the source term within the turbulent kinetic energy equation is included to simplify the boundary condition for turbulent quantities, allowing the effective turbulent dissipation rate to collapse to zero at the wall. However, there is no similar mathematical explanation for the inclusion of the source term within the turbulent dissipation rate equation. Instead, the inclusion of the term presented in Equation (57) is simply based on observational evidence of improved predictions of desired quantities.

$$S_\epsilon = C_\epsilon \nu \nu_t [(\nabla \cdot \nabla \bar{v})^2] \tag{57}$$

This term, which is based on near-wall velocity gradients, generates a local maxima in the turbulent dissipation rate within the buffer region and effectively dissipates in the free stream. The presence of this source term within the buffer region provides the model with increased sensitivity to local flow changes near the wall. The addition of a similar term in the AKN model could be used to heighten the model's sensitivity to buoyancy. However, as the aforementioned models require this term in order to obtain reasonable results, the AKN model does not require any additional terms for non-buoyant flow regimes. Hence, the additional term must not only be a function of buoyancy, but also must provide effective damping to not over sensitize the model. To provide this functionality, a turbulent Grashof number is derived to provide a buoyancy-dependent local flow variable. Like its global equivalent, this local relation is based on the ratio of buoyant to viscous forces ($\rho\mathbf{g}/\mu$) shown in Equation (58).

$$Gr_t = \frac{\rho \mathbf{g} k y}{\mu \epsilon} \tag{58}$$

Combining the turbulent Grashof number with local relations for the turbulent Reynolds number (used in the formulation of many low-Reynolds-number damping functions), results in the definition of a turbulent Richardson number Ri_t.

$$Re_d = \frac{\rho \sqrt{k} y}{\mu} \tag{59}$$

$$Ri_t = \frac{Gr_t}{Re_d^2} \tag{60}$$

The turbulent Richardson number presented in Equation (60) provides a convenient, local relation for the ratio of buoyant to inertial forces. In addition, the turbulent Richardson number follows basic heat transfer intuition, reaching its maximum value near the wall where the buoyancy force is highest and decreasing into the free stream where the inertial forces dominate. Combining the relationships for the turbulent Grashof and Richardson number with a similar term from Equation (57), the following source term for the turbulent dissipation rate transport expression is proposed for the AKN model.

$$S_\epsilon = \frac{Gr_t}{Gr_t + Re_t} \exp(-CRi_t) \nu \nu_t [|\nabla \bar{S}|^2] \tag{61}$$

The fraction of turbulent Grashof and Reynolds numbers follows a similar form to the flux Richardson number proposed by Rodi [68], which in this case, ensures that the new term only appears when the gravitational force is non-zero. Analogous to the term in Equation (57), the new source term is only present within the buffer region near the walls as demonstrated by Figure 40, which shows the magnitude of the source term calculated for Case B of the heated vertical pipe configuration.

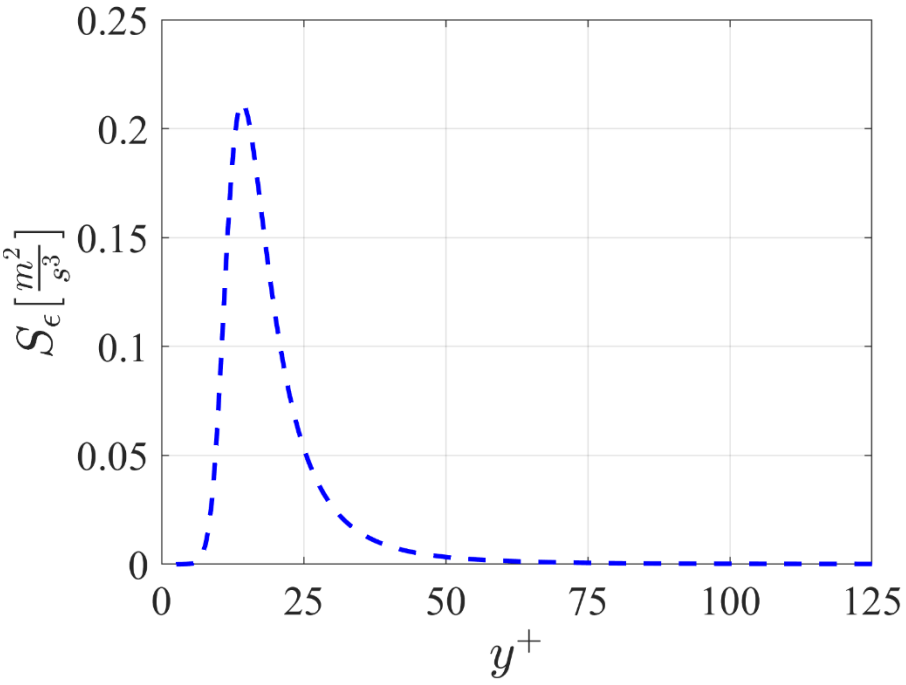

Figure 40: Resulting source term from Equation (61) for Case B in the heated vertical pipe configuration.

The exponential of the turbulent Richardson number acts as a damping function to ensure that the additional term does not over sensitize the AKN model to buoyancy. This damping is most crucial in the laminarization regime of Case C, where the calculation of gradients for an M-shaped velocity profile may be numerically unstable. A comparison of the general form of the source term in Equation (57) and the buoyancy-modified form in Equation (61) is presented in Figure 41.

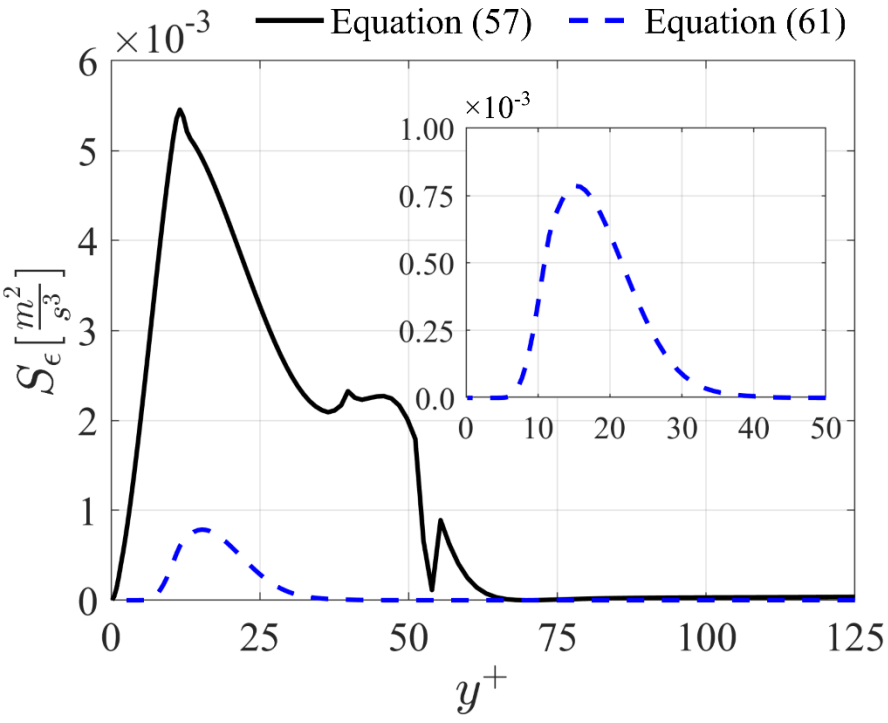

Figure 41: Comparison of the resulting source term with (Equation (61) - dotted line) and without (Equation (57) - solid line) the buoyancy modified damping function.

In the absence of the buoyant damping function, not only will the increased magnitude over sensitize the flow to buoyancy, but the resulting shape of the source from Equation (57) is highly non-linear, raising concerns about numerical stability. The inclusion of the damping function ensures that the new source term only appears within the near-wall buffer region ($5 < y^+ < 30$) , as well as providing moderation in the resulting magnitude. The magnitude of the damping function decreases with an increasing buoyancy force, allowing for the AKN model to retain its original form for very-high levels of buoyancy, in which the model showed excellent agreement with the DNS data (Case D). In addition, a tuning constant, C, is included and prescribed a value of 0.02. The value given to the closure constant is by no means optimized; however, it provides

adequate agreement for the given set of reference points (Case B - D). The new term defined in Equation (61) is applied as an explicit sourced term in the governing equation for the turbulent dissipation rate using the custom field function tools available in StarCCM+ (v. 13.02.011-R8). All computations are carried out using the same computational grids, settings and procedures presented in Chapter III.

Results and Validation

Case – B (Ri = 0.063)

The results for the velocity and turbulent kinetic energy between the original and modified AKN model for Case B is presented in Figure 42. Inevitably, the inclusion of the source term defined in Equation (61) has a direct impact on the turbulent flow field, particularly in the near-wall region in Figure 42(b). This drop in the turbulent kinetic energy results in a minor distortion of the velocity field, which can be observed by the decrease in the slope of the velocity profile within the buffer region in Figure 42(a). In the free stream, however, the reduction in turbulent kinetic energy results in improved prediction of the velocity field, highlighted by the inset in Figure 42(a). As observed in the assessment of the original AKN model against the DNS database, the under prediction of the turbulent kinetic energy does not necessarily limit the ability of the model to accurately predict crucial derived quantities such as Nusselt number and skin friction coefficient. Instead, it is the cumulative predictions of these quantities linked together through the underlying turbulent viscosity assumption which dictates the model's accuracy and general applicability to different flows.

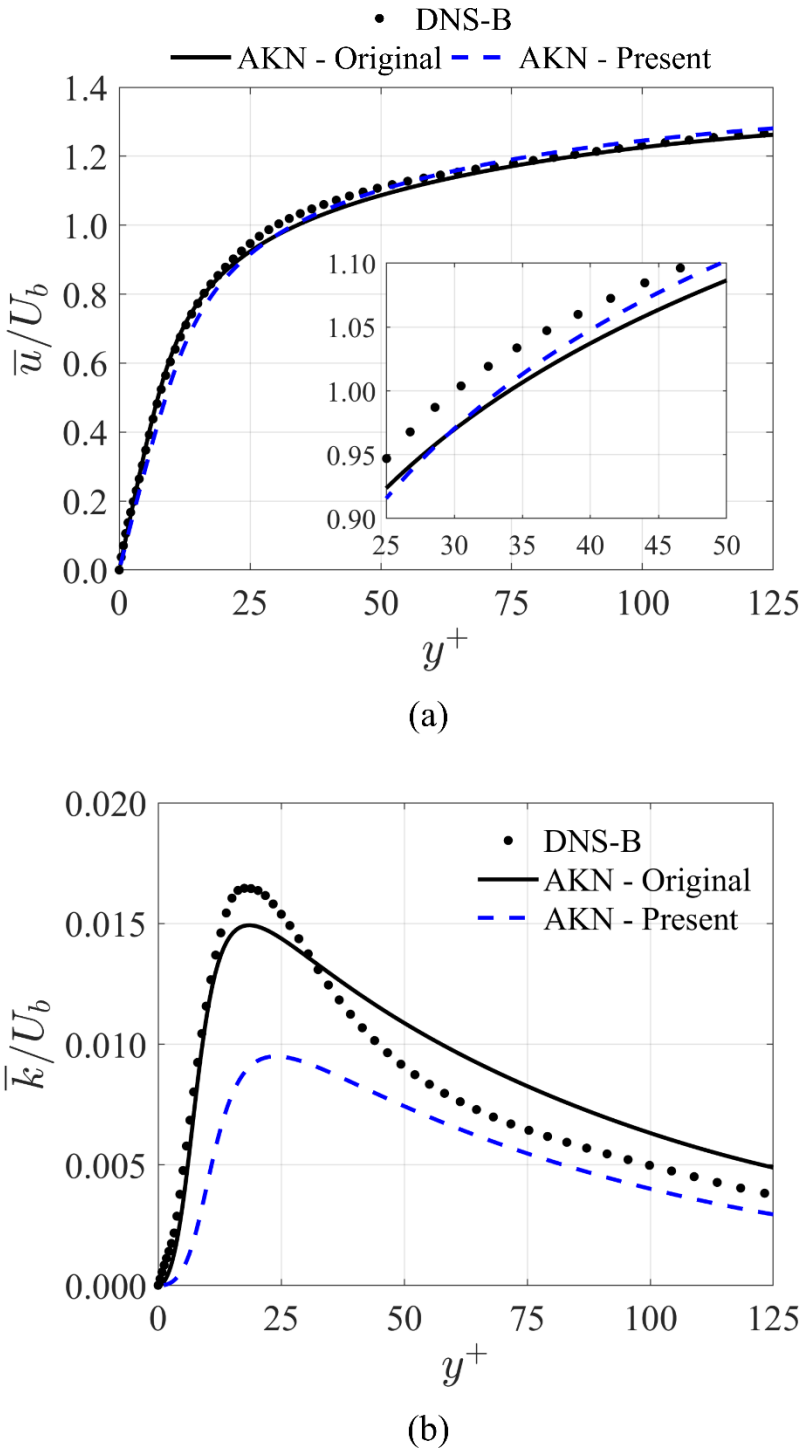

Figure 42: Comparison of line traces of velocity (a) and turbulent kinetic energy (b) for buoyancy aided flow for Case B within the heated vertical pipe configuration between DNS [9] (markers) and the original (solid lines) and modified (dashed lines) AKN models.

To provide a better understanding of the interplay of these variables and the effects on the resulting derived quantities, an extension of the area validation metric introduced in Chapter II is imposed on several system response quantities. Like the preceding analysis in Chapter II, every third data point along the line trace for the DNS data is used as a query point for comparison of mean values of turbulent kinetic energy and velocity. In addition to these two variables, the shear component of the Reynolds stress is included, as well as the derived Nusselt number and skin friction coefficient. To construct the simulation EDFs, the mean values and underlying uncertainties for each quantity of interest is interpolated to the spatial location defined by each query point. In this case, there is no uncertainty in the model input, hence the only source of uncertainty stems from the discretization of the governing equations (calculated through the GCI method). DNS data is widely accepted as exact solutions due to the resolution of all relevant time and length scales within the flow, as well as the use of high-order schemes in the discretization of the governing equations. The lack of uncertainty in the DNS solution causes the validation metric, defined in Equation (29), to collapse to a simple relative difference of mean quantities along with the numerical uncertainty quantified using the GCI method. In this way, the simulation EDF still has a similar shape to that shown in Figure 5, but the CDF for the DNS is defined by the Heaviside step function. To obtain one value for the validation metric for each spatially varying quantity, the metric is summed along the line trace, while the values for Nusselt number and skin friction are taken at the stream-wise center point of the heated wall. Comparative results for the area

validation metric between the original and modified AKN model are presented in Figure 43, with each chord extending from the origin representing the axis for a different system response quantity. Values closer to the origin represent lower dissimilarity between the DNS and AKN model. In the unlikely case where there would be no numerical uncertainty in the simulation, a validation metric of zero would represent the exact solution. The results of the validation metric for the velocity and turbulent kinetic energy in Figure 43 confirm the observations obtained through visual inspection of their respective line traces from Figure 42. Along the line trace, the cumulative relative difference between the AKN model and the DNS is lower for the original model relative to the modified version. In the case of the turbulent kinetic energy, this comes as no surprise as the peak in the buffer region is greatly underpredicted due to the increase in turbulent dissipation rate from the additional source term. However, upon visual inspection of the velocity profiles in Figure 42(a), the results from each model appear to be considerably closer to one another in both shape and magnitude than the results of the turbulent kinetic energy. This observation is contradicted by the results of the validation metric, highlighting the pitfalls of strictly using qualitative comparisons in reporting model accuracy and performance. The results in Figure 43 also stress the interconnectivity between different field variables, clearly demonstrating that the change in the turbulent kinetic energy has a direct and quantifiable effect on the velocity prediction.

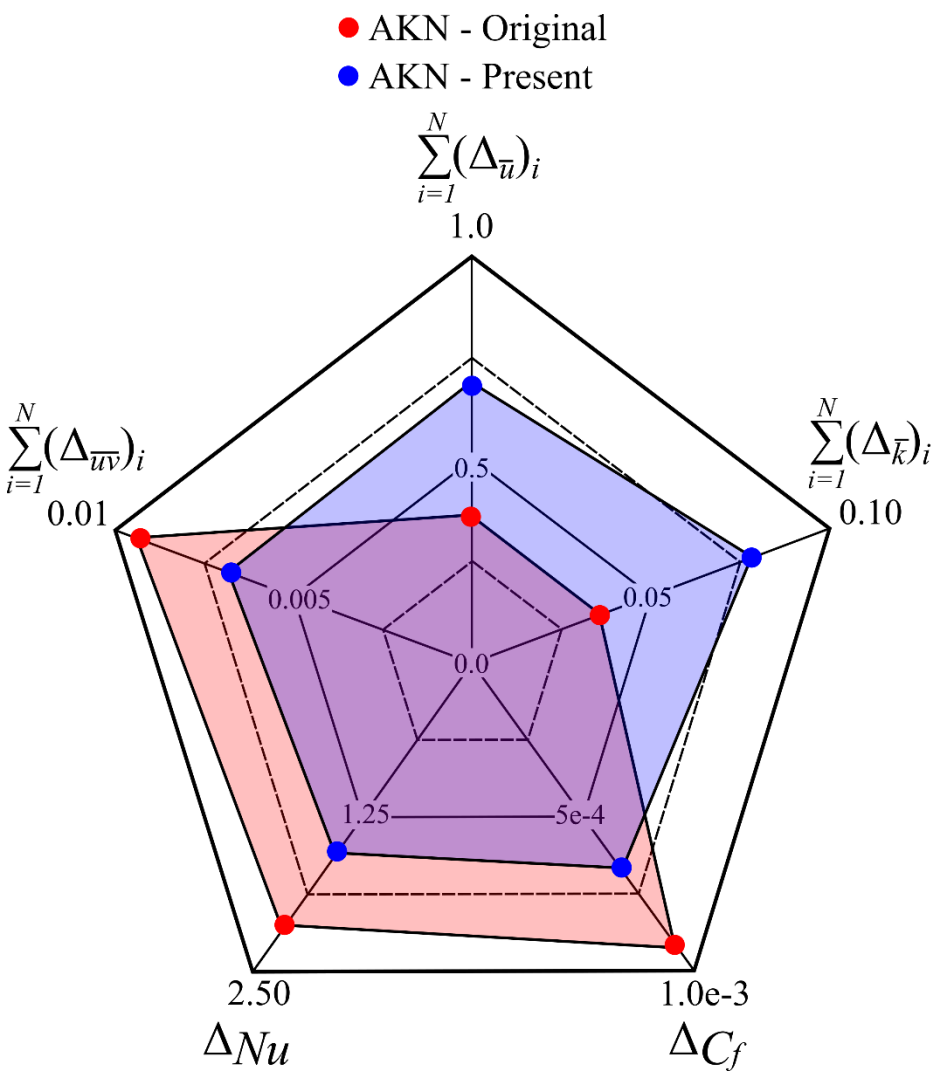

Figure 43: Results of the area validation metric for various system response quantities between the original and modified AKN model for Case B in the heated vertical pipe configuration.

While the inclusion of the source term in the modified AKN model results in increased dissimilarity with the DNS results for turbulent kinetic energy and velocity, the increase in turbulent dissipation rate in the near wall results in improved prediction of Nusselt number and skin friction coefficient. Similar to previous observations, this improvement

stems from a more accurate representation of the turbulent viscosity in the near-wall region through the buffer layer, as shown in Figure 44(b). The underprediction of the turbulent viscosity in the free stream is very similar to that observed in the buoyancy-aided case for the channel in Figure 35(a), which also results in well-predicted values of skin friction and Nusselt number. Considering these observations, obtaining an accurate representation of the turbulent viscosity within these high-gradient regions near the wall is pivotal in generating accurate predictions of the derived wall quantities like Nusselt number and skin friction coefficient. This improvement is also noticeable in the prediction of the Reynolds shear stress, presented qualitatively in Figure 44(a), as well as quantitatively using the cumulative area metric from Figure 43. The improvements in the modified AKN model observed in the area metric calculation for the Reynolds shear stress is a direct result of the more accurate representation of the turbulent viscosity within the near-wall region. Overall, the inclusion of the new source term in the AKN model does not negatively impact the applicability of the model within the flow regime for Case B. Although the area metric shows a marginal decline in the predictions of velocity and turbulent kinetic energy, the addition of the new source term corrects the near-wall turbulent viscosity, resulting in better predictions of Nusselt number, skin friction coefficient and the Reynolds shear stress.

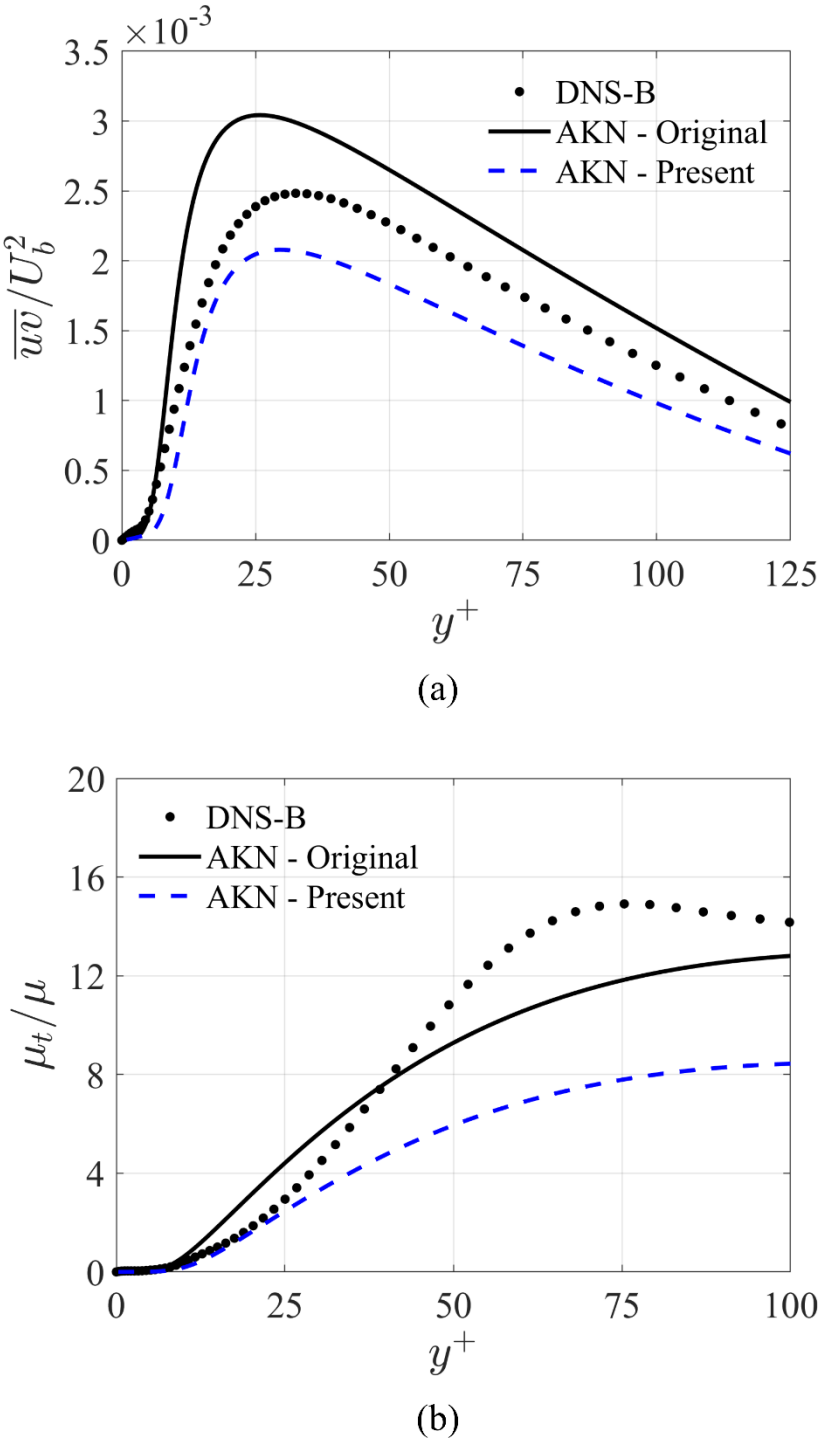

Figure 44: Comparison of line traces of Reynolds shear-stress (a) and turbulent viscosity ratio (b) for buoyancy aided flow for Case B within the heated vertical pipe configuration between DNS [9] (markers) and the original (solid lines) and modified (dashed lines) AKN models.

Case – C (Ri = 0.087)

As the buoyancy force increases from Case B to Case C, the impact of the additional source term on the mean flow quantities becomes considerably more significant. The resulting velocity and turbulent kinetic energy profile for both models is presented in Figure 45. While the original model shows almost no sensitivity to the increase in buoyancy, the buoyancy modified version shows excellent agreement with the DNS data. Figure 45(b) shows that the inclusion of the additional source term effectively reduces the turbulent kinetic energy to levels on-par with the laminarization effect observed in the DNS dataset. As a result, the velocity prediction in Figure 45(a) is significantly improved, particularly with respect to the near-wall gradients ($0 < y^+ < 25$) shown in the inset. As expected, these observations are confirmed in the results from the area validation metric in Figure 46. Most notably, the modified model shows vast improvement in the prediction of the derived quantities of Nusselt number and skin friction coefficient relative to the original model. The recovery in these predictions, presented in Table 12, stems from the inclusion of the source term which rectifies the discrepancies in the turbulent viscosity. From Figure 47(b), it is clear that the modified AKN model accurately predicts the area of laminarization (characterized by an effective turbulent viscosity of zero up to a $y^+ \sim 45$).

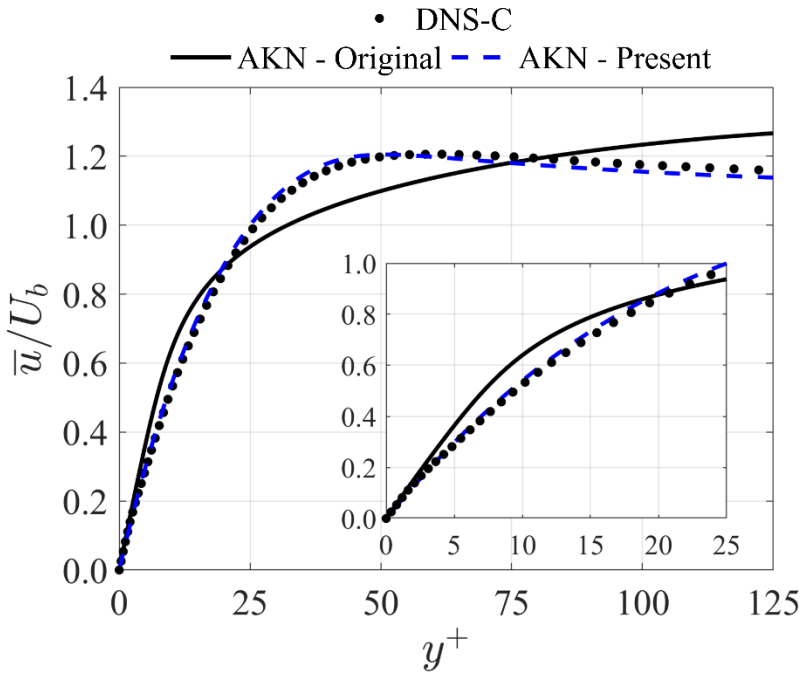

(a)

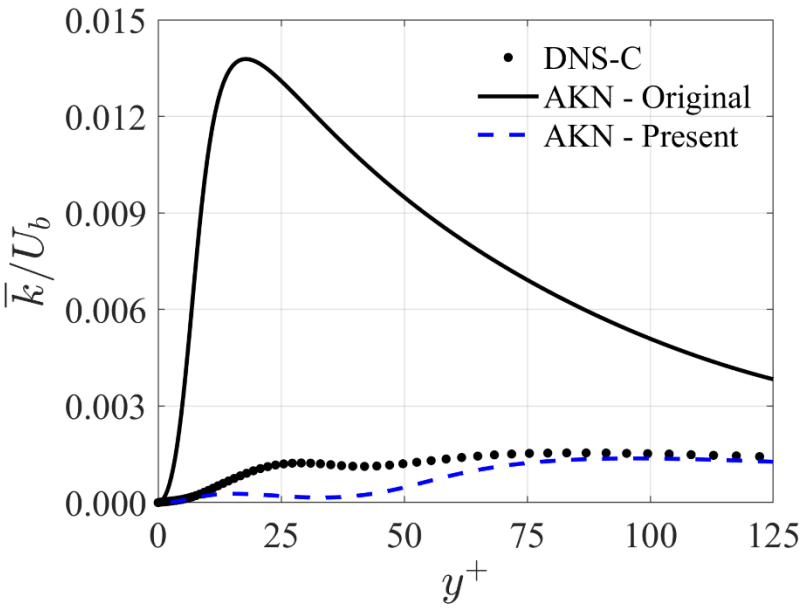

(b)

Figure 45: Comparison of line traces of velocity (a) and turbulent kinetic energy (b) for buoyancy aided flow for Case C within the heated vertical pipe configuration between DNS [9] (markers) and the original (solid lines) and modified (dashed lines) AKN models.

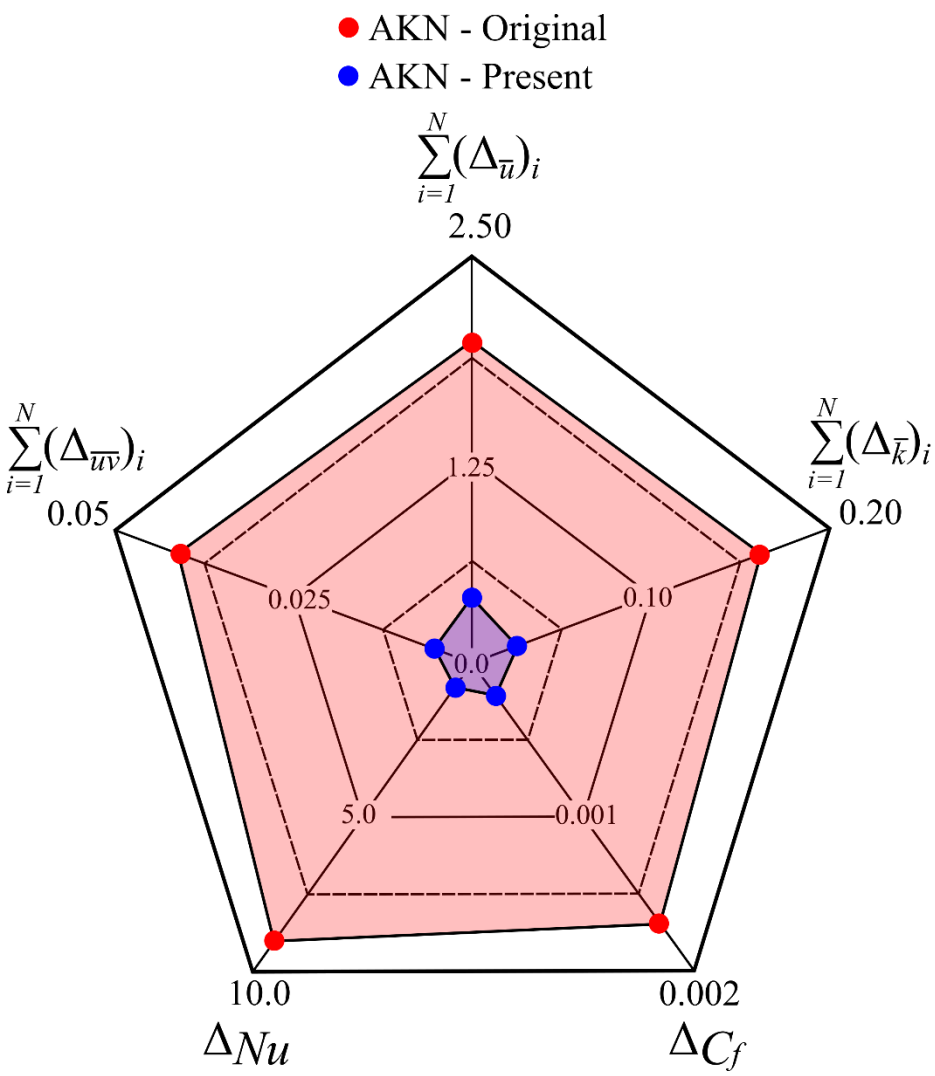

Figure 46: Results of the area validation metric for various system response quantities between the original and modified AKN model for Case C in the heated vertical pipe configuration

In Figure 47(a), the AKN model not only captures the laminarization effect on the near-wall Reynolds stress, but also predicts the inflection in the free stream ($y^+ > 75$), where the turbulent production is now dominant. The drastic improvements to the prediction of system response quantities is clearly observed both qualitatively and quantitatively

through line traces and the cumulative area validation metric, respectively. The congruence between the model and DNS results provides further justification for the inclusion of the new source term as a method to capture the complex effects of buoyancy in this coupled system.

Table 12: Comparative results for Nusselt number and skin-friction coefficient between the original and modified AKN model and DNS for a heated vertical pipe flow [9].

Buoyant Case	Model	Nu	$C_f \times 10^{-3}$
Case B (Ri = 0.063)	DNS	15.68	8.75
	AKN - Original	17.88 *(13.11%)*	9.70 *(10.30%)*
	AKN - Present	13.97 *(11.54%)*	8.15 *(7.10%)*
Case C (Ri = 0.087)	DNS	7.67	7.95
	AKN - Original	17.12 *(76.24%)*	9.64 *(19.22%)*
	AKN - Present	7.66 *(0.13%)*	8.23 *(3.46%)*
Case D (Ri = 0.241)	DNS	10.45	1.10
	AKN – Original	10.17 *(2.72%)*	1.15 *(4.44%)*
	AKN - Present	10.16 *(2.85%)*	1.15 *(4.44%)*

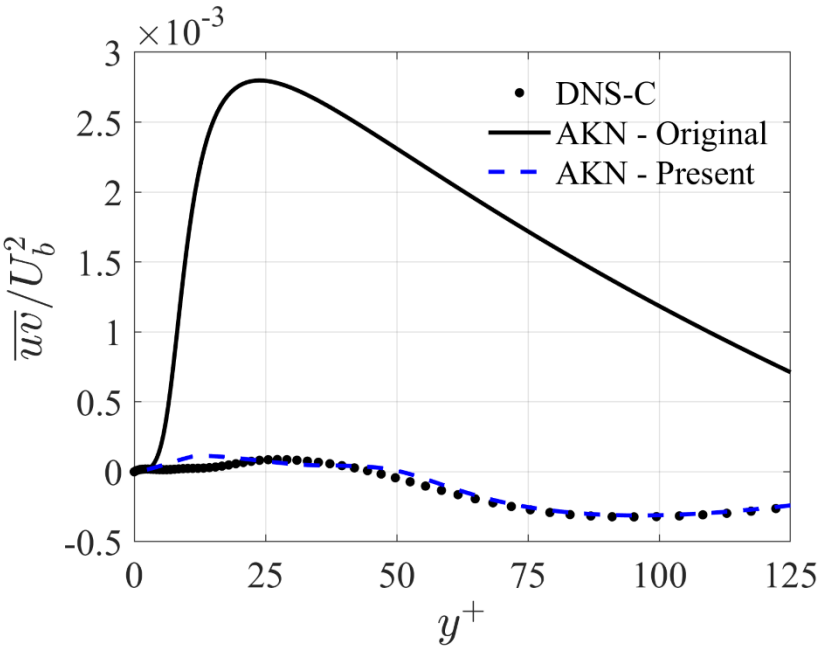

(a)

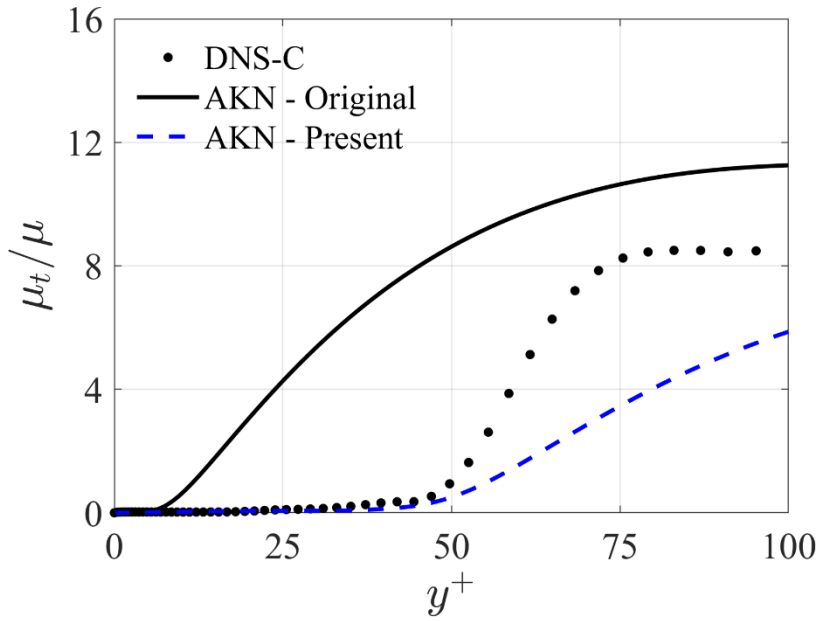

(b)

Figure 47: Comparison of line traces of Reynolds shear-stress (a) and turbulent viscosity ratio (b) for buoyancy aided flow for Case C within the heated vertical pipe configuration between DNS [9] (markers) and the original (solid lines) and modified (dashed lines) AKN models.

Case – D (Ri = 0.241)

The results presented in Table 12 highlight the improvements of the modified model in predicting the derived system response quantities of Nusselt number and skin friction coefficient. While Cases B and C showed a clear response to the inclusion of the new source term, the results of Case D show little to no change in comparison to the original model. As previously observed in the original model assessment presented in Chapter III, the predictions of all system response quantities are in excellent agreement with the DNS data. Therefore, special considerations are taken during the formulation of the new source term in Equation (61) to ensure the recovery of the original AKN model at higher levels of buoyancy. In this fashion, the benefits of the original model are preserved while improving the applicability for intermediate regimes such as Case B and C. Although redundant, the resulting profiles for system response quantities presented in Figure 48 and Figure 49 are almost precisely that of the original model. In accordance with many of the previous observations, the accurate representation of the turbulent viscosity (see Figure 49(b)) results in excellent predictions of system response quantities. The similarity in the results between the original and modified model is clearly represented by the validation metric in Figure 50. The marginal differences in the cumulative area metrics from the original and modified AKN models indicate that there is still some lingering effects of the new source term on the system response quantities. However, the relative differences between the original and modified model in Case D is insignificant in comparison to the improvements made by implementing the source term in Cases B and C.

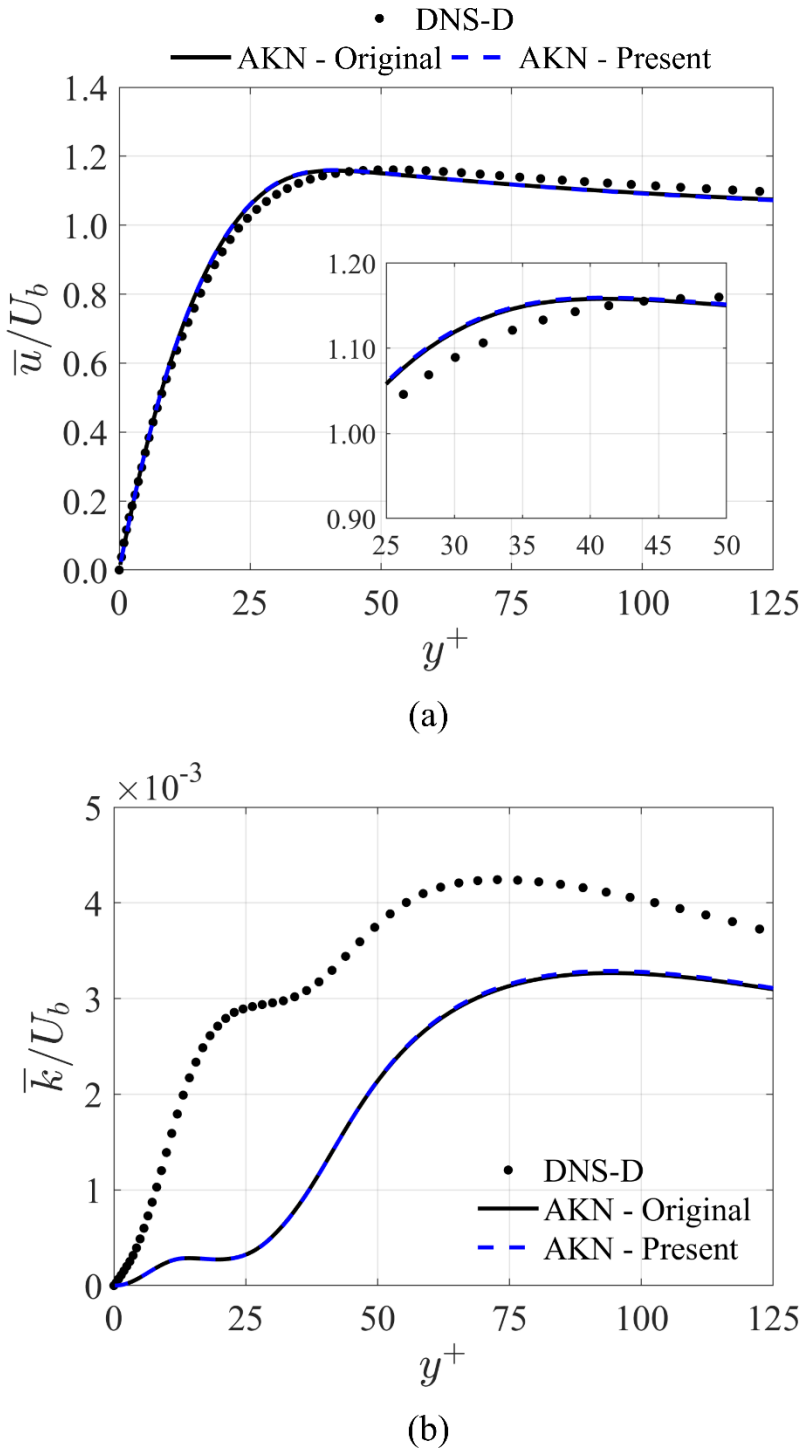

Figure 48: Comparison of line traces of velocity (a) and turbulent kinetic energy (b) for buoyancy aided flow for Case D within the heated vertical pipe configuration between DNS [9] (markers) and the original (solid lines) and modified (dashed lines) AKN models

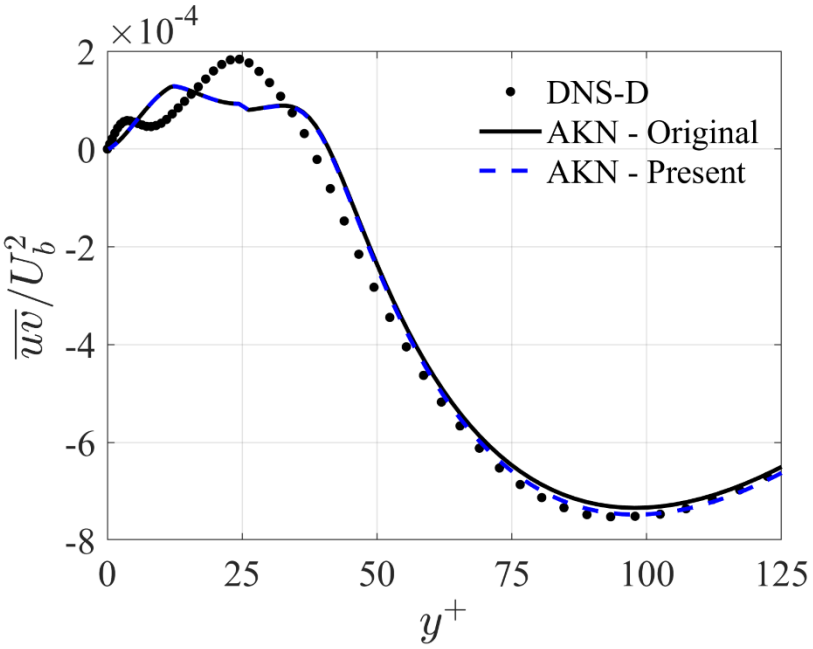

(a)

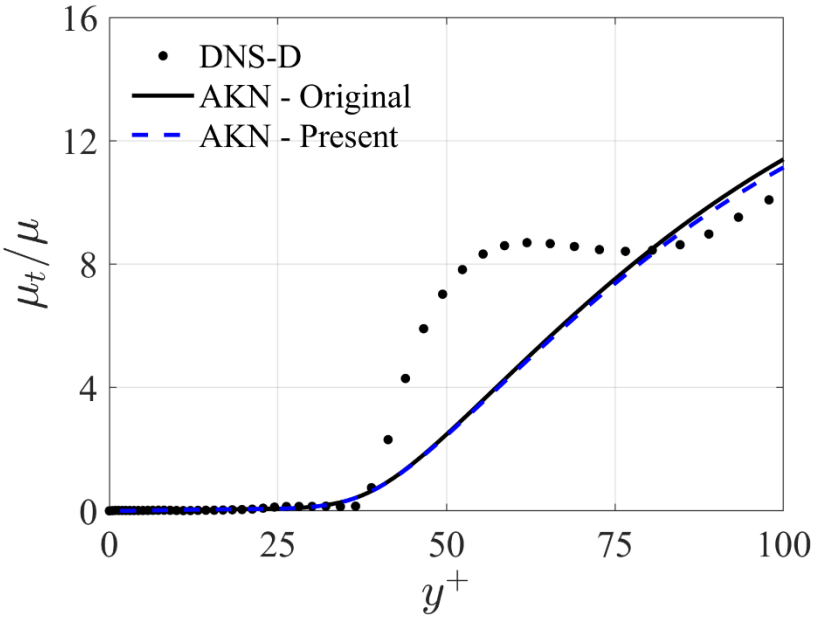

(b)

Figure 49: Comparison of line traces of Reynolds shear-stress (a) and turbulent viscosity ratio (b) for buoyancy aided flow for Case D within the heated vertical pipe configuration between DNS [9] (markers) and the original (solid lines) and modified (dashed lines) AKN models.

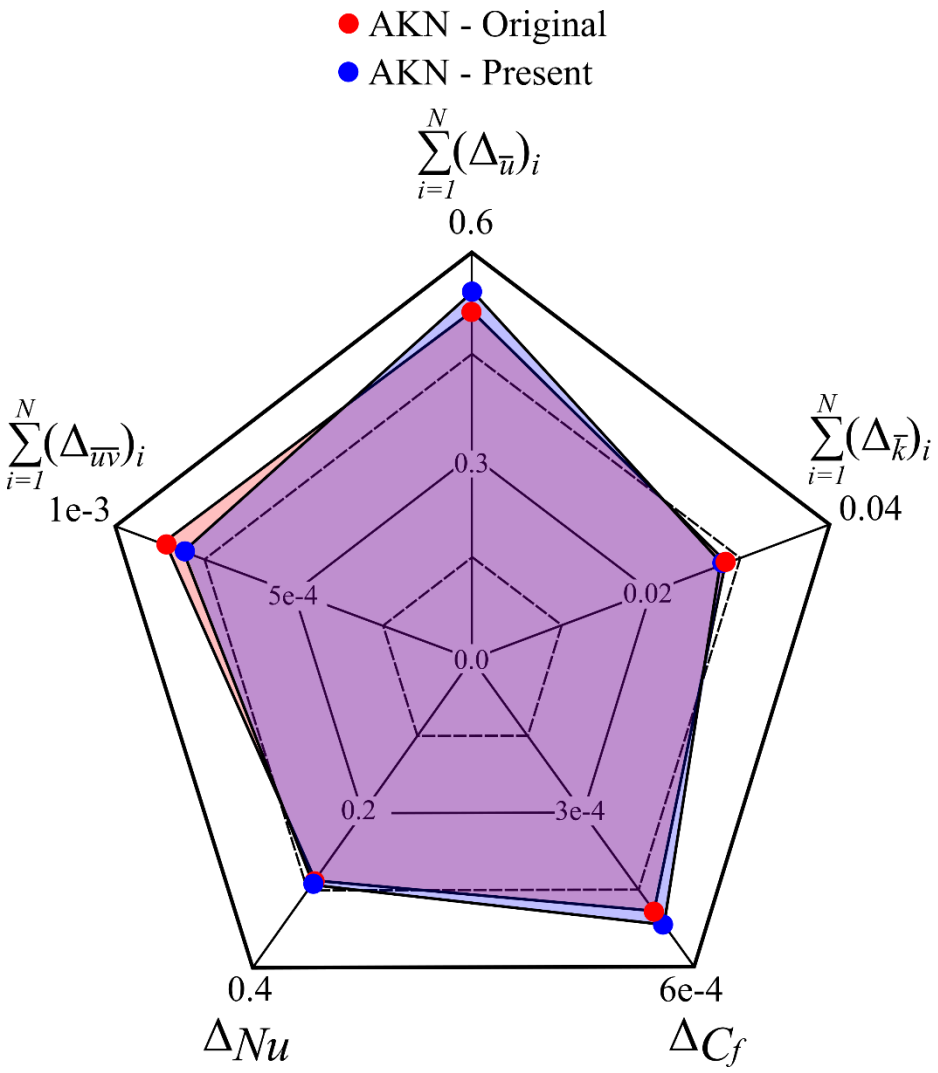

Figure 50: Results of the area validation metric for various system response quantities between the original and modified AKN model for Case D in the heated vertical pipe configuration.

In all cases within the heated vertical pipe configuration, the turbulent viscosity prediction is either maintained or improved with the inclusion of the newly proposed source term defined in Equation (61). This ad-hoc modification provides a simple, effective way of improving the applicability of the AKN model without a complete

overhaul of the underlying model assumptions. The formulation of the source term includes two localized buoyant flow variables, the turbulent Grashof (Gr_t) and turbulent Richardson (Ri_t) numbers, which allows the model to retain its original form in the absence of the buoyancy force. In addition, at very high levels of buoyancy, the source term is designed to collapse to the original model, as it is performs well in the prediction of highly buoyant flow regimes. A comparison of the range of applicability between the original and modified AKN model is presented in Figure 51 and Figure 52 through use of the area validation metric. The results of the original model in Figure 51 highlights the sizable discrepancy between Case C and all other cases. Ideally, the total area encompassed by each model result should be relatively similar, implying the model is equally applicable to each regime. This discrepancy raises concerns as to the general suitability of the original model for buoyancy-influenced flow regimes. On the other hand, the buoyancy-modified AKN model greatly reduces the spread of the validation metric observed in the original model. Although the original AKN models prediction of the velocity and turbulent kinetic energy for Case B is in better agreement with the DNS results, the near-wall turbulent viscosity is captured more accurately in the modified AKN model, resulting in better predictions of Nusselt number, skin friction, and Reynolds shear-stress. In contrast to the original model, the results presented in Figure 52 shows that the inclusion of the proposed source term provides a significant improvement to the model's applicability within the investigated mixed convection regimes.

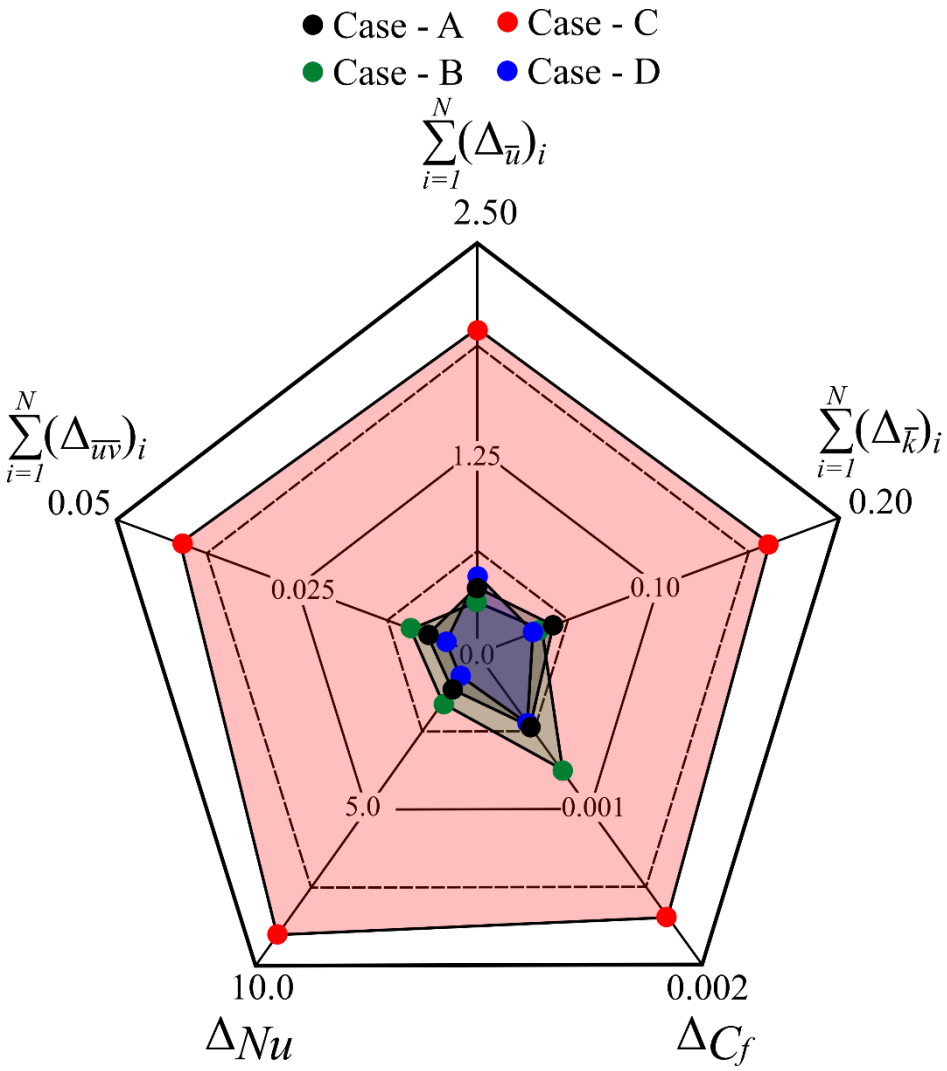

Figure 51: Results of the area validation metric the original AKN model in the heated vertical pipe configuration.

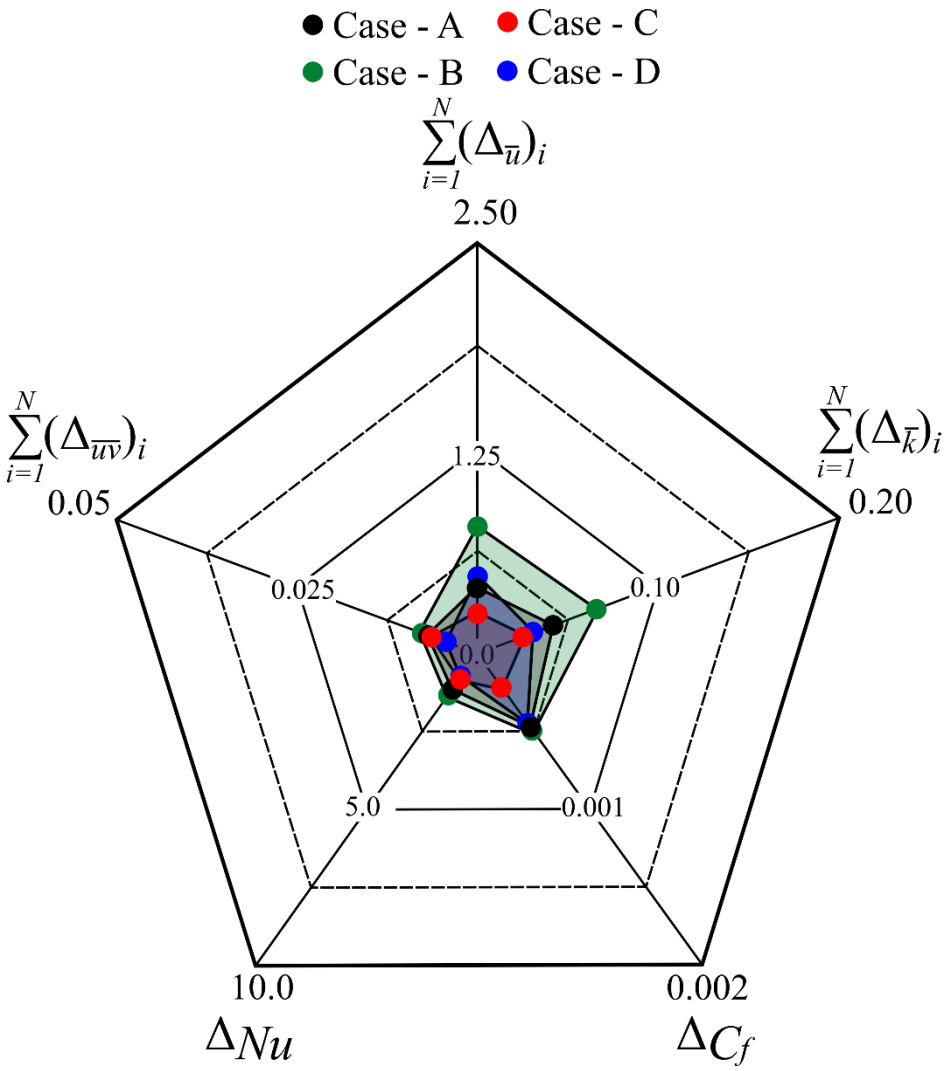

Figure 52: Results of the area validation metric for the buoyancy modified AKN model in the heated vertical pipe configuration.

CHAPTER V

CONCLUSIONS

As previously mentioned in Chapter I, the current research addresses the buoyancy related modeling issues inherent in RANS based turbulence models through three distinct contributions. The first of which is in Chapter II, where the applicability of RANS based turbulence models for the prediction of buoyant flows is assessed thorough a detailed model validation study against benchmark quality experimental data. This study showed that similar difficulties in the prediction of buoyant flows exists for all RANS based turbulence models, regardless of the level of complexity in the model. The use of a validation metric in the model assessment provides a way of ranking the most appropriate model for the given application. In this case, the low-Reynolds number AKN model is selected for further analysis based on the model validation results.

The analysis of the AKN model against the DNS database in Chapter III gives rise to the second contribution: provide insight into the deficiencies inherent in the RANS modeling paradigm for the prediction of buoyancy-influenced flow regimes using high-fidelity simulation results. In this chapter, the discrepancy in predictions of system response quantities is largely attributed to the representation of the turbulent viscosity, which acts as the interconnecting link between energy, momentum, turbulence and buoyancy. To correct for this disparity, Chapter IV describes a proposed a source term in the turbulent dissipation rate equation which is derived to effectively reduce the turbulent viscosity. This source term provides the third and final contribution from the

current research: enhance the predictive capability of RANS models for buoyancy-aided flows through a local buoyancy related source term targeted at the inherent deficiencies in the underlying modeling assumptions. Detailed discussions of these contributions are addressed in the conclusions below for each chapter.

Applicability of Common RANS Models for Transient Forced to Natural Convection

The applicability of several RANS turbulence models of varying complexity for the transient solution of forced to natural convection along a heated plate is investigated with the use of qualitative and quantitative comparisons to experimental data. The turbulence models are selected based on either their popularity within industry for routine calculations, competence in the prediction of complex, buoyant flows, or a combination of both. Boundary conditions and system response quantities are provided from the experiment along with their corresponding uncertainties for use in model validation efforts. This transient case proves to be extremely challenging for RANS models to be able to predict the complex flow regimes including turbulent, transitional, stagnant and developing flows. While the troubles for such simplified mathematical models to predict the complicated physics is not surprising, the predictability of the models may have been subject to some questionable assumptions about the symmetry of the flow at the inlet during flow reversal. Unforeseen problems in the acquisition of the dynamic behavior at the surface of the heated plate foregoes any useful comparison for thermal quantities, however reliable data for the shear stress on the heated plate provides

validation quality data for the models. Concerted efforts are taken to quantify the spatial discretization uncertainty and input uncertainty for each model using ASME best practices in order to conduct a thorough model validation assessment.

The results are split into three different cases based on the flow regimes that occur within the transient. Case 1 spans from $t = 0 - 6$ s and encompasses the deceleration of the flow prior to any flow reversal, Case 2 includes the flow reversal from $t = 6 - 12$ s as well as the start of the natural convection regime and finally turbulent natural convection within Case 3 for $t = 12 - 18$ s. In Case 1 the flow is primarily within the forced convection regime, resulting in very good predictions both qualitatively for the mean velocity and turbulent kinetic energy, as well quantitatively using the area metric for the EB-RSM, SST, AKN and V2F models. This implies that these models are able to adequately capture the near wall gradients during the deceleration of the flow. The RKE-Xu model however, struggles even within the forced regime, to accurately capture the mean flow quantities.

The complex flow physics involved during the flow reversal in Case 2 negatively impacts the predictability for the all models in terms of the mean flow variables. The velocity and turbulent kinetic energy predictions are fairly sporadic, which is possibly due to the equality assumption made for y and z-components of velocity at the inlet. This assumption imposes an unjustified constraint on the z-component of velocity which may explain the erroneous downstream velocity predictions as well as the increased values for the validation metric. Even during the flow reversal, the EB-RSM performs very well in characterizing the near wall velocity gradients in terms of skin friction comparison to

the experimental data. This model proves to be valuable in terms of applicability to regime changing flows due to its sophisticated closure modeling and unique near wall treatment.

The natural convection regime that dominates the final case poses another challenge for the SST, V2F and AKN models due to a transition from laminar to turbulent flow along the tall heated plate. This transitional period causes deteriorated predictions in terms of the velocity and turbulent kinetic energy at the second downstream location. Although the RKE-Xu model uses a near wall treatment for improved prediction of buoyant flows, it consistently displays exaggerated velocity profiles compared to the experimental results as well as large over predictions of turbulent kinetic energy in the near wall. The poor predictions of the RKE-Xu model throughout the transient is due to the empirical formulation lacking generality in terms of applicability to other scenarios. The EB-RSM predicts the mean velocity and the turbulent kinetic energy very well in the final case, as well as possessing the lowest amount of dissimilarity to the experimental results in the validation metric.

Qualitative and quantitative comparison between several turbulence models and experimental data suggests that the EB-RSM is the most acceptable model to calculate the complex flow physics during a flow reversal from forced to natural convection. The SST, V2F and AKN models perform very well within the forced convection regime, however the predictions of mean flow variables and near wall velocity gradients degrades significantly during the flow reversal and transitional periods in Cases 2 and 3. The two-layer RKE-Xu model provides the worst representation of the experimental

results, highlighting the limited applicability of this empirically derived one equation model for buoyant flows. The qualitative results for velocity and turbulent kinetic energy exhibit solutions more likely to be categorized as outliers in comparison to the other models, which is confirmed with the results for the validation metric. Although the EB-RSM outperforms the less intricate models, the computational cost is significantly higher than the standard two-equation models. The high computational cost coupled with the inherent stability problems due to numerical stiffness leaves room for improvement in modeling of these complex flows. In the development of such a model, the use of high-fidelity simulations such as a Reynolds Stress Transport models, LES and DNS provide the mathematical justification for formulation of modeled terms while validation experiments provide a way of quantifying the models predictability to real world scenarios.

The difficulties experienced in this experimental data set are unique due to the complex physics attempting to be captured. While the experimental design falls short in accurately defining the three-dimensional flow at the inlet of the test section during the flow reversal, the mean flow profiles prior to this time seem to match up well with previous steady-state cases at similar flow conditions[23]. The quality of the data acquired from this experimental setup during these tests, as well as the detail in which the uncertainty is quantified is unmatched within the verification and validation community. However, this study shows that acquiring benchmark quality data for such a complicated phenomenon is not a trivial task, and even some of the most successful facilities may not be able to produce adequate data for model validation. Future studies

could benefit from advanced non-intrusive techniques to capture three-dimensional flow behavior such as tomographic PIV [69]. While this technique has potential to be successful in areas where less sophisticated methods have struggled, the underlying uncertainties associated with this technique have yet to be fully quantified. In terms of capturing transient thermal behavior, special care needs to be taken in order to ensure that the response time of the instrumentation is short enough to capture evolution of the phenomena over time.

Model Assessment Against DNS Database

Building off the results from the turbulence model assessment provided in Chapter II, the low-Reynolds number AKN model is selected as a viable option for further assessment and model development. Prior to model development, the applicability of the AKN model for buoyant flows is investigated through direct comparison with trusted DNS databases of two mixed convection flow configurations. The two configurations consist of a differentially heated parallel plate channel [10, 11] and a vertical pipe with a constant flux heating condition [9]. The combination of these two canonical flow databases provide two forced convection cases, as well as five separate buoyant flow cases which are characterized by the ratio of buoyant to inertial forces through their respective Richardson number ($Ri = Gr/Re^2$). Each flow configuration is fully developed in the streamwise direction and makes use of constant material properties to isolate the effect of buoyancy on the subsequent system response quantities. Each RANS case is computed on three separate systematically refined grids to ensure that the discretization uncertainty is minimized in accordance to the GCI

method. System response quantities at the centerline of the domain are compared between the DNS databases and AKN model, with particular focus on the impact that these predictions have on the resulting derived quantities like the Nusselt number and skin-friction coefficient. The AKN model can adequately reproduce the velocity and turbulent kinetic energy for forced convection, as well as for low values of Richardson number (Ri = 0.0, 0.047, 0.063), in both the channel and pipe configurations. In general, the velocity prediction in these cases is excellent, while the turbulent kinetic energy predictions are slightly underpredicted. Regardless of this underprediction, the AKN model provides a very good representation of the turbulent viscosity relative to the DNS, resulting in accurate predictions for the derived system response quantities of Nusselt number and skin-friction coefficient. Further increase in the Richardson number raises concerns about the sensitivity of the AKN model to capture the effect of buoyancy. This is highlighted by the inability of the AKN model to capture the effect of laminarization, characterized by the complete misrepresentation of the turbulent viscosity and a resulting overprediction of Nusselt number and skin-friction coefficient by 76.24% and 19.22%, respectively. At even higher levels of buoyancy (Ri = 0.241) the prediction of the AKN model recovers and provides a very good representation of the mean fields as well as derived quantities. The inability for the AKN model to predict these intermediate buoyancy regimes proves that there is room to improve the model's performance. In particular, the model must exhibit a heightened sensitivity to the effects of buoyancy, which is current deficient. Using well trusted databases such as the ones employed in the current study, it is possible to develop empirically derived modifications to the current

RANS model to more accurately predict the impact of buoyancy on mean flow quantities. These types of modifications provide an avenue for model development with a focus on improving the applicability to the highly non-linear interactions between buoyancy and turbulence. By concentrating the AKN model in this fashion, it is theorized that these augmentations could enhance the predictive capability of the original formulation without an overhaul of the existing framework. Ad-hoc modifications such as these are extremely common, particularly in commercial codes which contain numerous modifications to the standard models in the form of source terms, limiters and corrections. Nevertheless, all changes to original model formulations are derived with the same goal in mind – to provide a more accurate representation of the flow topology through modification of the turbulent viscosity.

Model Modification and Validation

The current analysis builds upon the previous assessment of the AKN model and its predictive capacity in buoyancy-influenced flow regimes as presented in Chapter III. The model predictions are compared against highly trusted DNS databases for mixed convection flows over a range of Richardson numbers. The assessment showed that the AKN model is in good agreement with the DNS data in forced convection regimes (Ri = 0.0), as well as flows characterized by very low Richardson numbers (Ri = 0.043). However, at intermediate Richardson numbers, it is determined that the AKN model lacks the sensitivity to capture the intricate effects of buoyancy. Even with slight increases in Richardson number (Ri = 0.063 – 0.087), the applicability of the model

progressively declines until much higher levels of buoyancy influence (Ri = 0.241), in which the model predictions recover. In one particular case, the insensitivity of the original AKN model to buoyancy results in the overprediction of Nusselt number and skin friction coefficient by 76.24% and 19.22%, respectively. The poor predictions in system response quantities is a direct result of the model's representation of the turbulent viscosity, which serves as the interconnecting link between turbulence, momentum, energy and buoyancy. To rectify the insensitivity of the AKN model to buoyancy, an explicit source term is added to the governing equation for the turbulent dissipation rate as a function of newly defined local flow variables. The addition of the new source term succeeds in sensitizing the original AKN model to buoyancy, greatly improving the predictions of system response quantities in the laminarization regime. This improvement is most notable in the prediction of Nusselt number and skin friction coefficient, where the relative difference between the AKN model and DNS is reduced from 76.24% to 0.13% for Nusselt number and 19.22% to 3.46% for the skin friction coefficient. Another important feature of the modified models is that it maintains the success of the original formulation in the forced convection and highly buoyant regimes. Overall, the buoyancy modified AKN model improves the applicability of the original model to wider range of buoyancy-influenced flow regimes.

Future Work

The present study provides a very promising contribution in the pursuit of improving model predictions for buoyancy-influenced flow regimes. Nevertheless, the current model must undergo even further analysis and scrutiny before being claimed as superior to the original formulation. This modified variant of the AKN model provides excellent predictions under the limited, idealized conditions in the current study. In order to ensure the generality of the current model, it must be tested against additional buoyant flow regimes. The DNS database in the current analysis must be expanded to include Richardson numbers in between and beyond those included in the current study. In addition, the model validation must be expanded to include both buoyancy-aided and buoyancy-opposed regimes. The current model shows promising results for the historically troublesome buoyancy-aided regime; however, a similar detailed assessment must be performed for the opposed regime to ensure that the modifications do not compromise the original model predictions. Following these additional assessments, further insight into the effects of buoyancy on turbulent quantities could aid in developing a general source term applicable to a wider range of RANS models. Finally, to confirm the utility of the present model, an additional validation study must be performed against benchmark quality experimental datasets. To this end, supplementary benchmark quality experiments must be conducted over a wide range of buoyant regimes to aid in model validation efforts. In addition, experimental data sets like those in Chapter II must be revisited in order to supply accurate heat transfer estimates and boundary condtions during accident-type conditions. Not only are these experiments

pivotal in accelerating the design of next generation of power reactors, they provide invaluable benchmarks in complex conditions which push past the expected limitations of the current stable of RANS based turbulence models. In this way, any model can fully be tested, leaving considerably less uncertainty as to its applicability within buoyancy-influenced flow regimes.

REFERENCES

[1] R. A. Berry, J. W. Peterson, H. Zhang, R. C. Martineau, H. Zhao, L. Zou, *et al.*, "Relap-7 Theory Manual," Idaho National Lab, Idaho Falls, ID, 2018.

[2] "TRACE V5. 0 Theory Manual, Field Equations, Solution Methods, and Physical Models," 2010.

[3] US DOE Nuclear Energy Research Advisory Committee, "A Technology Roadmap for Generation IV Nuclear Energy Systems," *GIF-002-00,* 2002.

[4] Y.H. Tung, Y.M. Ferng, R. W. Johnson, and C.C. Chieng, "Study of Natural Circulation in a VHTR After a LOFA Using Different Turbulence Models," *Nuclear Engineering and Design,* vol. 263, pp. 206-217, 2013.

[5] Y.H. Tung, Y.M. Ferng, R. W. Johnson, and C.C. Chieng, "Transient LOFA Computations for a VHTR Using One-Twelfth Core Flow Models," *Nuclear Engineering and Design,* vol. 301, pp. 89-100, 2016.

[6] Y.H. Tung, R. W. Johnson, Y.M. Ferng, and C.C. Chieng, "Modeling Strategies to Compute Natural Circulation Using CFD in a VHTR After a LOFA," *Nuclear Engineering and Design*, vol. 275, pp. 80-90, 2014.

[7] Y.H. Tung, R. W. Johnson, Y.M. Ferng, and C.C. Chieng, "Bypass Flow Computations on the LOFA Transient in a VHTR," *Applied Thermal Engineering*, vol. 62, pp. 415-423, 2014.

[8] B. W. Lance and B. L. Smith, "Experimental Validation Benchmark Data for Computational Fluid Dynamics of Transient Convection from Forced to Natural

with Flow Reversal on a Vertical Flat Plate," *Journal of Verification, Validation and Uncertainty Quantification,* vol. 1, p. 031005, 2016.

[9] J. You, J. Y. Yoo, and H. Choi, "Direct Numerical Simulation of Heated Vertical Air Flows in Fully Developed Turbulent Mixed Convection," *International Journal of Heat and Mass Transfer,* vol. 46, pp. 1613-1627, Apr 2003.

[10] N. Kasagi and O. Iida, "Progress in Direct Numerical Simulation of Turbulent Heat Transfer," in *Proceedings of the 5th ASME/JSME Joint Thermal Engineering Conference,* San Deigo, CA, March 15-19, 1999.

[11] N. Kasagi and M. Nishimura, "Direct Numerical Simulation of Combined Forced and Natural Turbulent Convection in a Vertical Plane Channel," *International Journal of Heat and Fluid Flow,* vol. 18, pp. 88-99, 1997.

[12] K. Hanjalić, "One-Point Closure Models for Buoyancy-Driven Turbulent Flows," *Annual Review of Fluid Mechanics,* vol. 34, pp. 321-347, 2002.

[13] K. Hanjalić and B. Launder, *Modelling Turbulence in Engineering and the Environment: Second-Moment Routes to Closure*: Cambridge university press, New York, NY, 2011.

[14] S. Kenjereš, S. Gunarjo, and K. Hanjalić, "Contribution to Elliptic Relaxation Modelling of Turbulent Natural and Mixed Convection," *International Journal of Heat and Fluid Flow,* vol. 26, pp. 569-586, 2005.

[15] T. Craft, B. Launder, and K. Suga, "Development and Application of a Cubic Eddy-Viscosity Model of Turbulence," *International Journal of Heat and Fluid Flow,* vol. 17, pp. 108-115, 1996.

[16] W. Xu, Q. Chen, and F. Nieuwstadt, "A New Turbulence Model for Near-Wall Natural Convection," *International Journal of Heat and Mass Transfer,* vol. 41, pp. 3161-3176, 1998.

[17] W.S. Kim, S. He, and J.D. Jackson, "Assessment by Comparison with DNS Data of Turbulence Models Used in Simulations of Mixed Convection," *International Journal of Heat and Mass Transfer,* vol. 51, pp. 1293-1312, 2008.

[18] A. Keshmiri, A. Revell, and H. G. Darabkhani, "Assessment of a Common Nonlinear Eddy-Viscosity Turbulence Model in Capturing Laminarization in Mixed Convection Flows," *Numerical Heat Transfer, Part A: Applications,* vol. 69, pp. 146-165, 2016.

[19] A. Keshmiri, J. Uribe, and N. Shokri, "Benchmarking of Three Different CFD Codes in Simulating Natural, Forced, and Mixed Convection Flows," *Numerical Heat Transfer, Part A: Applications,* vol. 67, pp. 1324-1351, 2015.

[20] B. Smith, M. Andreani, U. Bieder, D. Bestion, F. Ducros, E. Graffard, *et al.*, "Assessment of Computational Fluid Dynamics (CFD) for Nuclear Reactor Safety Problems," *No. NEA-CSNI-R-2007-13,* Organisation for Economic Co-Operation and Development, 2008.

[21] K. L. Jones and B. L. Smith, "Benchmark Experiments for Steady-State Natural Convection in Fuel Rod Bundles," *Journal of Verification, Validation and Uncertainty Quantification,* vol. 2, p. 021001, 2017.

[22] J. R. Harris, B. W. Lance, and B. L. Smith, "Experimental Validation Data for Computational Fluid Dynamics of Forced Convection on a Vertical Flat Plate," *Journal of Fluids Engineering*, vol. 138, p. 011401, 2016.

[23] B. W. Lance, J. R. Harris, and B. L. Smith, "Experimental Validation Benchmark Data for Computational Fluid Dynamics of Mixed Convection on a Vertical Flat Plate," *Journal of Verification, Validation and Uncertainty Quantification*, vol. 1, p. 021005, 2016.

[24] American Society of Mechanical Engineers, *Standard for Verification and Validation in Computational Fluid Dynamics and Heat Transfer: An American National Standard*: American Society of Mechanical Engineers, New York, NY, 2009.

[25] W. L. Oberkampf and C. J. Roy, *Verification and Validation in Scientific Computing*: Cambridge University Press, New York, NY, 2010.

[26] H. W. Coleman and W. G. Steele, *Experimentation, Validation, and Uncertainty Analysis for Engineers*: John Wiley & Sons, Hoboken, NJ, 2018.

[27] B. H. Timmins, B. W. Wilson, B. L. Smith, and P. P. Vlachos, "A Method for Automatic Estimation of Instantaneous Local Uncertainty in Particle Image Velocimetry Measurements," *Experiments in Fluids,* vol. 53, pp. 1133-1147, 2012.

[28] B. M. Wilson and B. L. Smith, "Taylor-Series and Monte-Carlo-Method Uncertainty Estimation of the Width of a Probability Distribution Based on

Varying Bias and Random Error," *Measurement Science and Technology,* vol. 24, p. 035301, 2013.

[29] C. E. Clifford and M. L. Kimber, "Assessment of RANS-Based Turbulence Models for Buoyancy-Influenced Forced Convection on a Heated Vertical Surface," *Journal of Verification, Validation and Uncertainty Quantification,* 2019.

[30] B. W. Lance and B. L. Smith, "Transient Convection from Forced to Natural with Flow Reversal on a Vertical Flat Plate," in *NURETH-16*, Chicago, IL, 2015.

[31] *ANSYS ICEM CFD*, Release 19.0, ANSYS Inc., Cannonsburg, PA, 2019.

[32] Siemens, "Simcenter STAR-CCM+ User Guide V13. 04," *Siemens PLM,* Plano, TX, 2018.

[33] T.H. Shih, W.L. William, A. Shabbir, Z. Yang, J. Zhu, "A New K-Epsilon Eddy Viscosity Model for High Reynolds Number Turbulent Flows," *Computers and Fluids*, vol. 24, pp. 227-238, 1995.

[34] F. R. Menter, "Two-Equation Eddy-Viscosity Turbulence Models for Engineering Applications," *AIAA,* vol. 32, pp. 1598-1605, 1994.

[35] D. A. Johnson and L.S King, "A Mathematically Simple Turbulence Closure Model for Attached and Separated Turbulent Boundary Layers," vol. 23, pp. 1684-1692, 1985.

[36] K. Abe, T. Kondoh, and Y. Nagano, "A New Turbulence Model for Predicting Fluid Flow and Heat Transfer in Separating and Reattaching Flows—I. Flow

Field Calculations," *International Journal of Heat and Mass Transfer,* vol. 37, pp. 139-151, 1994.

[37] K. Abe, T. Kondoh, and Y. Nagano, "A New Turbulence Model for Predicting Fluid Flow and Heat Transfer in Separating and Reattaching Flows—II. Thermal Field Calculations," *International Journal of Heat and Mass Transfer,* vol. 38, pp. 1467-1481, 1995.

[38] L. Davidson, "Modification of the V2F Model for Computing the Flow in a 3D Wall Jet," *Turbulence Heat Mass Trans.,* vol. 4, pp. 577-584, 2003.

[39] P. A. Durbin, "Near-Wall Turbulence Closure Modeling Without “Damping Functions”," *Theoretical and Computational Fluid Dynamics,* vol. 3, pp. 1-13, 1991.

[40] F. Lien, G. Kalitzin, and P. Durbin, "RANS Modeling for Compressible and Transitional Flows," *Proceedings of the Stanford University Center for Turbulence Research Summer Program,* pp. 267-286, 1998.

[41] R. Manceau and K. Hanjalić, "Elliptic Blending Model: A New Near-Wall Reynolds-Stress Turbulence Closure," *Physics of Fluids,* vol. 14, pp. 744-754, 2002.

[42] E. Lemmon, M. McLinden, and D. Friend, *Thermophysical Properties of Fluid Systems*. Gaithersburg MD, 20899: National Institute of Standards and Technology, 2019.

[43] R. W. Johnson, "Modeling Strategies for Unsteady Turbulent Flows in the Lower Plenum of the VHTR," *Nuclear Engineering and Design*, vol. 238, pp. 482-491, 2008.

[44] P. J. Roache, "Perspective: A Method for Uniform Reporting of Grid Refinement Studies," *Journal of Fluids Engineering*, vol. 116, no. 3, pp. 405-413, 1994.

[45] L. Eça, "An Evaluation of Verification Procedures for CFD Applications," in *24th Symposium on Naval Hydrodynamics, Fukuoka, Japan, 2002*, pp. 568-587.

[46] L. Eça, M. Hoekstra, and P. Roache, "Verification of Calculations: An Overview of the Lisbon Workshop," in *23rd AIAA Applied Aerodynamics Conference*, Toronto, ON, 2005, p. 4728.

[47] J. Cadafalch, R. Consul, and A. Oliva, "Verification of Finite Volume Computations on Steady-State Fluid Flow and Heat Transfer," *Journal of Fluids Engineering*, vol. 124, pp. 11-21, 2002.

[48] T. Xing and F. Stern, "Factors of Safety for Richardson Extrapolation," *Journal of Fluids Engineering*, vol. 132, p. 061403, 2010.

[49] I. B. Celik, U. Ghia, P. J. Roache, and C. J. Freitas, "Procedure for Estimation and Reporting of Uncertainty Due to Discretization in CFD Applications," *Journal of Fluids Engineering*, vol. 130, no. 7, p.4, 2008, Art no. 078001.

[50] L. Eça, G. Vaz, S. Toxopeus, and M. Hoekstra, "Numerical Errors in Unsteady Flow Simulations," *Journal of Verification, Validation and Uncertainty Quantification*, vol. 4, 2019.

[51] P. Knupp and K. Salari, *Verification of Computer Codes in Computational Science and Engineering*: CRC Press, Boca Raton, FL, 2002.

[52] J. Kamm, W. Rider, and J. Brock, "Combined Space and Time Convergence Analysis of a Compressible Flow Algorithm," in *16th AIAA Computational Fluid Dynamics Conference*, June 23-26, Orlando, FL, 2003, p. 4241.

[53] S. Ferson, W. L. Oberkampf, and L. Ginzburg, "Model Validation and Predictive Capability for the Thermal Challenge Problem," *Computer Methods in Applied Mechanics and Engineering*, vol. 197, pp. 2408-2430, 2008.

[54] N. Kumar Singh and B. Premachandran, "Analysis of Turbulent Natural and Mixed Convection Flows Using the v2–f Model," *Journal of Heat Transfer,* vol. 138, 2016.

[55] S. V. Patankar, C. H. Liu, and E. M. Sparrow, "Fully Developed Flow and Heat Transfer in Ducts Having Streamwise-Periodic Variations of Cross-Sectional Area," *Journal of Heat Transfer,* vol. 99, pp. 180-186, 1977.

[56] B. J. Daly and F. H. Harlow, "Transport Equations in Turbulence," *The Physics of Fluids,* vol. 13, pp. 2634-2649, 1970.

[57] N. Ince and B. Launder, "On the Computation of Buoyancy-Driven Turbulent Flows in Rectangular Enclosures," *International Journal of Heat and Fluid Flow,* vol. 10, pp. 110-117, 1989.

[58] C.M. Rhie and W. L. Chow, "Numerical Study of the Turbulent Flow Past an Airfoil with Trailing Edge Separation," *AIAA* Journal, vol. 21, no. 11, pp. 1525-1532, 1983.

[59] S. B. Pope, *Turbulent Flows:* Cambridge University Press, New York, NY, 2000.

[60] C. R. Yap, "Turbulent Heat and Momentum Transfer In Recirculating and Impinging Flows," PhD, Mechanical Engineering, The University of Manchester, 1990.

[61] S.B. Pope, "An Explanation of the Turbulent Round-Jet/Plane-Jet Anomaly," *AIAA Journal,* vol. 16, pp. 279-281, 1978.

[62] M. Kato and B. Launder, "The Modelling of Turbulent Flow Around Stationary and Vibrating Square Cylinders," in *Turbulent Shear Flow,* Kyoto, 1993, pp. 10.4. 1-10.4. 6.

[63] B. E. Launder and B. Sharma, "Application of the Energy-Dissipation Model of Turbulence to the Calculation of Flow Near a Spinning Disc," *Letters in Heat and Mass Transfer,* vol. 1, pp. 131-137, 1974.

[64] Z. Yang and T.H. Shih, "New Time Scale Based K-Epsilon Model for Near-Wall Turbulence," *AIAA Journal,* vol. 31, pp. 1191-1198, 1993.

[65] C. Lam and K. Bremhorst, "A Modified Form of the k-ε Model for Predicting Wall Turbulence," *Journal of Fluids Engineering,* vol. 103, no. 3, pp. 456-460, 1981.

[66] A. M. Oler, C. E. Clifford, and M. L. Kimber, "Quantitative Assessment of Eddy-Viscosity RANS Models for Turbulent Mixed Convection in a Differentially Heated Plane Channel " *International Journal of Heat Transfer* 2020.

[67] M.A. Cotton and P.J. Kirwin, "A Variant of the Low-Reynolds-Number Two-Equation Turbulence Model Applied to Variable Property Mixed Convection Flows," *International Journal of Heat and Fluid Flow*, vol. 16, no. 6, pp. 486-492, 1995.

[68] W. Rodi, *Turbulence Models and Their Application in Hydraulics*: CRC Press, Boca Raton, FL, 1993.

[69] G. E. Elsinga, F. Scarano, B. Wieneke, and B. W. van Oudheusden, "Tomographic Particle Image Velocimetry," *Experiments in Fluids*, vol. 41, pp. 933-947, 2006.